Computational Study on Thermal Responses of Laser Irradiated Blood Perfused and Vascularized Tissues

A Thesis Submitted

for the Award of the Degree of

Doctor of Philosophy

by

Rupesh Singh

DEPARTMENT OF MECHANICAL ENGINEERING
INDIAN INSTITUTE OF TECHNOLOGY GUWAHATI

October 2014

भारतीय प्रौद्योगिकी संस्थान गुवाहाटी
Indian Institute of Technology Guwahati

ACKNOWLEDGMENTS

First of all, I would like to express my deepest gratitude to my supervisor, Prof. Subhash C. Mishra, for his invaluable inspiration, encouragement and support throughout my PhD. I am very thankful to GCOE at Institute of Fluid science, Tohoku University and Prof. S. Maruyama for providing me valuable guidance and support during my internship period. I am also thankful to Dr. J. Okajima and student members of Maruyama's laboratory for their support.

I would like to thank all my doctoral committee members, namely, Dr. Niranjan Sahoo, Dr. Vinayak Kulkarni, and Dr. Dipankar Bandyopadhyay, for their valuable advice and encouragement. I am very grateful to faculty members and staff members of the Department of Mechanical Engineering, Indian Institute of Technology Guwahati, for their support and guidance during my PhD program.

And last, but not the least, I am thankful to all my friends at IIT Guwahati for their love and support. Special thanks to Koushik, Aritra and Niraj for their invaluable cooperation.

Journal Publications

1 **R. Singh**, K. Das and S. C. Mishra, Laser-induced hyperthermia of nanoshell mediated vascularized tissue – A numerical study, ***Journal of Thermal Biology*** vol. 44, pp. 55-62, 2014.

2 S.C. Mishra, **R. Singh**, P. Agarwal and C. H. Krishna, Analysis of radiative transport in a 2-D cylindrical participating medium subjected to collimated radiation, ***Numerical Heat Transfer***, *Part A*, Vol. 66 (8), pp. 884-903, 2013.

3 **R. Singh**, K. Das, S. C. Mishra, J. Okajima, and S. Maruyama, Minimizing Tissue Surface Damage Using Convective Cooling During Laser Induced Thermal Therapy – A Numerical Study, ***Journal of Thermal Science and Engineering Applications, ASME journal*** (Accepted).

4 **R. Singh,** A. Sasmal, S. C. Mishra, Transmittance signal analysis of a short pulse laser irradiated cancerous lung tissue as a function of respiration, ***Optik*** (Under review).

5 **R. Singh**, K. Das, J. Okajima, S. Maruyama and S. C. Mishra, Skin cooling using optical windows and cryogens during laser induced hyperthermia, ***Applied Thermal Engineering*** (Under review).

Conference Publications

1 **R. Singh**, S. C. Mishra, Nanoparticle Mediated Laser Irradiation of Pig Lung as a Function of Respiration, *Eleventh International Conference on Flow Dynamics (ICFD2014)*, Tohoku University, Japan, 2014.

2 **R. Singh**, K. Das, S. C. Mishra, J. Okajima and S. Maruyama, Minimizing skin thermal damage using surface cooling during laser induced thermal therapy - a numerical study, 22nd National and 11th *ISHMT - ASME Heat and Mass Transfer Conference*, IIT Kharagpur, India, 2013.

3 **R. Singh**, J. Okajima, S. C. Mishra, S. Maruyama, U. Barman, Hyperthermia Treatment of Lung Cancer using Laser and Inhalable Nanoparticles, *Tenth International Conference on Flow Dynamics* (ICFD2013), Tohoku University, Japan, 2013.

ABSTRACT

Lasers find extensive applications in medicine and biology. The laser-tissue interaction has remained an active area of research. Its usage has been explored in the treatment of anomalies such as port-wine stain and diseases like cancers. Treatment is performed by the thermal effects of laser irradiation, and the process is known as laser induced hyperthermia or laser induced thermal therapy. It is important therefore to understand heat transfer and radiative transfer inside biological tissue. During any laser induced heating of biological tissues, two of the major concerns are (i) skin surface overheating and (ii) undesired thermal damage of healthy tissue. In present study, a quantitative evaluation of the effect of heating by laser irradiation in biological tissue is performed.

The objective of laser induced hyperthermia and thermal therapy procedures is to treat the affected tissue while minimizing the thermal damage to the surface of the skin and the surrounding healthy tissues. Using the contact surface cooling method, skin surface temperature rise can be prevented during laser irradiation of tissue. During any such procedures, skin surface cooling is desirable to prevent its damage. Optical window surface contact cooling and cryogenic spray cooling are widely used methods for the skin surface cooling.

Optical windows are materials which are transparent for the wavelength ranging from ultra violet to near infra-red, and they are used for providing a transparent and highly conducting contact cooling material. In the present study, four optical windows are examined for their suitability during contact cooling applications. The four optical window used are sapphire, yttrium aluminium garnet, lithium tantalate, and magnesium oxide doped lithium niobate. In addition to the optical windows, two cryogens (R1234yf and liquid CO_2) are also studied for spray type cooling and in combination with optical window cooling.

The modelling of laser propagation and absorption in biological tissue is done by solving the bioheat and radiative transfer equation. In order to study heat transfer phenomena inside biological tissue when the tissue surface is irradiated by the laser, numerical simulations are conducted. The radiative transfer equation was solved by the discrete ordinate method, and for

the simple cases, by radiation element method by ray emission model. The temperature distribution in the biological tissue on laser irradiation was numerically estimated by the radiation-bioheat conduction combined heat transfer. In addition, for heat conductive simulation, Pennes bio-heat transfer equation for blood perfused tissues, and Weinbaum-Jiji model for vascularized tissues, were used and solved using finite volume method. Two laser wavelengths of 632.8 nm and 1064 nm are considered.

Laser induced thermo-optical signal analysis of biological tissues is an emerging area of tumor detection and characterization. Thermophysical and optical properties of an abnormal tissue are different than that of a healthy one. Transmittance and reflectance signals from the laser irradiated tissue provides specific information about the state of the tissue including the presence of an abnormality such as a tumor. However the signal strength in such procedures are weak and can be enhanced by infusion of metal-dielectric core nanoparticles.

Metal-dielectric core nanoparticles such as gold-silica nanoshell exhibits phenomenon known as surface-plasmon resonance, which when tuned to a particular wavelength, significantly alters the absorption and scattering coefficient of the medium. In the present study, transmittance and reflectance signals from the nanoparticle infused cancerous lung, irradiated with short pulse laser, for different stages of respiratory volumes, are studied. For modelling heat transfer in tissues with embedded thermally significant blood vessel pairs, Weinbaum-Jiji bioheat model was studied. Energy absorption by nanoshells infused vascularized tissue during laser induced hyperthermia is also studied.

TABLE OF CONTENT

List of Figures

Figure **Page**

List of Tables

Nomenclature

Symbols

AR - aspect ratio

$\Delta A, \Delta V$ - surface area and volume of the control volume, respectively

D - directional weight

E, W, N, S, T, B - east, west, north, south, top and bottom neighbor control volumes of P, respectively

e, w, n, s, t, b - east, west, north, south, top and bottom face of the control volumes of P, respectively.

$\vec{e}_r, \vec{e}_\varphi, \vec{e}_z$ - cylindrical r, φ and z direction base vectors, respectively

G - incident radiation

H - phase function

I - intensity

m - index for direction

N_θ - number of discrete θ directions

N_ϕ - number of discrete ϕ directions

N_r - number of control volumes in radial direction

N_z - number of control volumes in axial direction

P - cell center

R - radius of the cylinder

r - radial direction

q - radiative heat flux

S - source term

s - distance

$\hat{s}$ - direction

T - temperature

Z - height of the cylinder

Greek Symbols

β - extinction coefficient

ε - emissivity

θ - polar angle

ϕ - azimuthal angle

κ_a - absorption coefficient

σ - Stefan-Boltzmann constant (= 5.670×10^{-8} W/m^2 K^4)

σ_s - scattering coefficient

μ, η, ζ - direction cosines in the r, ϕ and z directions, respectively.

ω - scattering albedo

Ω - direction in the MDOM

$\Delta\Omega$ - elemental solid angle

Ψ - dimensionless heat flux

Subscripts

O, T, B - outer, top and bottom walls of the cylinder

b - black/boundary

c - collimated

d - diffuse

N, S, E, W, B, T - Cell centers of neighboring north, south, east, west, bottom and top control volumes, respectively of the control volume having cell center P

n, s, e, w, b, t - north, south, east, west, bottom and top control volume faces, respectively

P - value at the cell center

Superscript

$*$ - dimensionless variable

m - discrete direction

r - radial direction

z - axial direction

Abbreviations

MDOM	Modified Discrete Ordinate Method
FVM	Finite Volume Method
LIH	Laser Induced Hyperthermia
LITT	Laser Induced Thermal Therapy
NPs	Nanoparticles/Nanoshells
REM^2	Radiation Element Method Using Ray Emission Model

Chapter 1

Introduction

1.1 Motivation

Laser-tissue interaction, especially the light transport trough tissues has remained an active area of research. Effect of laser-tissues interaction has been exploited for many therapeutic and diagnostic applications. Its usage has been explored in the treatment of anomalies such as port-wine stain and diseases like cancers. In the recent past, this field has been explored for the direct ablation of tumor and cancer treatment independently as well as in combination with other methods of treatment. Laser induced hyperthermia (LIH) and laser induced thermal therapy (LITT) in combination with chemotherapy and/or radiotherapy have been studied, and successful cases of treatment have been reported. Combined photodynamic - thermal therapy is also emerging as an area of interest. The understanding of heat transfer in a human body during hyperthermia treatment is not only important for better insight of thermoregulatory mechanism and physiological studies, but also for accurate prediction of temperature distribution during therapeutic processes. The present thesis aims at addressing different aspects of laser – tissue interaction, and different therapeutic and diagnostic applications, there efficacy and challenges.

Biological tissues are optically participating media with strong scattering and absorption for thermal radiation. Thermal signals resulting from laser irradiation on a tissue depends on its thermo-physical and optical properties. Thermal signals and temperature field in the tissue are specific to specific set of thermo-physical and optical properties of the tissue. These effects form the basis of new set of diagnosis and treatment for many medical disorders. LIH and LITT involve elevating the temperature of the tissue to obtain desired effects such as coagulation, ablation, increased absorption of certain drugs or increased effect of other modes of treatment like radiotherapy and chemotherapy.

Destroying the tumor by keeping it at an elevated temperature 42^{o}C or above, is the basis of LIH or LITT for cancer treatment. This temperature rise of the tissue can be achieved by laser irradiation. Depending upon the laser power and the exposure time, these procedures are classified into different categories. In LIH, the necrosis (cell death) of the malignant tissue is achieved by keeping it at 42°C - 43°C for a prolonged duration. In a relatively faster procedure, in the LITT, the tissue temperature is raised to 55°C or above. Both LIH and LITT can be achieved by continuous wave and short-pulse lasers.

For understanding the treatment mechanism of LIH and LITT, it is important to understand the thermal response of the tissue during the laser-tissue interaction. During LIH and LITT, skin surface overheating and undesired thermal damage of the healthy tissues remain the two major concerns. The present work is aimed at addressing these concerns.

The objective of both LIH and LITT procedures is to treat the affected tissue while minimizing the thermal damage to the surface of the skin and the surrounding healthy tissues. Laser gets absorbed in the tissue, and the absorption starts from the skin surface in case of external irradiation. Therefore, the maximum thermal energy absorbed is in the skin and the tissue layers (dermis and subcutaneous layers) immediately below the skin surface. During any laser therapy such as LIH and LITT, skin surface cooling is desirable to prevent its damage. Optical window surface contact cooling and cryogenic spray cooling are widely used methods for the skin surface cooling.

Optical windows are materials which are transparent for the wavelength ranging from ultra violet to near infra-red. For applications in LIH and LITT procedures, optical windows are used for providing a transparent and highly conducting contact cooling material. In the present study, the multilayer skin tissue, composed of epidermis, dermis, fatty soft tissue and vascular tissue with embedded blood vessels, is considered. The epidermis contains melanin which is characterized by high absorption of light, and is therefore, the most susceptible for thermal damage during laser heating of tissues. Three different cooling applications considered in the present study are passive contact plate cooling, active contact plate cooling and spray cooling.

For contact cooling application, sapphire is the most preferred material because of its wide range of transparency from red to infrared wavelengths, high strength and high conductivity. Sapphire also has high threshold for optical damage. In the present study, three new optical materials with thermal conductivity comparable or greater than sapphire are examined for suitability for contact cooling applications. The new optical window materials viz., yttrium aluminium garnet, lithium tantalate, and magnesium oxide doped lithium niobate, were selected based on their ability to pass light between wavelength bands of medical laser i.e., between 500 nm to 1200 nm. Other important properties for selection were high conductivity, low reflection loss, stability, hardness, insolubility, non-toxicity, and high threshold for optical damage. A perfect contact between the skin and the optical window is assumed for all cases of contact cooling. In practice, a near perfect contact can be achieved by applying high conductive gels on the skin.

Cryogenic liquids, also known as cryogens, have very low boiling point (typically less than -25°C). The two cryogens selected in the present study are HFO-1234yf or R1234yf (boiling point -30°C) and liquid CO_2 (boiling point -57°C). The selection criteria followed are, low boiling point, low global warming potential and low toxicity. In the present work, only active cooling is considered by means of either keeping constant isothermal condition of optical window material or forced convective condition with extremely low temperature cryogen.

In the present study, a quantitative evaluation of the skin surface cooling during LIH and LITT is performed. The transport of laser in the tissue is characterized by absorption, emission and scattering, and this is governed by the radiative transfer equation (RTE). Numerically, the RTE is solved using the discrete ordinate method (DOM). For a simplified case, the transport of thermal radiation in the tissue is analyzed by the radiation element method using ray emission model.

Energy accumulation in the tissue is not the same throughout in the line of laser irradiation. This non-uniformity causes temperature gradient in the tissue, and hence the conduction heat transfer comes into picture. The metabolic heat generation rate in the tissue is also an important term that needs to be considered. Among various bioheat models, the Pennes bioheat model is extensively used to obtain the temperature distribution in a blood perfused tissue. In vascularized tissues, with embedded blood vessel pairs, Weinbaum-Jiji model is used. To account for the transport of thermal radiation, the volumetric radiative source term, in the form of the divergence of radiative heat flux is incorporated in Pennes bioheat as well as Weinbaum-Jiji models. With radiative information computed using the DOM, the bioheat energy equations are solved using the finite volume method. For both 1-D and 2-D cylindrical tissues, the wavelengths of laser considered are 632.8 nm and 1064 nm.

For a realistic scenario of laser heating of multilayer skin with deep seated vascularized tissue, four optical window materials, two cryogens, and their combinations is modelled for skin surface cooling. A theoretical assessment of suitability of these materials for skin surface cooling application is done. A low temperature level of skin is achieved while raising the internal tissue temperature up to the LIH or LITT range.

The second part of the study aims at selective targeting of tumor during LIH and LITT. In this part of the study, a quantitative analysis of laser irradiation on thermal characteristics, such as temperature, transmittance and reflectance of biological tissues is studied. Thermophysical and optical properties of a malignant tissue are different from a healthy one. Using this fact as the basis of present study, laser induced thermo-optical signal analysis of biological tissues for tumor detection and characterization is done. Transmitted and reflected thermal signals from the laser irradiated tissue provide specific information about the state of the tissue including the presence of a tumor. The signal strength in such procedures are normally weak. Infusion of metal-dielectric core nanoparticles in the tissue helps strengthening the magnitudes of such signals.

Metal-dielectric core nanoparticles such as gold-silica nanoshells exhibits phenomenon known as surface-plasmon resonance, which when tuned to a particular wavelength, significantly alters the absorption and scattering coefficient of the medium. Transmittance and reflectance signals from the lung, irradiated with short pulse laser, for different stages of respiratory volumes, are studied. While Pennes bioheat model predicts temperature evolution in blood perfused tissues, it is not suitable for vascularized tissue with large blood vessels. For modelling heat transfer in tissues with embedded thermally significant blood vessel pairs, Weinbaum-Jiji bioheat model is studied. Energy absorption by nanoshells infused vascularized tissue during laser induced hyperthermia is analyzed. Enhancement in energy absorption by infused nanoshells are reported.

In this thesis, both the issues of skin surface overheating and selective targeting of tumors are analyzed in detail. Different aspects for a successful LIH or LITT procedure are studied. The study covers modelling of collimated radiation in case of external laser irradiation to feasible skin cooling solutions. Enhancement of thermal radiation absorption by infusion of metal core nanoshells for selective targeting of tumors are studied. The thesis presents a detailed numerical solution of LIH and LITT in multilayer tissues in axisymmetric cylindrical and spherical geometries.

1.2 Aim and Objectives

Literature review of different aspects of numerical bioheat transfer, numerical thermal radiative transfer, laser – tissue interaction, laser induced hyperthermia, thermal therapy and nanoparticle assisted thermal therapy are presented in there corresponding chapters. Based on the literature review, the present work is aimed at computational study on thermophysical responses of laser irradiated blood perfused and vascularized tissues. For the chosen aim, following are the objectives:

1. To develop a solver for modelling a coupled bioheat – radiation transfer in a laser irradiated tissue using the finite volume method (FVM) and the radiation element method using ray emission model.
2. To develop a solver for transport of collimated radiation in participating medium using DOM.
3. To study efficacy of different methods of skin surface cooling during LIH and LITT, and to find a better solution for the same.
4. To study nanoparticle assisted LIH and LITT in multilayer tissue – tumor geometry for selective targeting of tumor.
5. To study laser – tissue interaction by analyzing transmittance and reflectance signals from laser irradiated tissue.

1.3 Organization of the Thesis

In the present section, a brief discussion of each chapter is presented. The present chapter, Chapter 1, titled “Introduction”, gives an overview of the present study. The major concerns of LIH and LITT procedures are discussed. Introduction about application of numerical methods in analysis of LIH and LITT processes are also discussed.

A detailed formulation for different problems considered in the present study is presented in chapter 2, titled “Numerical Bioheat Transfer”. Problems involving coupled bioheat – radiation are modelled using the finite volume method (FVM) and the radiation element method using ray emission model. The formulation and solution procedure for collimated radiation in 2-D axisymmetric cylindrical geometry using the DOM are also presented in detail.

Chapter 3, titled "Analysis of Transport of Collimated Radiation", presents the results of distributions of radiative heat flux and incident radiation in a 2-D cylindrical participating medium. The top boundary of the 2-D cylinder is subjected to laser irradiation. Effects of extinction coefficient, scattering albedo and aspect ratio on distributions of radial and axial heat fluxes and incident radiation are reported.

In chapter 4, titled "Convective and Contact Surface Cooling during Laser Induced Thermal Therapy", a theoretical solution of skin surface convective cooling during laser irradiation is presented. Results of studies on contact type cooling during LIH and LITT procedures are presented in section 4.3, titled "Optical Window Contact Cooling during Laser Induced Thermal Therapy". A detailed comparative study of combinations of different optical window materials and cryogenic refrigerants is presented.

Transmittance and reflectance signals resulting from the irradiation of a short-pulse laser and a train of short-pulse laser of nanoparticles infused lung tissue as a function of respiratory lung volume are presented in chapter 5, titled "Transmittance and Reflectance Signals from Laser Irradiated Lung Tissue".

Chapter 6, titled "Nanoparticle Assisted Hyperthermia and Thermal Therapy", deals with the nano-scale effect of embedding a single nanoparticle in a spherical tissue-tumor geometry during LIH and LITT. Macro-scale study with nanoparticles infused in a deep seated vascularized tissue is also presented, and selective targeting of tumor is demonstrated.Finally, in Chapter 7, overall conclusions and scope for the future work are outlined.

Chapter 2

Numerical Bioheat Transfer

2.1 Governing Equations

Modeling heat transfer in a biological system is a complex process. The complexity arises due to the heterogeneous vascular architecture, anisotropic blood flow in the network of arteries and veins, and variable metabolic heat generation rates, thermophysical and optical properties. In addition to that, blood vessel diameter, tissue physiological condition and the dependence of tissue properties on other variables make the study more difficult. In order to study bioheat transfer, many models have been proposed, viz., continuum (Pennes bioheat model) and vascular models (Weinbaum-Jiji model). Each model has its strengths and limitations. In the present chapter, a brief description of the governing equations of heat transfer in biological systems based on two different models is presented. Also, the modeling of laser in participating media, such as biological tissues, which is governed by radiative transfer equation, is discussed.

2.1.1 Pennes bioheat transfer model

Bioheat models are classified as continuum and vascular models. The continuum models are simplified form of the bioheat equations. The continuum models consider the effect of blood flow averaged over a control volume in the conduction equation without consideration of flow through each individual vessel. On the other hand, the vascular models are complex forms of bioheat equations, since flow of blood in each individual vessel is considered in order to predict temperature distributions along the directions of interest.

In mid-20th century, Pennes [Pennes 1948] developed a bioheat equation based on the experimental analysis of human forearm. Pennes bioheat equation is a modified form of the transient heat conduction equation including the effects of blood flow and metabolic heat generation. It is one of the oldest blood perfusion models, which has been used for numerous applications such as therapeutic hyperthermia [Roemer and Cetas 1984], brain hypothermia [Zhu and Diao 2001], tissue ablation [Jaunich *et al.* 2008], and cryosurgery [Rossi and Rabin

2007]. According to Pennes, heat transfer in a tissue occurs only in porous capillary beds, since the microscopic capillaries distribute blood to various tissues where the transfer of nutrients, oxygen and waste products take place. As a result, the densely distributed capillaries provide larger area for heat exchange between blood and tissues. Pennes also introduced a thermal equilibration parameter k' to correlate between the temperature of arterial blood, venous blood and tissue since the temperature of the venous blood leaving tissues and capillaries depends on the extent of heat transfer needed to achieve the thermal equilibrium. While using Pennes bioheat equation, it is commonly assumed that there is a complete thermal equilibrium in the control volume, and the venous blood leaves at the tissue temperature. Also, it is assumed that the arterial temperature has a constant value throughout the tissue, and this is taken as the deep body temperature. This Pennes bioheat equation is given as

$$\rho c\left(\frac{\partial T}{\partial t}\right)=\nabla.\left(k\nabla T\right)+\left(1-k'\right)\omega_b c_b\left[T_a-T\right]+q_m''' \tag{2.1}$$

where t denotes time, ρ_t is the density of the tissue, c_t is the specific heat, k_t is the thermal conductivity of tissue, T_t is the volume averaged tissue temperature, ω_b is the blood perfusion per unit tissue volume per unit time, T_a is the temperature of arterial blood, k' is the thermal equilibration parameter which is either 0 or 1, q_m''' is the rate of volumetric heat generation due to metabolism, subscripts *t*, *b*, *a* and *m* stand for tissue, blood, arterial blood and metabolism, respectively [Bhowmik *et al.* 2013]. Over the years, this model has been criticized, reinvestigated and modified by many investigators because of the various assumptions made by Pennes. A modern and more simplified version of Pennes bioheat equation is given by [Pennes 1948]

$$\rho c\left(\frac{\partial T}{\partial t}\right)=k\left(\nabla^2 T\right)+\rho_b c_b \eta\left(T_a-T\right)+Q_m+Q_s \tag{2.2}$$

where ρ_b is the density, c_b is the specific heat of the blood, T_a is the arterial blood temperature, Q_m is the metabolic heat generation rate, Q_s is the distributed volumetric heat source, and η is the blood perfusion rate.

2.1.2 Weinbaum-Jiji bioheat transfer model

Blood perfusion based models such as Pennes bioheat model and the countercurrent bioheat models such as Weinbaum-Jiji bioheat model are some of the widely used models for bioheat transfer analysis. Bhowmik *et al.* (2013) and Kok *et al.* (2013) have recently summarized basic principles of conventional and newly developed bioheat transfer models. Popularly used models for bioheat transport such as Pennes bioheat equation and its modifications, although simple to implement, are based on several assumptions regarding temperature of blood entering the tissue and the local tissue temperature. Also, since it is based on the concept of blood perfusion rate, it ignores presence of large blood vessels and its effect on overall heat transfer in the tissue [Jaunich *et al.*, 2008; Okajima *et al.*, 2009; Gupta *et al.*, 2010; Das *et al.*, 2013; Paul *et al.*, 2014].

In a peripheral tissue, generally, the blood circulation is carried out by the capillary network and small vessel bleed-off. In these types of tissues, heat transfer modelling with blood perfusion based models performs well. On the other hand, blood flow in vessels have significant effect on heat transfer in nearby regions in a tissue with embedded countercurrent pairs of large blood vessels of typical diameter < 200 µm. Weinbaum *et al.* (1984) proposed a three layer model for bioheat transfer analysis in tissues geometry with large countercurrent blood vessel pairs. Later, because of complexity associated in modelling three-layer system, a new simplified Weinbaum-Jiji (WJ) bioheat model was proposed. The WJ model considered the effect of number of countercurrent blood vessel pairs, the blood velocity, and the blood vessel diameter, while predicting temperature field in vascularized biological tissue. Baish *et al.* (1986) presented a comparative study of unidirectional and countercurrent blood flow bioheat models. Later, Song *et al.* (1987) developed a three-layer model using simplified WJ model, and analyzed the effect of vascular geometry on enhancement of effective conductivity. Numerical implementation of the above discussed bioheat models are presented in the subsequent sections.

For the 2-D cylindrical geometry under consideration (Fig. 2.4a), the WJ model can be expressed as [Weinbaum and Jiji, 1985],

$$\rho c\frac{\partial T}{\partial t}=\frac{1}{r}\frac{\partial}{\partial r}\left(rk_{eff}\frac{\partial T}{\partial r}\right)+\frac{\partial}{\partial z}\left(k_{eff}\frac{\partial T}{\partial z}\right)+Q_m \qquad (2.3)$$

where ρ, c, k_{eff} and Q_m are the density, the specific heat, the effective thermal conductivity and the volumetric metabolic heat generation rate of the tissue, respectively. The effective thermal conductivity of the tissue is a function of different tissue-blood vessel configurations, and is given by [Weinbaum and Jiji, 1985],

$$k_{eff} = k\left[1+\frac{n}{k^2\sigma_{sf}}\left(\pi\rho_b c_b a^2 u\right)^2\right] \tag{2.4}$$

In Eq. 2.4, k, n, ρ_b, c_b, a and u are the thermal conductivity of the tissue, the number of vessel pairs crossing control volume surface per unit area, the density of blood, the specific heat of blood, the vessel radius and the average blood velocity in the counter current vessel pairs, respectively. For two parallel vessels with uniform surface temperature embedded in a very large medium of tissue, the shape factor σ_{sf} provides the information of resistance to the heat transfer and is given by [Chato, 1980; Weinbaum and Jiji, 1985],

$$\sigma_{sf} = \frac{\pi}{\cosh^{-1}\left(l/2a\right)} \tag{2.5}$$

where l is the center to center spacing between the vessel pairs.

2.1.3 Radiative transfer equation

Analysis of volumetric radiation is important in many thermal systems. Diagnostic and therapeutic applications of thermal radiation in the form of infrared lasers are well established. Laser induced thermal therapy and hyperthermia treatments of tumors are examples of its application in bioheat transfer. In most of the bioheat transfer applications, the radiation source is laser [Niemz 2007, Welch *et al.* 2011]. Laser is a collimated radiation and when it travels through an optically participating medium, like a biological tissue, its attenuation gives rise to diffuse radiation, which unlike collimated radiation, manifests and travels in all directions [Modest 2013]. Transport of thermal radiation (diffuse and collimated) in a participating medium is characterized by absorption, emission and scattering, and with these phenomena, it becomes volumetric in nature. The transport of radiation in a participating medium is governed by the radiative transfer equation (RTE). Except for simple geometry and medium, its analytic solution is rare. Numerical methods like the Monte Carlo method [Modest 2013], the discrete transfer method [Rath *et al.* 2003, Mishra *et al.* 2006], the integral equation method [Wu and Wu 1997, 2000], the discrete ordinate method [DOM] [Chandrasekhar 1960, Fiveland 1984, 1987, Kim and Huh, 1999, Lee and Viskanta, 2006] and the finite volume method [FVM] [Raithby and Chui 1990, Chui *et al.* 1992, Chui and Raithby 1992, Murthy and Mathur 2000, Mishra and Sahai 2013] are normally used for the solution of the RTE.

The RTE accounts for the absorption, emission, out-scattering and in-scattering of the radiative energy during its transport in a given direction through a control volume. Emission and in-scattering augment the intensity, and intensity gets attenuated with absorption and out-scattering. This energy balance can be expressed as

$$\begin{pmatrix} \text{Rate of change of} \\ \text{intensity per unit} \\ \text{path length} \end{pmatrix} = \begin{pmatrix} \text{Emitted} \\ \text{intensity} \end{pmatrix} - \begin{pmatrix} \text{Absorbed} \\ \text{intensity} \end{pmatrix} - \begin{pmatrix} \text{Out-scattered} \\ \text{intensity} \end{pmatrix} + \begin{pmatrix} \text{In-scattered} \\ \text{intensity} \end{pmatrix} \tag{2.6}$$

Mathematically, the RTE is given by [Modest 2013],

$$\left(\frac{1}{c}\right)\frac{\partial I(r,s)}{\partial t} + \frac{dI(r,s)}{ds} = \kappa I_b(r) - \beta I(r,s) + \frac{\sigma_s}{4\pi}\int_{4\pi} I_-(s_i)\Phi(s_i,s)\,d\Omega' \tag{2.7}$$

where c is the speed of light, $I(r,s)$ is the radiation intensity at a given location indicated by position vector r, in the direction s, travelling through a participating medium. In Eq. 2.7, I_- is the incident intensity and I_b is the blackbody intensity. In steady-state form, RTE is given as [Modest 2013],

$$\frac{dI(r,s)}{ds} = \kappa I_b(r) - \beta I(r,s) + \frac{\sigma_s}{4\pi}\int_{4\pi} I_-(s_i)\Phi(s_i,s)\,d\Omega' \tag{2.8}$$

The sum of the absorption coefficient κ and the scattering coefficient σ_s is the extinction coefficient $\beta = \kappa + \sigma_s$ [Mishra *et al.* 2006, Modest 2013, Muthukumaran and Mishra 2008, Sarma *et al.* 2005].

2.1.4 Energy equation

When the volumetric radiative source term, i.e., the divergence of radiative heat flux $\nabla \cdot q_r$ is accounted, the Pennes bioheat equation takes the form

$$\rho c_p \frac{\partial T}{\partial t} = k\left[\frac{1}{r}\frac{\partial}{\partial r}\left(r\frac{\partial T}{\partial r}\right) + \frac{\partial^2 T}{\partial z^2}\right] + \eta_b \rho_b c_{pb}\left(T_a - T\right) + Q_m - \nabla \cdot q_r \qquad (2.9)$$

This equation (Eq. 2.9) is solved numerically to model coupled bioheat conduction-radiation scenario. In the next section, a detailed solution procedure with numerical methods for bioheat equation and radiative transfer equation are discussed.

2.2 Solution Procedure

A general solution procedure in the form of a flow chat is presented in Fig. 2.1. In most of the simulations in the present work, this procedure have been followed.

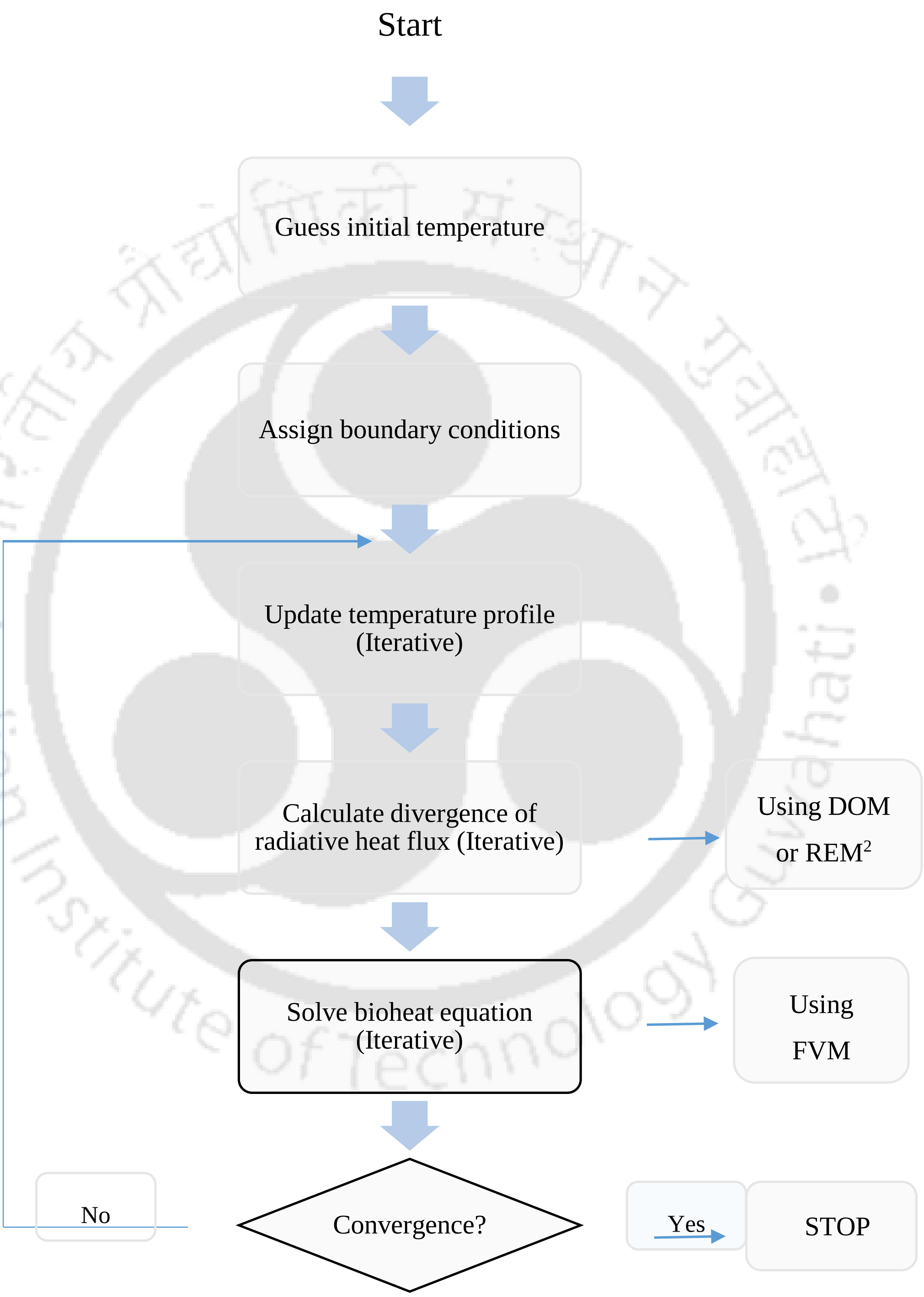

Figure 2.1: Flowchart of the solution procedure.

2.3 Finite Volume Method

Towards, the numerical solution of bioheat energy equation, we follow the procedure of the finite volume method (FVM) [Versteeg and Malalasekera, 1995]. Here, a simple 1-D geometry is considered for explaining the procedure.

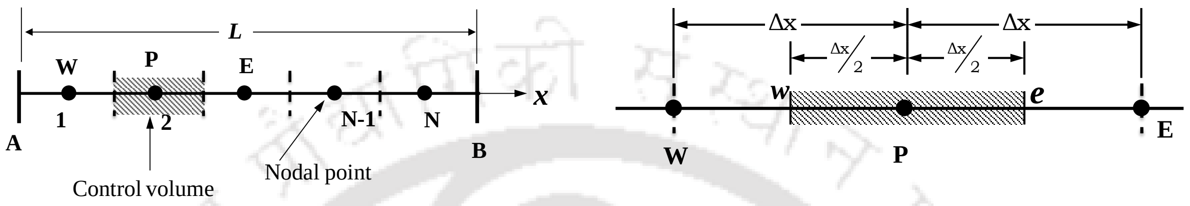

(a) (b)

Figure 2.2: Schematics of the 1-D (a) discretized solution space and (b) description of the 1-D FVM control volume.

With reference to Figs. 2.2a and 2.2b, integrating Eq. 2.2 over finite time step Δt and control volume ΔV, gives,

$$\int_{t}^{t+\Delta t}\left(\int_{\Delta V}\rho c_{p}\frac{\partial T}{\partial t}dV\right)dt=\int_{t}^{t+\Delta t}\left(\int_{\Delta V}\frac{\partial\left(k\frac{\partial T}{\partial x}\right)}{\partial x}dV\right)dt+\int_{t}^{t+\Delta t}\left(\int_{\Delta V}\left(\eta_{b}\rho_{b}c_{pb}\left(T_{a}-T\right)+Q_{m}+Q_{s}\right)dV\right)dt \tag{2.10}$$

After simplification, in the discrete form, with explicit approach, Eq. 2.10 becomes

$$T_{P}^{n+1}=T_{P}^{n}+\frac{\Delta t\,k}{\rho c_{P}\Delta x}\left(T_{E}^{n}-2T_{P}^{n}+T_{W}^{n}\right)+\frac{\Delta t}{\rho c_{P}}\left[\eta_{b}\rho_{b}c_{Pb}\left(T_{a}^{n}-T_{P}^{n}\right)+Q_{m}+Q_{s}\right] \tag{2.11}$$

where the variables with suffix P are the volume averaged values at the center of the discrete control volume (Fig. 2.2a), and those with suffixes E and W are the same at its east and west neighboring nodes.

As shown in the solution procedure flow chart (Fig. 2.1), the bioheat equation with divergence of radiative heat flux $\nabla \cdot q_r$ as a source term is solved iteratively till the convergence is achieved. The details of discretization process and other FVM details are omitted for brevity, as they are standard procedures [Versteeg and Malalasekera, 1995]. In case of 2-D axisymmetric cylindrical geometry, the same procedure is followed.

2.4 Radiation Element Method using Ray Emission Model (REM^2)

Originally proposed by Maruyama *et al.* [1993, 1997, 2004], the Radiation element method by ray emission model (REM^2) is a method for solving radiation heat transfer. Compared with other existing methods, REM^2 uses deterministic approach for faster speed against stochastic approach used in Monte Carlo method [Modest 2013]. REM^2 guarantees energy conservation and is free from ray effect. The REM^2 can easily be applied to complex systems having specular or diffuse surfaces, non-gray participating medium and anisotropic scattering media. REM^2 has been applied to a wide range of problems with results showing improved computational time over other methods [Maruyama 1993, 1997, 2004].

In the REM^2, the (RTE) is written as [Sakurai 2010]

$$\frac{1}{\beta}\frac{dI_d(\hat{s})}{dS} = -I_d(\hat{s}) + (1-\omega)I_b(\hat{s}) + \frac{\omega}{4\pi}\int_{4\pi} I_d(\vec{r},\hat{s}')\Phi\left(\hat{s}' \to \hat{s}\right)d\Omega' \tag{2.12}$$

where β and ω are extinction coefficient and scattering albedo, respectively. Here, s is the path length in the direction $\hat{s}$, and $\Phi(\hat{s}' \to \hat{s})$ is the phase function from $\hat{s}'$ to $\hat{s}$. I_d is the diffuse part of radiative intensity and I_b is black body radiative intensity.

For any radiation element i, considering contributions from all surface and volume elements, the radiative energy $Q_{J,i}$, and the net heat generation rate $Q_{X,i}$, are given by [Mruyama 1993, 1997, 2004, Sakurai 2010],

$$Q_{J,i} = A_i^R \varepsilon_i n^2 \sigma T_i^4 + \sum_{j=1}^{M} F_{j,i}^D Q_{J,j} \tag{2.14}$$

$$Q_{X,i} = A_i^R \varepsilon_i n^2 \sigma T_i^4 - \sum_{j=1}^{M} F_{j,i}^A Q_{J,j} \tag{2.15}$$

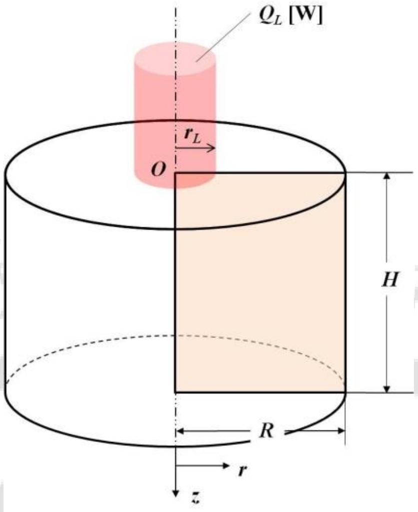

Figure 2.3: Two-dimensional axisymmetric cylinder model.

where A_i^R is effective radiation area, ε_i is emissivity, n is the refractive index, σ is the Stephan-Boltzmann constant, $F_{j,i}^D$ is the diffuse scattering view factor, and $F_{j,i}^A$ is the absorption view factor from jth to ith element. These view factors are obtained by the extinction view factor $F_{i,j}^E$ as

$$F_{i,j}^D = \frac{\omega_j^D}{\left(1-\omega_j^S\right)} F_{i,j}^E \tag{2.16}$$

$$F_{i,j}^A = \frac{\varepsilon_j}{\left(1-\omega_j^S\right)} F_{i,j}^E \tag{2.17}$$

where superscript S and D mean specular and diffuse, respectively. The extinction view factor is defined as [Mruyama 1993, 1997, 2004, Sakurai 2010],

$$F_{i,j}^E = \frac{1}{\pi A_i^R} \int_{4\pi} f_i^j(\hat{s}) A_i(\hat{s}) \left[1-\exp\left(-\beta_i^D S_i\right)\right] \times \left[1-\exp\left(-\beta_j^D S_j\right)\right] d\Omega \tag{2.18}$$

where $f_i^j(\hat{s})$ is fraction of energy emitted from i^{th} element in the direction $\hat{s}$ which reaches j^{th} element. A_i is projected cross-section of i^{th} element from the direction $\hat{s}$. S_i is effective thickness of i^{th} element. The effective radiation area is given by [Mruyama 2004, Sakurai 2010],

$$A_i^R = \sum_{l=1}^{L} \left[1 - \exp\left(-\beta^D \Delta x_i / \mu_l\right)\right] \mu_l \Omega_l \tag{2.19}$$

The scaling function is used to approximate anisotropic scattering by using zeroth-order delta function approximation as [Mruyama 2004, Sakurai 2010],

$$\beta^D = \beta\left(1 - \omega a_1 / 3\right) \tag{2.20}$$

$$\omega^D = \frac{\omega\left(1 - a_1 / 3\right)}{1 - \omega a_1 / 3} \tag{2.21}$$

where a_1 is forward scattering parameter, and value of a_1 for biological tissues is set to Eq. 2.7 in present study. Finally the value of radiative heat flux is be obtained by [Mruyama 2004, Sakurai 2010],

$$q_r(x) = \int_0^X Q_X(x) / S(x)\, dx \tag{2.22}$$

2.5 Discrete Ordinate Method

In the following, the formulation of the DOM is provided. Consideration is given to a 2-D axisymmetric cylindrical enclosure (Fig. 3.1a) having radius R and height Z. The cylinder with diffuse-gray boundaries contains an absorbing, emitting and scattering non-isothermal medium. The top boundary of the medium is subjected to collimated radiation (Fig. 2.4a) having intensity $I_{c,\max}$, and is thus, the source of the collimated radiation in the medium. Along its direction of incidence, while travelling from the top $(z = Z)$ boundary towards the bottom $(z = 0)$ boundary, at any location s, attenuation of the collimated intensity I_c is given by

$$\frac{\partial I_c}{\partial s} = -\beta I_c \tag{2.23}$$

where β is the extinction coefficient.

The attenuated component of the collimated intensity manifests in the form of diffuse intensity I_d, which unlike the collimated intensity I_c, spreads in all directions in the 4π spherical space. Therefore, within the medium, intensity I consists of both collimated I_c and diffuse I_d components, i.e.,

$$I = I_c + I_d \tag{2.24}$$

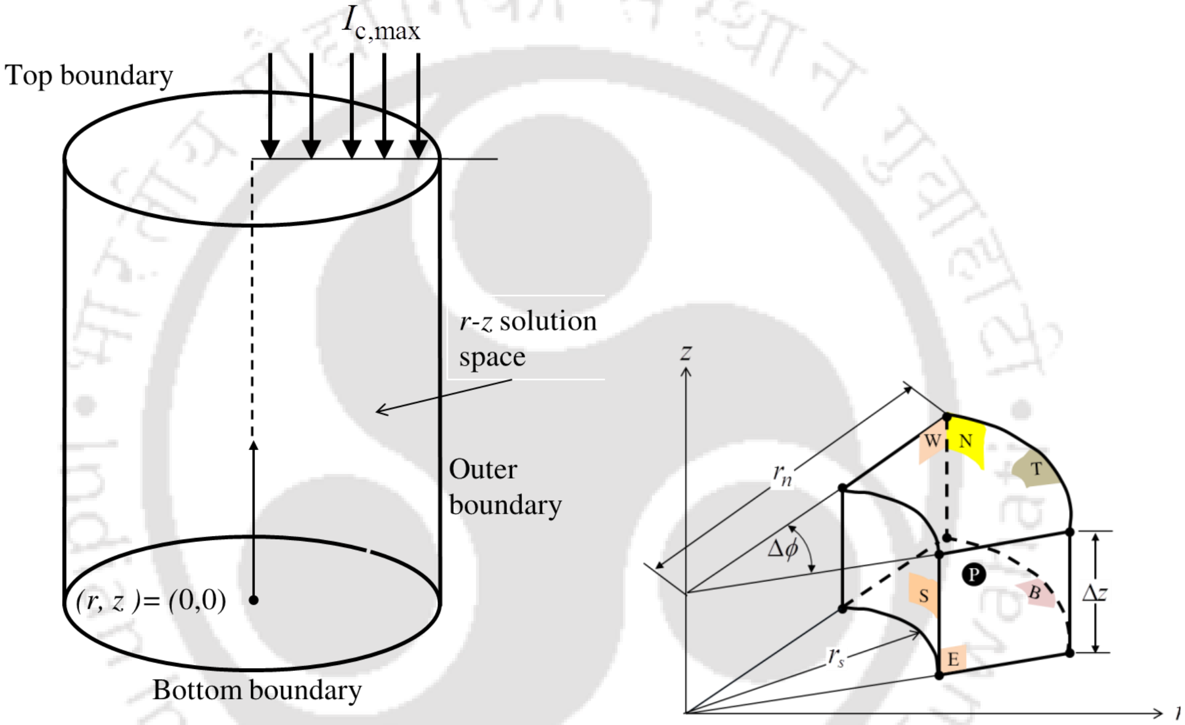

(a) (b)

Figure 2.4: Schematic of (a) 2-D concentric cylindrical enclosure with cylindrical coordinate system and computational domain and (b) 3-D control volume needed for marching in angular space.

With reference to the coordinate system also shown in Fig. 2.4a, with $\theta\left(0 \le \theta \le \pi\right)$ as the polar angle and $\phi\left(0 \le \phi \le 2\pi\right)$ as the azimuthal angle, for any discrete direction $\hat{s} = \left(\sin\theta\cos\phi\right)\vec{e}_r + \left(\sin\theta\sin\phi\right)\vec{e}_\phi + \left(\cos\theta\right)\vec{e}_z$, the RTE is given by [Modest 2013, Mishra *et al.* 2006],

$$\frac{\partial I}{\partial s} = -\beta I + \kappa_a I_b + \frac{\sigma_s}{4\pi}\int_{\Omega'=4\pi} I(s')\Phi(s,s')d\Omega' \tag{2.25}$$

where s is the distance in the direction $\hat{s}$, κ_a is the absorption coefficient, σ_s is the scattering coefficient and $\Phi(s,s')$ is the scattering phase function. Substitution of $I = I_c + I_d$ from Eq. 2.23 and $\frac{\partial I_c}{\partial s} = -\beta I_c$ from Eq. 2.24 in Eq. 2.25 results in [Modest 2013, Mishra *et al.* 2006],

$$\frac{\partial I_d}{\partial s} = -\beta I_d + S_t \tag{2.26}$$

where the total source term S_t consists of the source term S_c due to collimated intensity and source term S_d due to diffuse intensity. For an absorbing, emitting and isotropically scattering medium $H(s,s') = 1$, and in this case, the source term due to collimated intensity is given by,

$$S_c = \frac{\sigma_s}{4\pi} G_c \tag{2.27}$$

In Eq. 2.27, the incident radiation G_c due to collimated intensity is obtained from

$$G_c = I_c = I_{c,\max} \exp(-\beta s_c) \tag{2.28}$$

where $I_{c,\max}$ is the magnitude of the collimated intensity at the top boundary $(z = Z)$ and s_c is the physical distance travelled by the collimated intensity along its direction of incidence.

In terms of local temperature T, with Plank blackbody intensity $I_b = \frac{\sigma T^4}{\pi}$, where $\sigma = 5.67\times10^{-8}$ Wm^{-2}K^{-4} is Stefan-Boltzmann constant, the source term due to diffuse intensity is given by [Modest 2013, Mishra *et al.* 2006],

$$S_d = k_a I_b + \frac{\sigma_s}{4\pi} G_d = (1-\omega)\beta I_b + \frac{\omega\beta}{4\pi} G_d \tag{2.29}$$

where $\omega\left(=\frac{\sigma_s}{\beta}\right)$ is the scattering albedo and G_d is the incident radiation due to diffuse intensity. With no variations in surface radiative properties and boundary conditions along the circumferential ϕ direction, mathematically the present problem is a 2-D axisymmetric one. Thus, as shown in Fig. 2.4a, the solution plane is the $r-z$ plane. At any (r,z) location, the diffuse intensities I_d exist in the 4π spherical space. For calculation of the incident radiation G_d in Eq. 2.29, distribution of discrete diffuse intensities I_d over the 4π spherical space has to be known. Following the steps of [Mishra *et al.* 2006] of the DOM, with distributions of the diffuse intensity I_d^m in all discrete directions known, G_d needed in Eq. 2.7 is computed from the following [Mishra *et al.* 2006],

$$G_d = \int_{\Omega=0}^{4\pi} I_d(\theta,\phi)\,d\Omega \approx \sum_{l=1}^{N_\phi}\sum_{k=1}^{N_\theta} I_d^m \Delta\Omega^m \tag{2.29}$$

where N_θ and N_ϕ are the divisions of the polar $(0 \le \theta \le \pi)$ and the azimuthal $(0 \le \phi \le 2\pi)$ space, respectively. In Eq. 2.29, $\Delta\Omega^m$ is the directional weight associated with the diffuse intensity I_d^m. With total solid angle 4π divided into $N_\theta \times N_\phi$ directions, $\Delta\Omega^m$ is computed from the following [Mishra *et al.* 2006]

$$\Delta\Omega^m = 2\sin\theta^m \sin\left(\frac{\Delta\theta}{2}\right)\Delta\phi^m \tag{2.30}$$

Diffuse intensity I_d needed in Eq. 2.30 is computed from the solution of Eq. 2.26. In the DOM approach for the cylindrical geometry (Fig. 2.4a) considered in the present work, Eq. 2.26 is written as

$$\frac{1}{r}\frac{\partial}{\partial r}[\mu r I_d] + \frac{\partial}{\partial z}[\zeta I_d] - \frac{1}{r}\frac{\partial}{\partial \phi}[\eta I_d] = -\beta I_d + S_t \tag{2.31}$$

where $\mu = \sin\theta\cos\phi$, $\eta = \sin\theta\sin\phi$ and $\zeta = \cos\theta$ are the direction cosines, respectively.

In the DOM, to proceed with the solution, the RTE given in Eq. 2.31 is written for a discrete direction $\left(\Omega^m = \left(\theta^m, \phi^m\right)\right)$ having index m, and is then integrated over the 3-D elemental control volume (Fig. 2.4b) [Mishra *et al.* 2011] having center P.

$$\int_{\Delta V}\frac{1}{r}\frac{\partial}{\partial r}\left[\mu^m r I_d^m\right]dV+\int_{\Delta V}\frac{\partial}{\partial z}\left[\zeta^m I_d^m\right]dV \\ -\int_{\Delta V}\frac{1}{r}\frac{\partial}{\partial\phi}\left(\eta^m I_d^m\right)dV+\int_{\Delta V}\beta I_d^m dV=\int_{\Delta V}S^m dV \tag{2.41}$$

After simplification, Eq. (2.41) can be written as [Mishra *et al.* 2006, 2011],

$$\mu^m\left(\Delta A_n I_{d,n}^m-\Delta A_s I_{d,s}^m\right)+\zeta^m\left(\Delta A_t I_{d,t}^m-\Delta A_b I_{d,b}^m\right) \\ -\left(\Delta A_e \eta_e^m I_{d,e}^m-\Delta A_w \eta_w^m I_{d,w}^m\right)+\beta I_{d,P}^m\Delta V=S_P^m\Delta V \tag{2.42}$$

where in the direction having index m, $I_{d,n}^m$, $I_{d,s}^m$, $I_{d,t}^m$, $I_{d,b}^m$, $I_{d,e}^m$ and $I_{d,w}^m$ are the intensities at the north, south, top, bottom, east and west faces of the control volume (Fig. 2.4b), respectively. In Eq. 2.42, I_P^m and S_P^m are the volume averaged intensities and source term in the direction m, respectively. It is to be noted that in the DOM [Mishra *et al.* 2010, 2011, 2012, Mishra and Krishna 2011], for a given polar angle θ^m, the variation of intensity with azimuthal angle is the same as the along the circumferential direction. In [Mishra *et al.* 2010, 2011, 2012, Mishra and Krishna 2011], the two azimuthal angles are termed as *angular* and *spatial* azimuthal angles, respectively. Thus, for marching in the angular space, a 1-D cylindrical geometry, the control volumes become 2-D and as shown in Fig. 2.4b, in a 2-D cylindrical geometry, it becomes 3-D. It is to be further noted that in solving the RTE, spatially the solution space for the 2-D cylinder (Fig. 2.4a) is a 2-D rectangular $(r-z)$ domain.

The direction cosines appearing in Eqs. (2.41) and (2.42) are the following

$$\mu^m=\sin\theta^m\cos\phi^m,\ \zeta^m=\cos\theta^m,\ \eta_e^m=\sin\theta^m\sin\left(\phi^m+\frac{\Delta\phi}{2}\right), \\ \eta_w^m=\sin\theta^m\sin\left(\phi^m-\frac{\Delta\phi}{2}\right) \tag{2.43}$$

With reference to the control volume shown in Fig. 2.4b, area terms and volume appearing in Eq. 2.42 above are the following [Mishra *et al.* 2006, 2011],

$$\Delta A_n = r_n \Delta\phi \times \Delta Z, \quad \Delta A_s = r_s \Delta\phi \times \Delta Z, \quad \Delta A_e = \Delta A_w = (r_n - r_s) \times \Delta Z,$$
$$\Delta A_t = \Delta A_b = \frac{\pi (r_n^2 - r_s^2)}{2N_\phi}, \Delta V = \pi (r_n^2 - r_s^2) \Delta Z / 2N_\phi \tag{2.44}$$

In any direction having index m, Eq. 2.42 contains six facial intensities $I_{d,n}^m, I_{d,s}^m\ I_{d,t}^m, I_{d,b}^m$, $I_{d,e}^m$, $I_{d,w}^m$, and one nodal intensity I_P^m. To calculate the discrete diffuse intensities over the 4π spherical space, nodal intensities I_P^m in any direction is calculated in terms of known nodal intensities of the surrounding control volumes. At any point in the medium, the distribution of the nodal intensity is known when intensities are traced from all four quadrants. In any quadrant, tracing of intensities starts from the corners of the solution space. For the corner control volumes, the nodal intensities are written in terms of boundary facial intensities that are known from the radiative boundary conditions. With this, to reduce the number of unknowns, the nodal intensities are related with the facial intensities through a step scheme. Following [Mishra *et al.* 2012], for marching from four quadrants, intensity relations are the following:

$$\left.\begin{array}{lll} I_{d,n}^m = I_{d,P}^m, & I_{d,s}^m = I_{d,S}^m, & I_{d,t}^m = I_{d,P}^m, \\ I_{d,b}^m = I_{d,B}^m, & I_{d,e}^m = I_{d,P}^m, & I_{d,w}^m = I_{d,W}^m \end{array}\right\} \begin{array}{c} \text{for } \mu^m > 0, \zeta^m > 0 \\ \text{(First quadrant)} \end{array} \tag{2.45a}$$

$$\left.\begin{array}{lll} I_{d,n}^m = I_{d,N}^m, & I_{d,s}^m = I_{d,P}^m, & I_{d,t}^m = I_{d,P}^m, \\ I_{d,b}^m = I_{d,B}^m, & I_{d,e}^m = I_{d,P}^m, & I_{d,w}^m = I_{d,W}^m \end{array}\right\} \begin{array}{c} \text{for } \mu^m < 0, \zeta^m > 0 \\ \text{(Second quadrant)} \end{array} \tag{2.45b}$$

$$\left.\begin{array}{lll} I_{d,n}^m = I_{d,N}^m, & I_{d,s}^m = I_{d,P}^m, & I_{d,t}^m = I_{d,T}^m, \\ I_{d,b}^m = I_{d,P}^m, & I_{d,e}^m = I_{d,P}^m, & I_{d,w}^m = I_{d,W}^m \end{array}\right\} \begin{array}{c} \text{for } \mu^m < 0, \zeta^m < 0 \\ \text{(Third quadrant)} \end{array} \tag{2.45c}$$

$$\left.\begin{array}{lll} I_{d,n}^m = I_{d,P}^m, & I_{d,s}^m = I_{d,S}^m, & I_{d,t}^m = I_{d,T}^m, \\ I_{d,b}^m = I_{d,P}^m, & I_{d,e}^m = I_{d,P}^m, & I_{d,w}^m = I_{d,W}^m \end{array}\right\} \begin{array}{c} \text{for } \mu^m > 0, \zeta^m < 0 \\ \text{(Fourth quadrant)} \end{array} \tag{2.45d}$$

where $I_{d,W}^m, I_{d,E}^m, I_{d,N}^m, I_{d,S}^m, I_{d,T}^m$ and $I_{d,B}^m$ are the nodal intensities in the six control volumes surrounding the control volume with center P. With nodal intensities related with facial intensities as given in Eq. 2.45, depending upon the quadrants, the nodal intensity $I_{d,P}^m$ is written in terms of relevant known nodal intensities $I_{d,W}^m, I_{d,E}^m, I_{d,N}^m, I_{d,S}^m, I_{d,T}^m$ and $I_{d,B}^m$ of the neighboring control volumes. From Eq. 2.42 and Eq. 2.45, depending upon the quadrants, expressions for nodal intensity $I_{d,P}^m$ are the following [Mishra *et al.* 2011, 2012],

$$I_{d,P}^{m} = \frac{\mu^{m}\Delta A_{s} I_{d,S}^{m} + \zeta^{m}\Delta A_{b} I_{d,B}^{m} - \Delta A_{w}\eta_{w}^{m} I_{d,W}^{m} + \Delta V S_{P}^{m}}{\mu^{m}\Delta A_{n} + \zeta^{m}\Delta A_{t} - \Delta A_{e}\eta_{e}^{m} + \beta\Delta V}, \quad \text{for } \mu^{m} > 0, \zeta^{m} > 0 \text{ (First quadrant)} \tag{2.46a}$$

$$I_{d,P}^{m} = \frac{-\mu^{m}\Delta A_{n} I_{d,N}^{m} + \zeta^{m}\Delta A_{b} I_{d,B}^{m} - \Delta A_{w}\eta_{w}^{m} I_{d,W}^{m} + \Delta V S_{P}^{m}}{-\mu^{m}\Delta A_{s} + \zeta^{m}\Delta A_{t} - \Delta A_{e}\eta_{e}^{m} + \beta\Delta V}, \quad \text{for } \mu^{m} < 0, \zeta^{m} > 0 \text{ (Second quadrant)} \tag{2.46b}$$

$$I_{d,P}^{m} = \frac{-\mu^{m}\Delta A_{n} I_{d,N}^{m} - \zeta^{m}\Delta A_{t} I_{d,T}^{m} - \Delta A_{w}\eta_{w}^{m} I_{d,W}^{m} + \Delta V S_{P}^{m}}{-\mu^{m}\Delta A_{s} - \zeta^{m}\Delta A_{b} - \Delta A_{e}\eta_{e}^{m} + \beta\Delta V}, \quad \text{for } \mu^{m} < 0, \zeta^{m} < 0 \text{ (Third quadrant)} \tag{2.46c}$$

$$I_{d,P}^{m} = \frac{\mu^{m}\Delta A_{s} I_{d,S}^{m} - \zeta^{m}\Delta A_{t} I_{d,T}^{m} - \Delta A_{w}\eta_{w}^{m} I_{d,W}^{m} + \Delta V S_{P}^{m}}{\mu^{m}\Delta A_{n} - \zeta^{m}\Delta A_{b} - \Delta A_{e}\eta_{e}^{m} + \beta\Delta V}, \quad \text{for } \mu^{m} > 0, \zeta^{m} < 0 \text{ (Fourth quadrant)} \tag{2.46d}$$

It is to be noted that for the faces of control volumes lying along the boundaries of the enclosure, for the given marching direction, upstream nodal intensities are not available. Thus for those control volumes, in the expressions of $I_{d,P}^{m}$ given in Eq. 2.46, facial intensities, $\left(I_{d,n}^{m}, I_{d,s}^{m}, I_{d,t}^{m}, I_{d,b}^{m}, I_{d,e}^{m}, I_{d,w}^{m}\right)$ take the place of nodal intensities $\left(I_{d,W}^{m}, I_{d,E}^{m}, I_{d,N}^{m}, I_{d,S}^{m}, I_{d,T}^{m}, I_{d,B}^{m}\right)$. For such control volumes, the upstream facial intensities are calculated from the radiative boundary condition. For a diffusely emitting and reflecting boundary having emissivity ε_{b} and temperature T_{b}, the facial boundary intensity is calculated from

$$I_{b}^{m} = \frac{\varepsilon_{b}\sigma T_{b}^{4}}{\pi} + \frac{1-\varepsilon_{b}}{\pi} \sum_{m', D_{b}^{m'} < 0} \left\{ \left(I_{d,b}^{m'}\right) \left|D_{d,b}^{m'}\right| + \left(I_{c,b}^{m'}\right) \cos\theta_{c} \right\} \quad \text{for} \quad D_{d,b}^{m} > 0 \tag{2.47}$$

where the first and the second terms on the right hand side of Eq. 2.47 represent the emitted and the reflected components of the net intensity, respectively. It is to be noted that if the boundary under consideration is the bottom one, in Eq. 2.47, $I_{c,b}^{m'}$ will appear. For other boundaries, it is not relevant. $I_{c,b}^{m'}$ accounts for the attenuated collimated intensity striking the bottom boundary and its magnitude is given by Eq. 2.28. In Eq. 2.47, the directional weight D_{b}^{m} is given by [Mishra *et al.* 2006, 2011],

$$D_{d,b}^{m} = \int_{\Delta\Omega^{m}} \left(\vec{\Omega} \cdot \vec{n}_{b}\right) d\Omega \tag{2.48}$$

where at the bounding cylindrical wall, $\vec{n}_{b}$ is the unit normal vector pointing towards the medium.

In the absence of other modes of heat transfer, i.e., conduction and convection, with top boundary of the 2-D cylinder as the radiation source, the problem under consideration belongs to the class of radiative equilibrium, i.e., $\nabla\cdot q = 0,$ where q is the radiative heat flux. Radiative heat flux q varies along radial r and axial z directions. From the knowledge of distributions of the facial intensities along $r-$ and $z-$faces of a control volume, radiative heat fluxes along these faces are calculated from the following [Mishra *et al.* 2006, 2011],

$$q_r = \int_{\Omega=4\pi} I_d\left(\vec{\Omega}\cdot\vec{n}_n\right)d\Omega \approx \sum_{l=1}^{N_\phi}\sum_{k=1}^{N_\theta} I_d^m D_{d,n}^m, \quad \text{along the } r\text{-face} \tag{2.49}$$

$$\begin{aligned} q_z = q_{d,z} + q_{c,z} &= \int_{\Omega=4\pi} I_d\left(\vec{\Omega}\cdot\vec{n}_t\right)d\Omega + I_c\cos\theta_c \\ &= \sum_{l=1}^{N_\phi}\sum_{k=1}^{N_\theta}\left(I_d^m D_{d,t}^m\right) + I_c\cos\theta_c, \quad \text{along the } z\text{-face} \end{aligned} \tag{2.50}$$

where the directional weights D_n^m and D_t^m are computed from the following

$$D_n^m = \cos\phi^m \sin\left(\frac{\Delta\phi}{2}\right)\left[\Delta\theta - \cos 2\theta^m \sin\left(\Delta\theta\right)\right] \tag{2.51}$$

$$D_t^m = \left(\sin\theta^m \cos\theta^m \sin\Delta\theta\right)\Delta\phi \tag{2.52}$$

For generality, in the following, results are presented in non-dimensional form. Collimated intensity is the source of radiation, and thus the maximum heat flux $q_{c,\max} = I_{c,\max}\cos\theta_c$ due to collimated radiation is used for non-dimensionalisation. With this, the radial Ψ_r and the axial Ψ_z non-dimensional heat fluxes are defined as [Mishra *et al.* 2011],

$$\Psi_r = \frac{q_{d,r}}{q_{c,\max}}, \quad \Psi_z = \frac{q_{d,z} + q_{c,z}}{q_{c,\max}} \tag{2.53}$$

In a radiative equilibrium problem, $\nabla\cdot q$ =0, i.e.

$$\nabla\cdot q = \kappa_a\left(4\pi\frac{\sigma T^4}{\pi} - G\right) = 0 \tag{2.54}$$

Thus, the incident radiation is the indicator of temperature/emissive power of the medium. Non-dimensionalisation of the incident radiation G^* has also been done with respect to the maximum value of incident radiation $G_{c,\max} = I_{c,\max}$ which is due to the collimated radiation at the boundary of incidence. Non-dimensionalisation is given by [Mishra *et al.* 2011],

$$G_r^* = \frac{G_{d,r}}{G_{c,\max}}, G_z^* = \frac{G_{z,d} + G_{z,c}}{G_{c,\max}} \tag{2.55}$$

2.6 Closure

In the present chapter, a detailed formulations of FVM, REM^2, and DOM for 1-D planner and 2-D axisymmetric cylindrical geometry were presented. Solvers for bioheat transfer models, namely Pennes bioheat and Weinbaum-Jiji bioheat models were developed using FVM. Radiative transfer equation was modelled using REM^2 and DOM for 2-D axisymmetric cylindrical geometry. The formulations presented in this chapter are utilized for solving different aspects of bioheat transfer of laser irradiated tissue in corresponding chapters.

Chapter 3

Radiative Transport in Participating Medium Subjected to Collimated Radiation

3.1 Theory and Formulation

This chapter deals with the numerical analysis of radiative transport in a 2-D axisymmetric cylindrical enclosure containing absorbing, emitting and scattering medium. The participating medium receives collimated radiation from the top boundary of the enclosure. Attenuation of the collimated radiation in the medium gives rise to the diffuse radiation. Thus, the governing radiative transfer equation accounts for both collimated and diffuse radiation. The radiative transfer equation is solved using the MDOM. Effects of extinction coefficient, scattering albedo and aspect ratio on radial and axial distributions of heat flux and incident radiation are studied. In all cases, results are validated against those available in the literature. Modified discrete ordinate method has been found to provide accurate results.

Analysis of volumetric radiation is important in many thermal systems. If its consideration is paramount in the design and analysis of high temperature devices like boilers, furnaces, porous burners, insulations, etc. [Borjini *et al.* 2003, 2007, Baburić *et al.* 2005, Filho and Pimenta 2000, Johansson *et al.* 2010, Marakis*et al.* 2011, Veiseh and Hakkaki-Fard 2009], its importance in low temperature applications like bioheat transfer is also immense [Jaunich *et al.* 2008, Khanafer *et al.* 2007, Kim and Guo 2004, Liu *et al.* 1997, Muthukumaran and Mishra 2008, 2009, Niemz 2007, Sakurai *et al.* 2010, Welch *et al.* 2011]. Diagnostic and therapeutic applications of thermal radiation in the form of infrared lasers are well established. Laser induced thermal therapy and hyperthermia treatments of tumors are examples of its application in bioheat transfer.

In most of the bioheat transfer applications, the radiation source is laser [Niemz 2007, Welch *et al.* 2011]. Laser is a collimated radiation. When its travels through an optically participating medium, like a biological tissue, its attenuation gives rise to diffuse radiation, which unlike collimated radiation, manifests and travels in all directions [Modest 2013]. Transport of thermal radiation (diffuse and collimated) in a participating medium is characterized by absorption, emission and scattering, and with these phenomena, it becomes volumetric in nature, and the governing radiative transfer equation (RTE) turns out to be an integro-differential one [Modest 2013]. Except for simple geometry and medium, its analytic solution is rare. Numerical methods like the Monte Carlo method [Modest 2013], the discrete transfer method [Rath *et al.* 2003, Mishra *et al.* 2006] the integral equation method [Wu and Wu 1997, 2000], the discrete ordinate method [DOM] [Chandrasekhar 1960, Fiveland 1984, 1987, Kim and Huh, 1999, Lee and Viskanta, 2006] and the finite volume method [FVM] [Raithby and Chui 1990, Chui *et al.* 1992, Chui and Raithby 1992, Murthy and Mathur 2000, Mishra and Sahai 2013] are normally used for the solution of the RTE.

Transport of collimated radiation in planar and cylindrical geometry has been studied by many researchers [Crosbie and Lee 1987, Hsu *et al.* 1999, Sarma *et al.* 2005, Singh and Mishra 2007, Wu and N. R. Ou 2002, Wu and Wu 1997, 2000]. They have done the study with different methods. Analysis of transport of radiation in even a 1-D cylindrical geometry is relatively difficult. In this, unlike a 1-D planar geometry, radiation is azimuthally not symmetric. Thus, in a 1-D cylinder, though the spatial marching is needed in only one (radial) direction, at any radial location, intensities have to be traced in the 4π spherical space, i.e., in two angular dimensions (polar angle and azimuthal angle). This adds to the complexity of the formulation and computational expense. Thus, researchers are still working on development of methods, in which not only the formulation is simple, but the computational cost is also low.

Proposed by [Chandrasekhar, 1960], the DOM is one of the oldest numerical radiative transfer methods. It has been widely used by physicists and engineers [Modest 2013]. Subsequently, many others have contributed to the development and applications of the DOM [Fiveland 1984, 1987, Kim and Huh, 1999, Lee and Viskanta, 2006]. The DOM proposed by Chandrasekhar for stellar applications and then extended to thermal problems by Fiveland and others [Kim and Huh, 1999] is based on predefined ordinates and weights. Severe ray effects and false scattering have been its drawbacks [Chai *et al.* 1993]. To overcome the shortcomings of the DOM, in 90s, FVM was proposed by Raithby and coauthors and Chai and coauthors, and they found the weight for the discrete directions by integrating the direction cosines over the elemental solid angle. Since then, owing to the flexibility in formulation and solution, the FVM has been extensively used by many researchers.

Mishra *et al.* [2006] revisited the DOM and the FVM. The DOM and the FVM differed only in the angular discretization procedure, and thus in the computations of heat flux and incident radiation. Spatial integration and marching procedures were the same. Mishra *et al.* [2006], relaxed the constraints on selection of ordinates and simplified the computation of the associated weights in the DOM. Though the proposed DOM, called the MDOM, has been successfully tested for a wide range of problems in different geometry, with collimated radiation, it has been used only in 1-D planar geometry. In the analysis of radiation, cylindrical geometry poses lots of complexities. The present work, therefore, aims at the usage of the DOM [Mishra *et al.* 2006] to analyze transport of collimated radiation in a cylindrical participating medium.

The formulation of the MDOM for transport of collimated radiation in a 2-D axisymmetric cylindrical geometry is provided in chapter 2. Towards validation, results on effects of radiative parameters like the extinction coefficient, the scattering albedo and the geometric parameter, the aspect ratio on heat flux and incident radiation distributions on different boundaries of the medium are provided and physically analyzed in the section on results and discussion.

Consideration is given to a 2-D axisymmetric cylindrical enclosure (Fig. 3.1a) having radius R and height Z. The cylinder with diffuse-gray boundaries contains an absorbing, emitting and scattering non-isothermal medium. The top boundary of the medium is subjected to collimated radiation (Fig. 3.1a) having intensity $I_{c,\max}$, and is thus, the source of the collimated radiation in the medium. Along its direction of incidence, while travelling from the top $(z = Z)$ boundary towards the bottom $(z = 0)$ boundary, at any location s, attenuation of the collimated intensity I_c is given by [Mishra *et al.* 2006, 2008]

$$\frac{\partial I_c}{\partial s} = -\beta I_c \tag{3.1}$$

where β is the extinction coefficient.

The attenuated component of the collimated intensity manifests in the form of diffuse intensity I_d, which unlike the collimated intensity I_c, spreads in all directions in the 4π spherical space. Therefore, within the medium, intensity I consists of both collimated I_c and diffuse I_d intensities, i.e.

$$I = I_c + I_d \tag{3.2}$$

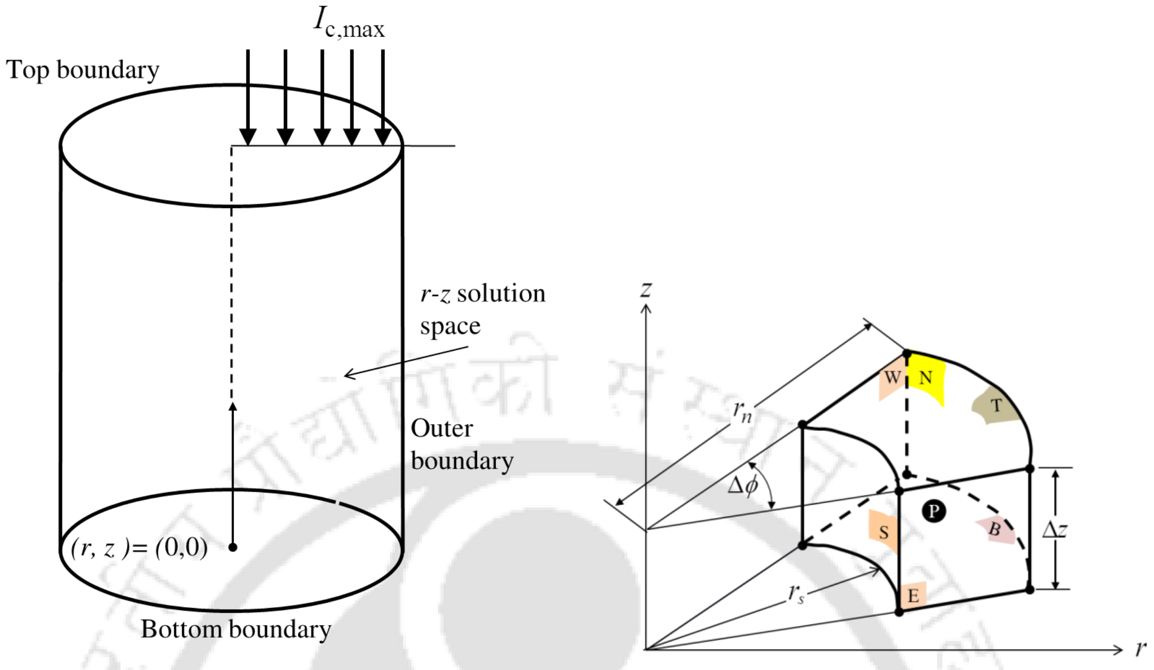

(a) (b)

Figure 3.1: Schematic of (a) 2-D concentric cylindrical enclosure with cylindrical coordinate system and computational domain and (b) 3-D control volume needed for marching in angular space.

With reference to the coordinate system also shown in Fig. 3.1a, with $\theta\left(0\le\theta\le\pi\right)$ as the polar angle and $\phi\left(0\le\phi\le2\pi\right)$ as the azimuthal angle, for any discrete direction $\hat{s}=\left(\sin\theta\cos\phi\right)\vec{e}_r+\left(\sin\theta\sin\phi\right)\vec{e}_\phi+\left(\cos\theta\right)\vec{e}_z$, the RTE is given by

$$\frac{\partial I}{\partial s}=-\beta I+\kappa_a I_b+\frac{\sigma_s}{4\pi}\int_{\Omega'=4\pi} I(s')H\left(s,s'\right)d\Omega' \tag{3.3}$$

where s is the distance in the direction $\hat{s}$, κ_a is the absorption coefficient, σ_s is the scattering coefficient and $H\left(s,s'\right)$ is the scattering phase function. Equation 3.3 is solved using MDOM formulation as discussed in chapter 2. Study on pure radiative transfer is required because of its necessity in modelling laser irradiation on biological tissues in the subsequent chapters.

3.2 Results and Discussion

3.2.1 Validation

In the following section, distributions of non-dimensional heat flux Ψ are analyzed at the bottom, the top and the outer boundaries. Distributions of the non-dimensional incident radiation G^* are studied along the central axis, the bottom and the top boundaries. For distributions of Ψ and G^*, radial and axial distances are normalized as $r^* = \frac{r}{R}$ and $z^* = \frac{z}{Z}$, respectively. Effects of aspect ratio $AR = \frac{2R}{Z}$, extinction coefficient β and scattering albedo ω are studied on the distributions of heat flux Ψ and incident radiation G^*. For all results, incidence of the collimated radiation $I_{\mathrm{c,max}}$ is normal to the top boundary, and boundaries are considered non-reflecting.

Calculation of heat flux (Eq. 2.53) and incident radiation (Eq. 2.55) at any location in the solution (r,z) space needs knowledge of angular distribution of intensity over the 4π spherical space. Intensity distribution is calculated from Eqs. (2.46a-d), and in any direction, through its source term $S_P^m \left(= S_{d,P}^m + S_{c,P}^m\right)$, intensity $I_{d,P}^m$ is an implicit function of intensities $I_{c,P}^m$ and $I_{d,P}^m$. This make the solution an iterative one. In the first iteration, the solution starts with a guess value of the source term, and with radiative boundary conditions known, intensity distribution is calculated at all locations. With new intensity distribution, the source term is updated for all locations and directions. The process continues till convergence. For all locations, in the present case, this stopping criterion has been imposed on the relative change in the incident radiation between two consecutive iterations $\frac{\left|G_{\mathrm{old}}^* - G_{\mathrm{new}}^*\right|}{G_{\mathrm{new}}^*} \le 10^{-8}$.

Before we present and analyze distributions of heat flux and incident radiation for different parameters, grid and ray independencies are established first. With $AR = 1.0$, $\beta = 1.0$ $\omega = 1.0$ and for $N_\theta \times N_\varphi = 12 \times 12$ rays, for different numbers $\left(N_r \times N_z\right)$ of control volumes, radial r^* distributions of heat flux Ψ at the top and the bottom boundaries are shown in Figs. 2a and 2b, respectively.

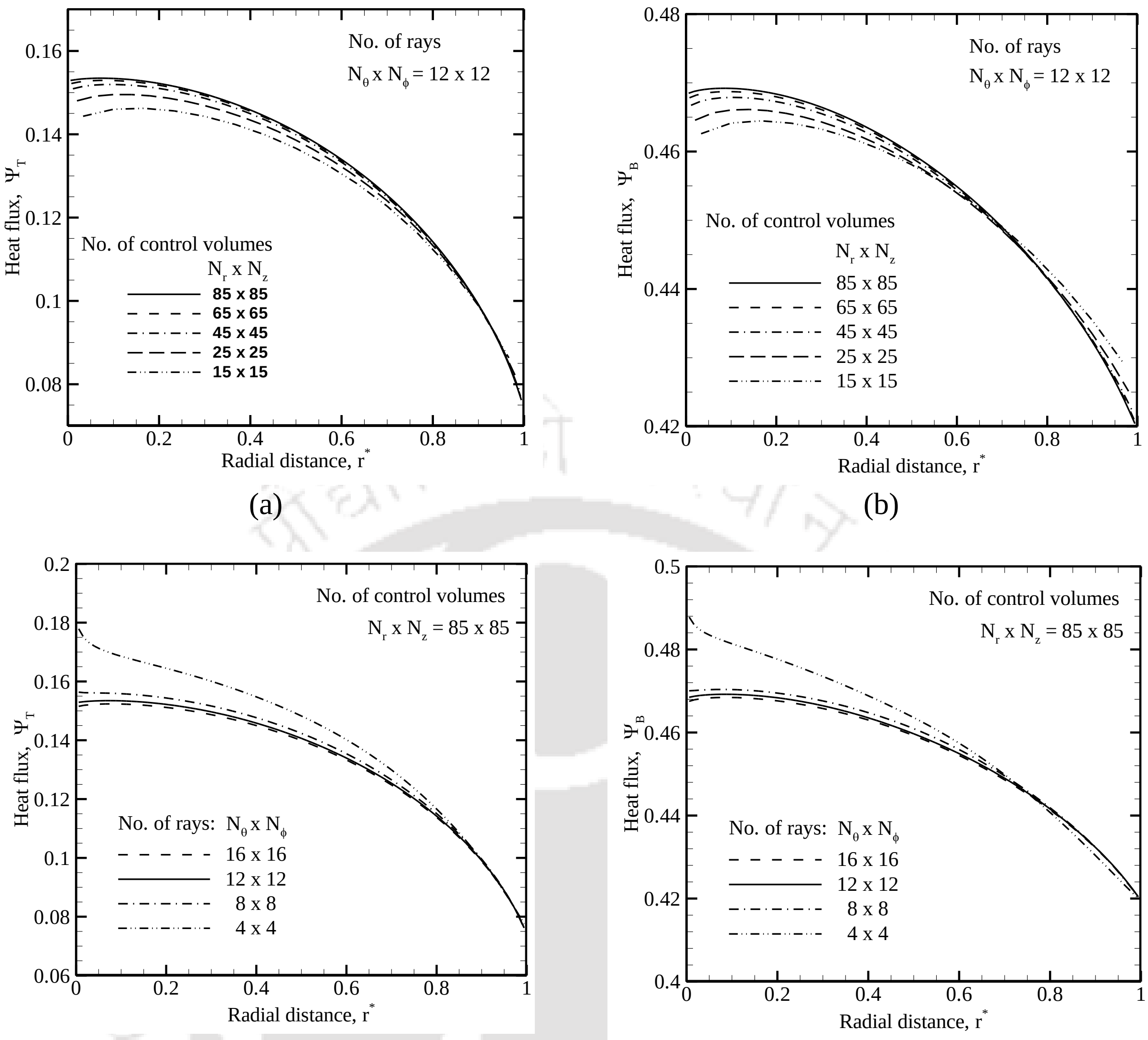

(a) (b)

(c) (d)

Figure 3.2: Effect of number of control volumes on variations of heat flux along (a) the top boundary and (b) the bottom boundary for number of rays $N_\theta \times N_\phi = 12\times12;$ effect of number of rays on variations of heat flux along (a) the top boundary and (b) the bottom boundary for number of control volumes $N_r \times N_z = 85\times85; AR = 1.0, \omega = 1.0, \beta = 1.0.$

No significant change in the results is observed above $N_r \times N_z = 65\times65,$ hence to ensure grid independencies for other sets of parameters, all results are generated for $N_r \times N_z = 85\times85.$ With all other parameters the same, for $N_r \times N_z = 85\times85,$ results of ray independency test are shown in Figs. 3.2c and 3.2d. Radial r^* distributions of heat flux Ψ at the top and the bottom boundaries have no significant improvements beyond $N_\theta \times N_\varphi = 12\times12$ rays, and for all the calculations the number of rays has been fixed to $N_\theta \times N_\varphi = 12\times12.$

3.2.2 Effect of aspect ratio

For different aspect ratios $AR\left(=2R/Z\right)$, with extinction coefficient $\beta=1.0$, scattering albedo $\omega=1.0$, heat flux distributions on the bottom $\left(r^*,0\right)$, the top $\left(r^*,1\right)$, and the outer $\left(1,z^*\right)$ boundaries are shown in Figs. 3.3a-c, respectively. It is observed from Figs. 3.3a and 3.3b that at both bottom and the top boundaries, at any radial location, with increase in AR, heat flux Ψ increases. Axial $\left(1,z^*\right)$ heat flux distribution Ψ_O along the outer boundary also increases with increase in AR.

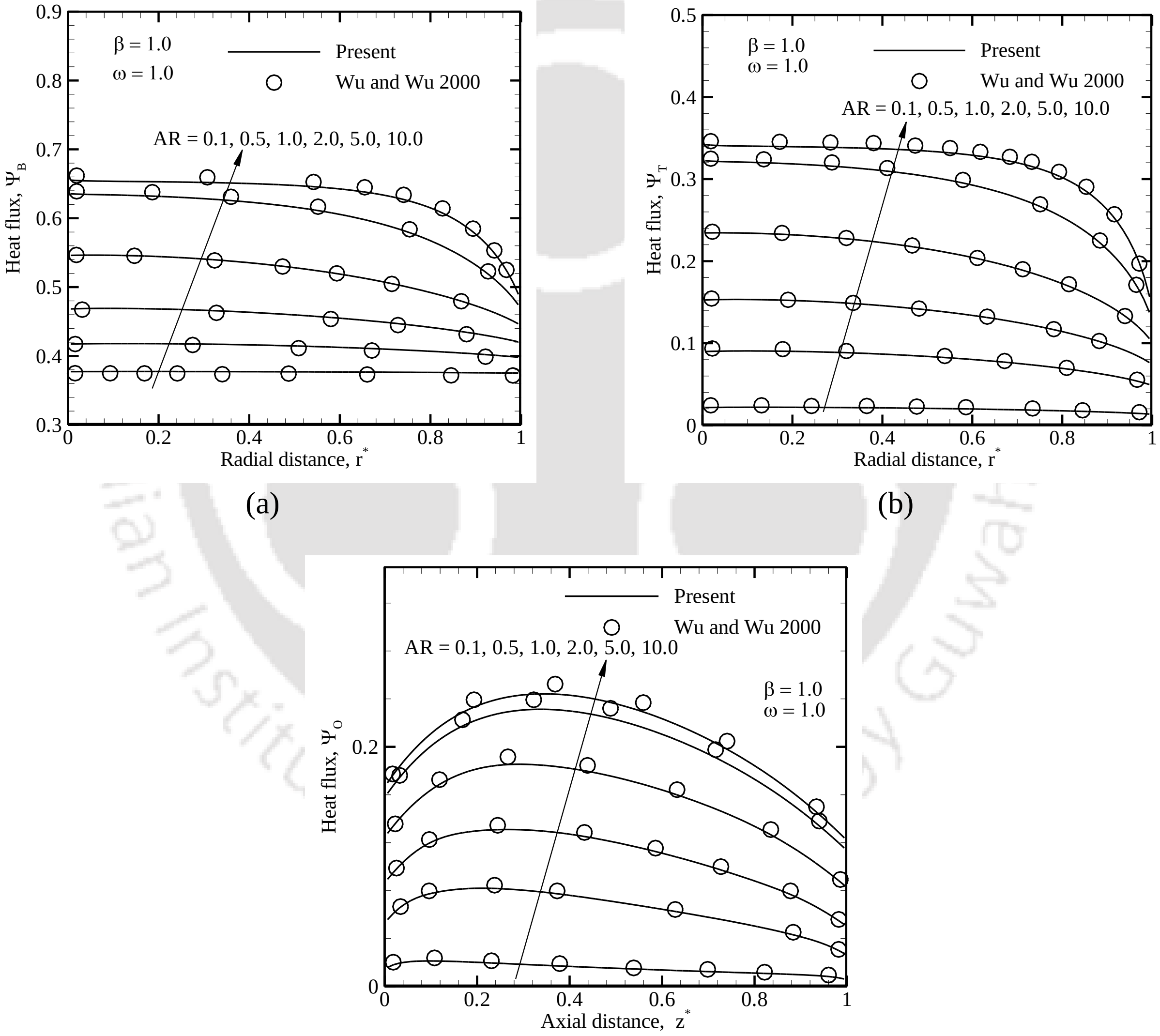

(a) (b)

(c)

Figure 3.3: Effect of aspect ratio AR on variations of non-dimensional heat flux Ψ along (a) the bottom $\left(r^*,0\right)$ boundary, (b) the top $\left(r^*,1\right)$ boundary and (c) the outer $\left(1,z^*\right)$ boundary; $\omega=1.0, \beta=1.0$.

For any AR, at the bottom and the top boundaries, heat flux is maximum at the center $\left(r^* = 0\right)$ and it decreases with increase in radial distance (Figs. 3.3a, 3.3b). Towards the outer boundary, this decrease is steeper for a higher value of AR. Axial variation of Ψ_O on the outer boundary first increase for some distance from the top $\left(z^* = 1\right)$ and after reaching the peak, it decreases further and reaches the minimum at the bottom end $\left(z^* = 0\right)$. With increase in AR, the peak of Ψ_O shifts away from the top boundary.

The observed trend of increase in heat flux with increase in AR at the bottom (Fig. 3.3a) and the top (Fig. 3.3b) boundaries is attributed to the fact that with length Z of the cylinder fixed, for a higher value of AR, the cylinder behaves as a planar geometry. Because of this, compared to the outer boundary, more radiation is received by the bottom and the top boundaries. For a given AR, the maximum heat flux at the center $\left(r^* = 0\right)$ and the minimum at the outer boundary $\left(r^* = 1\right)$ (Figs. 3.3a, 3.3b) is for the fact though the collimated radiation is radially uniformly distributed, however, the diffuse radiation is more concentrated in the central region. Away from the center, its concentration decreases, and it reaches the minimum at the outer boundary.

The observed trend in Fig. 3.3c can be understood from the following. Collimated radiation from the top boundary is the source of radiation in the medium. With its normal incidence (Fig. 3.1a), unlike bottom boundary, the heat flux at the outer boundary is only due to the diffuse radiation. Heat flux due to collimated radiation at the outer boundary will be zero. As the collimated radiation travels towards the bottom boundary, it continuously attenuates, i.e., it becomes weaker. Its attenuation gives rise to the diffuse radiation that goes in all directions. At the outer boundary, while coming from the top to the bottom, owing to stronger collimated radiation, the diffuse radiation is also stronger near the top boundary. With an increase in AR, the location of the maximum heat flux slightly shifts towards the bottom boundary. In all cases, present results of the MDOM are compared with the integral equation approach [Wu and Wu 2000]. MDOM results are found to compare exceedingly well.

Since the present problem belongs to the class of radiative equilibrium, through Eq. (3.24), knowledge of distribution of the incident radiation gives direct estimate of the emissive power, hence temperature of the medium. In Figs. 3.4a-c distributions of non-dimensional incident radiation (Eq. (3.25)) along the central axis $\left(0, z^*\right)$, the bottom boundary $\left(r^*, 0\right)$ and the top boundary $\left(r^*, 1\right)$ are shown, respectively. Like the distributions of heat flux (Figs. 3.3a-c), for $\beta = 1.0$ and $\omega = 1.0$, distributions of $G_C^*\left(0, z^*\right)$, $G_B^*\left(r^*, 0\right)$ and $G_T^*\left(r^*, 1\right)$ are shown for different values of aspect ratio $AR\left(= 0.1, 0.5, 1.0, 2.0, 5.0, 10\right)$. Distributions of $G_C^*\left(0, z^*\right)$ are compared against the results available in [Wu and Wu 2000]. An excellent comparison is found.

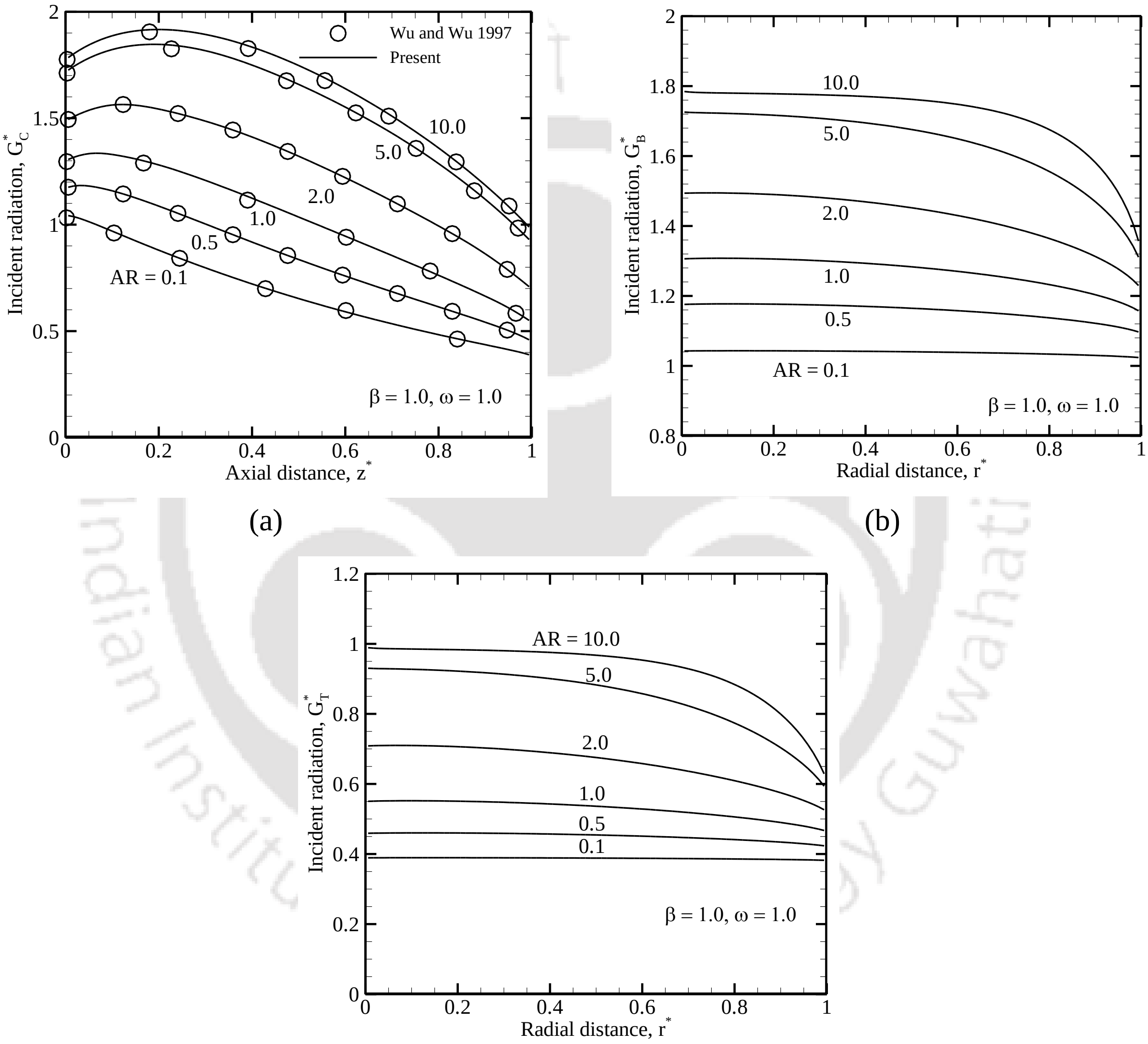

(a)

(b)

(c)

Figure 3.4: Effect of aspect ratio AR on variations of non-dimensional incident radiation G^* (a) along (a) the central $\left(0, z^*\right)$ axis, (b) the bottom $\left(r^*, 0\right)$ boundary and (c) the top $\left(r^*, 1\right)$ boundary; $\beta = 1.0, \omega = 1.0$.

It is observed from Fig. 4a that at any location along the central axis $\left(0, z^*\right)$, the G_C^* increases with increase in *AR*, and like the distribution of heat flux along the outer boundary (Fig. 3.3c), for any *AR*, it first increases with increase in z^*, reaches the maximum and then continuously decreases to a minimum value at the bottom boundary. The value of G_C^* at the top wall is more than at the bottom wall, and with an increase in AR, like heat flux distribution at the outer boundary (Fig. 3.3c), the maximum of the G_C^* slightly shifts away from the top boundary. The radial distributions of incident radiation at the bottom (Fig. 3.4b) and the top (Fig. 3.4c) also follows the similar trend as Ψ_B (Fig. 3.3a) and Ψ_T (Fig. 3.3b).

3.2.3 Effect of extinction coefficient

Extinction coefficient β accounts for attenuation of radiative energy by absorption and out-scattering. For a transparent medium, the extinction coefficient $\beta = 0.0$, whereas, a higher value of β implies an optically dense participating medium having strong ability to attenuate the radiation. Thus, in the analysis of transport of thermal radiation, extinction coefficient β is an important optical parameter. Effects of β on distributions of heat flux and incident radiation are shown in Figs. 3.5 and 3.6, respectively. These results are shown for *AR* = 1.0 and the scattering albedo ω = 1.0. In Figs. 5a-c, for β = 0.5, 1.0, 2.0, 4.0 and 10.0, distributions of heat flux are shown on the bottom boundary, the top boundary and the outer boundary, respectively. It is observed from Fig. 3.5a that at any location on the bottom $\left(r^*, 0\right)$ boundary, heat flux decreases with increase in β. For a higher value of β, as collimated and diffuse radiations move along the bottom boundary, attenuation experienced by them is more, and this results in lower heat flux. For a given β, the heat flux is the maximum at the center $(0,1)$ and it gradually decreases to the minimum at the outer edge $(1,1)$ of the boundary.

For different values of β, distributions of heat flux at the top boundary are shown in Fig. 3.5b. Contrary to the heat flux distributions on the bottom boundary, with increase in β, heat flux is found to increase. This trend is attributed to the fact that with boundaries of the enclosure black, the top boundary does not receive collimated radiation. Thus the heat flux at this boundary is only due to the diffuse radiation. With increase in β, attenuation of the collimated radiation is more, and thereby a higher amount of diffuse radiation manifests. Thus, for a higher $\beta,$ the top boundary receives more diffuse radiation, and hence is the observed trend. For a given $\beta,$ the heat flux is the maximum at the center $(0,1)$ and minimum at the outer edge $(1,1)$ of the boundary. With increase in $\beta,$ the difference between the maximum and the minimum increases. With homogeneous incidence of collimated radiation at the top boundary, the central region of the cylinder receives more diffuse radiation than the outer boundary.

Heat flux distributions at the outer boundary are shown in Fig. 3.5c. For any $\beta,$ with increase in axial distance $z^*,$ heat flux first increases, it reaches the maximum and then continuously decreases towards the bottom end. The peak values are higher for higher $\beta.$ Further, with increase in $\beta,$ the peak of the heat flux distribution curve shifts towards the top boundary, and the rise and the fall of the heat flux are sharper. The reason for above trend is attributed to the fact that concentration of diffuse radiation is more in the vicinity of the top boundary, and this concentration increases with increase in $\beta.$ For a given axial distance, attenuation of collimated radiation is more for higher $\beta.$ For $\beta = 1.0,$ heat flux distributions at all three boundaries are compared against the results available in the literature [Wu and Wu 2000]. A very good agreement is observed.

Effects of extinction coefficient β on variations of the incident radiation along the central axis $(0,z^*),$ the bottom boundary $(r^*,0)$ and the top boundary $(r^*,1)$ are shown in Figs. 3.6a-c, respectively. For a higher $\beta,$ along the central axis, the incident radiation G_C^* is higher towards the top boundary and lower towards the bottom boundary. The difference between the maximum and the minimum increases with increase in $\beta.$ For all values of $\beta,$ the DOM results are found to compare exceedingly well with the results of [Wu and Wu 1997]. For different values of $\beta,$ radial distributions of incident radiation at the bottom boundary (Fig. 3.6b) and the top boundary (Fig. 3.6c) follow a trend similar to that of heat flux distributions (Figs. 3.5a and 3.5b) at these boundaries.

3.2.4 Effect of scattering albedo

In an absorbing, emitting and scattering medium, with κ_a as the absorption coefficient and σ_s as the scattering coefficient, the extent of scattering is known by the scattering albedo

$\omega = \dfrac{\sigma_s}{\kappa_a + \sigma_s} = \dfrac{\sigma_s}{\beta}$. Medium is absorbing-emitting for $\omega = 0$, and it scatters all radiation when $\omega = 1.0$. Like β, the scattering albedo ω is also an important parameter.

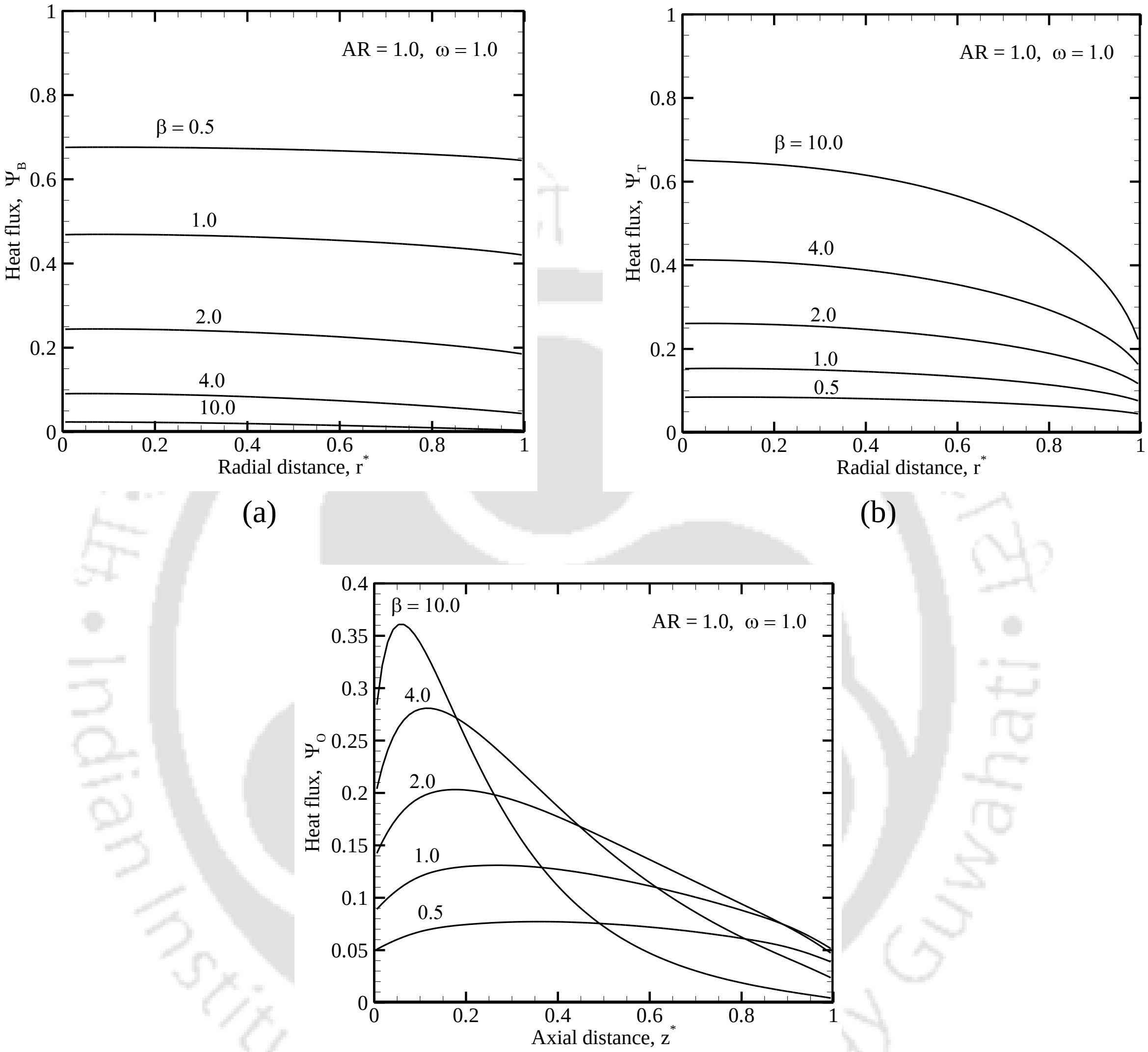

(a) (b)

(c)

Figure 3.5: Effect extinction coefficient β on variations of non-dimensional heat flux Ψ along (a) the bottom $(r^*, 0)$ boundary (b) the top $(r^*, 1)$ boundary and (c) the outer $(1, z^*)$ boundary; $AR = 1.0, \omega = 1.0$.

Its effects on distributions of heat flux and incident radiation are shown in Figs. 3.7 and 3.8, respectively. These results are shown for $AR = 1.0$ and $\beta = 1.0$. At all three boundaries, heat flux increases with increase in ω, and for a given ω, at the bottom and the top boundaries, it is the maximum at the center and the minimum at the outer edge. At the outer boundary of the cylinder, heat flux first increases, reaches its maximum value and then decreases to the minimum at the bottom end. At all boundaries, variations in the maximum and the minimum values increases with increase in ω. With extinction coefficient β fixed, with increase in ω, the absorption decreases and scattering is enhanced. This is evident from Eq. (3.7) in which the first term on the right-hand-side with multiplier $\kappa_a = (1-\omega)\beta$ accounts for absorption and the second terms $\sigma_s = \omega \times \beta$ is the incident radiation because of in-scattering.

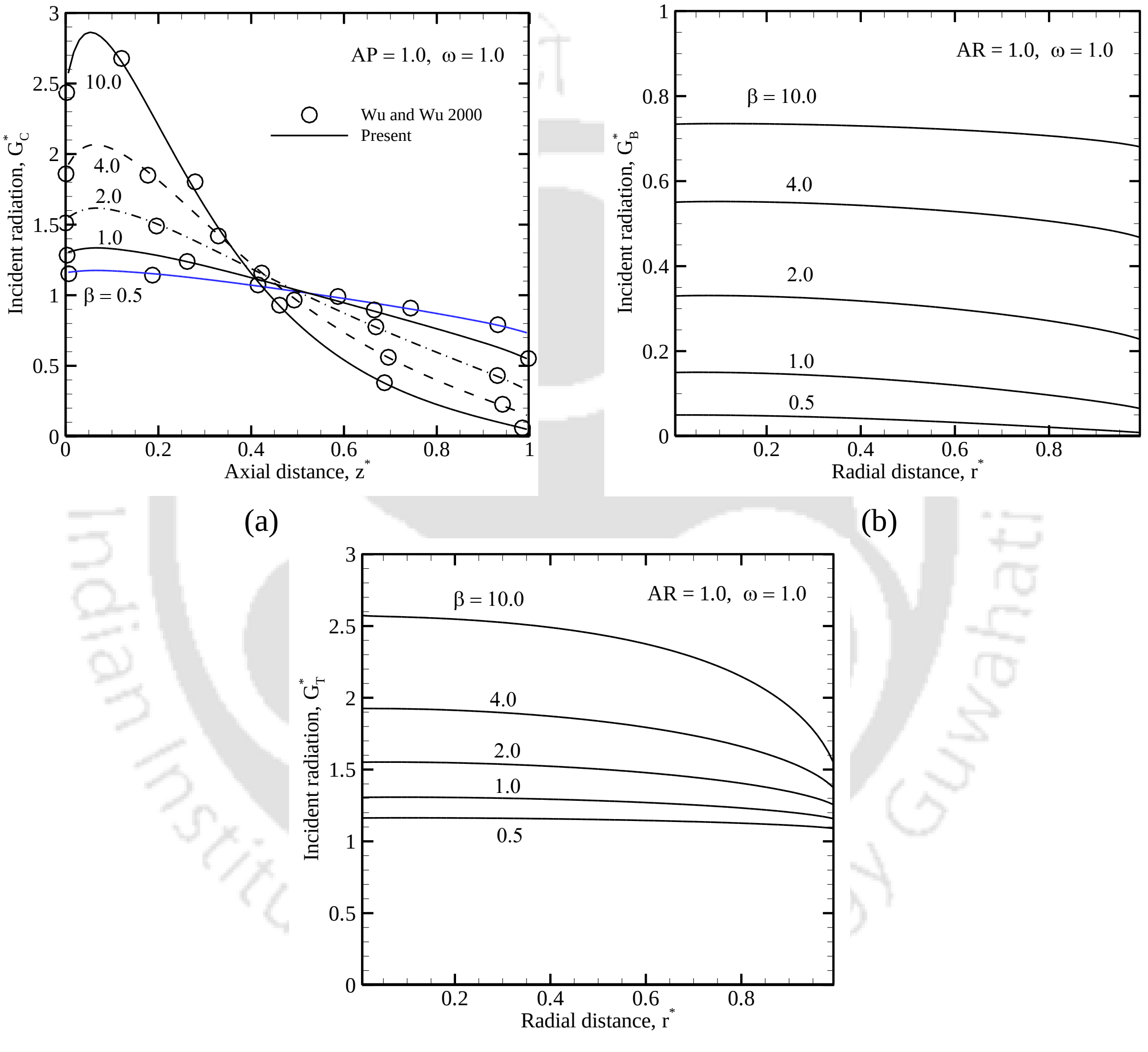

(a) (b)

(c)

Figure 3.6: Effect extinction coefficient β on variations of non-dimensional incident radiation G^* along (a) the central $(0, z^*)$ axis (b) the bottom $(r^*, 0)$ boundary and (c) the top $(r^*, 1)$ boundary; $AR = 1.0, \omega = 1.0$.

With increase in ω, which may be because of increased in-scattering or decreased absorption, thus leads to a higher value of the heat flux. At all three boundaries, for $\omega = 1.0$, DOM results are compared with [Wu and Wu 2000]. A good comparison is found. For different values of ω, distributions of incident radiation along central axis $\left(0, z^*\right)$, and on bottom $\left(r^*, 0\right)$ and top $\left(r^*, 1\right)$ boundaries are shown in Figs. 3.8a-c, respectively.

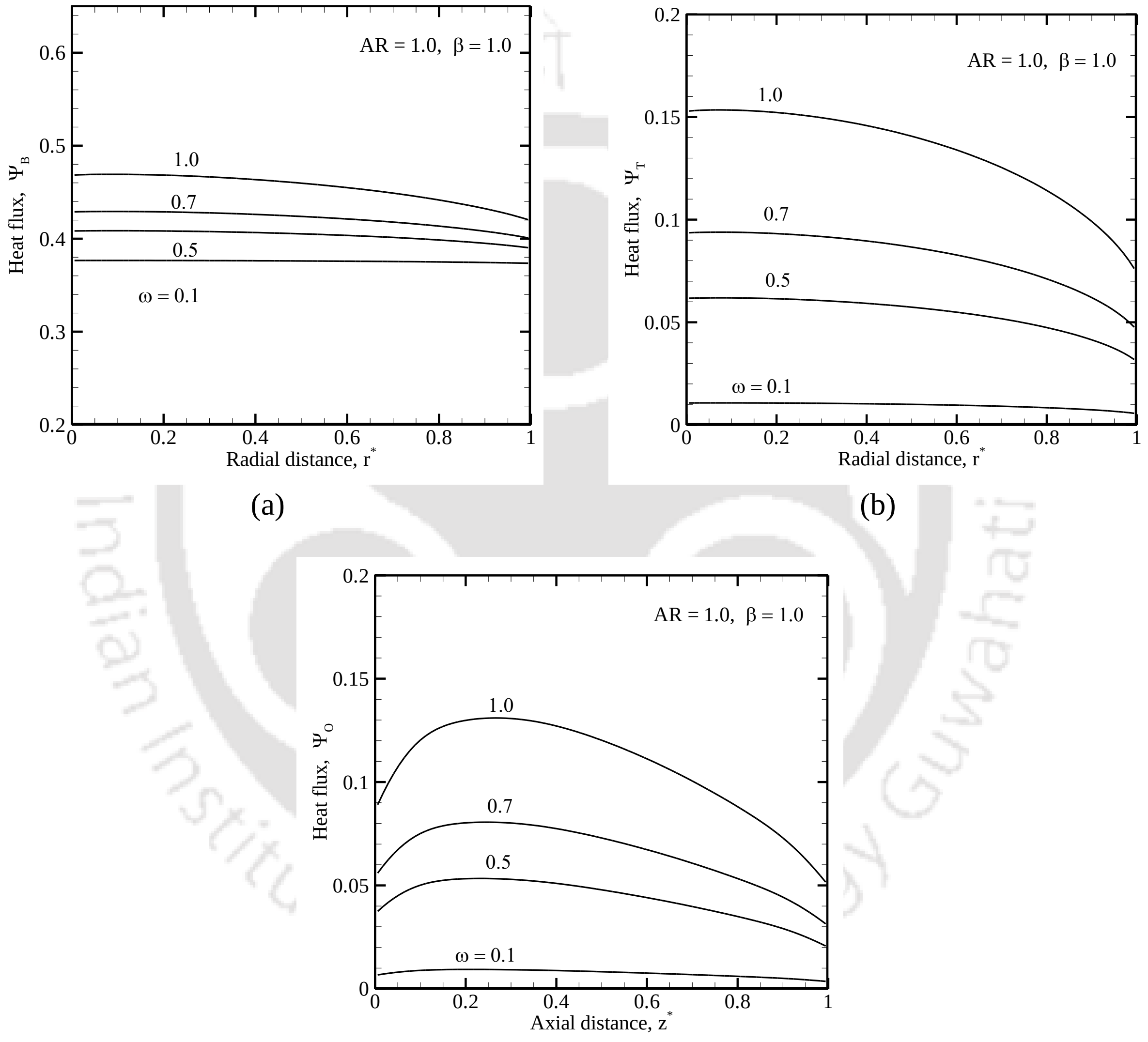

(a) (b)

(c)

Figure 3.7: Effect of scattering albedo ω on variations of non-dimensional heat flux Ψ along (a) the bottom $\left(r^*, 0\right)$ boundary, (b) the top $\left(r^*, 1\right)$ boundary and (c) the outer $\left(1, z^*\right)$ boundary; $AR = 1.0, \omega = 1.0$.

Along the central axis, the incident radiation decreases sharply towards the bottom boundary, and at the bottom and the top boundaries, the decrease is slow with the radial distance. Along the central axis, for $\omega = 0.5$ and 1.0, the MDOM results are compared with those available in the literature. MDOM results compare exceedingly well.

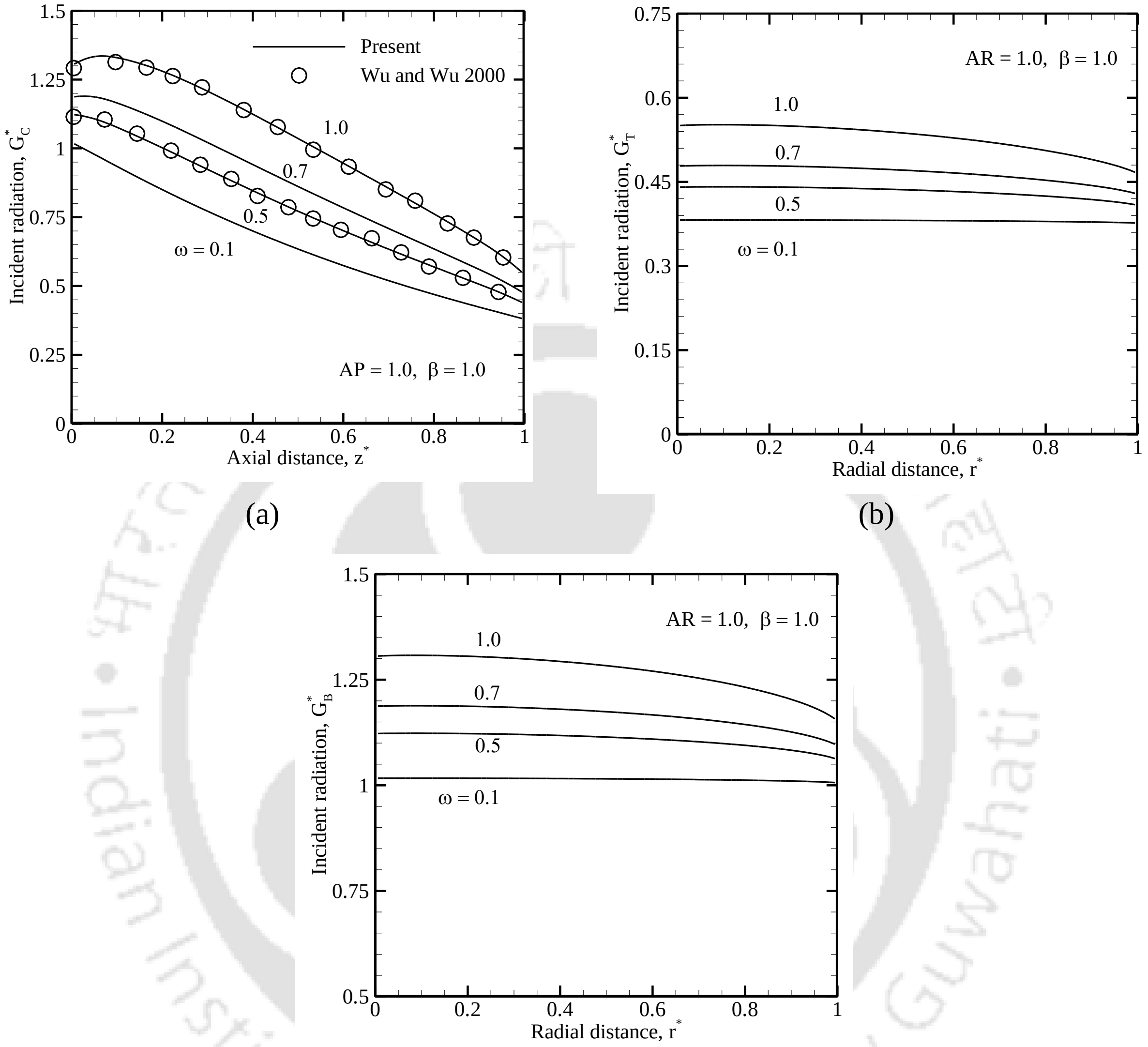

(c)

Figure 3.8: Effect of scattering albedo ω on variation of non-dimensional incident radiation G^* along (a) the central $\left(0, z^*\right)$ axis, (b) the bottom $\left(r^*,0\right)$ boundary and (c) the top $\left(r^*,1\right)$ boundary; $AR = 1.0, \beta = 1.0$.

3.3 Closure

Usage of the MDOM was extended to the analysis of radiative heat transfer in a 2-D cylindrical enclosure subjected to collimated radiation. Effects of the aspect ratio, the extinction coefficient and the scattering albedo on variations of heat flux along the bottom, the top and the outer boundaries were analyzed. Effects of these parameters were also analyzed on the variations of incident radiation along the central axis, the bottom boundary and the top boundary. MDOM results were compared with those available in literature. Results were found to compare exceedingly well.

Chapter 4

Convective and Contact Surface Cooling During Laser Induced Thermal Therapy

4.1 Theory

The present chapter deals with different aspects of surface cooling during laser induced hyperthermia and thermal therapy. Divided broadly into two categories of surface cooling mechanisms, this chapter is presented into two sections. First section (4.2) deals with the convective non-contact surface cooling and second section (4.3) deals with optical window based contact surface cooling during laser induced thermal therapy. In section 4.3, starting with blood perfused tissue based on Pennes bioheat model, present study is extended towards a more realistic vascularized multilayer tissue geometry based on both Pennes and Weinbaum-Jiji models. Before presenting the case specific formulation and results, in the following paragraphs a brief theoretical discussion is presented.

Laser displays three important characteristics. It is (i) coherent, i.e. all the wave trains are exactly in phase, in time as well as in space, (ii) collimated, i.e. the radiation beam is almost parallel (showing a low divergence), and (iii) monochromatic, i.e. a narrow spectral band of high spectral intensity is emitted. For therapeutic applications, the laser-tissue interaction mechanisms are mainly determined by two parameters, namely the laser exposure time on the tissue and the effective power density taking into account the tissue-specific absorption. The absorption and scattering of any tissue varies with wavelength. The spectrum of commercially available lasers for diagnostic and therapeutic medical applications stretches from 193 nm to 10.6 μm. Both *cw* and pulse lasers are available in the ultra violet (UV), visible and infra-red (IR) [Welch 1984, Welch 2011, Zhou 2004, Kim 2004, Niemz 2007].

Study of Laser-tissue interaction can be divided into two broad areas based on change and effects on properties of tissue when tissue is irradiated by laser. There are two primary effects of laser irradiation of biological tissues, thermal and optical. The thermal effects are affected by both thermo-physical properties as well as optical properties of tissue. The process of laser irradiation of tissue and its subsequent effects are summarized as [Dua and Chakraborty 2005, Jha and Narasimhan 2011].

Tissue is treated as an absorbing and scattering medium. When irradiated with a laser beam, changes in its optical properties can be measured which helps in determining the state of the tissue. For the measurement of following properties several methods are available [Cheong *et al.* 1990]:

i. Light propagation
ii. Reflection
iii. Transmission

When a tissue is irradiated most of the absorbed light is converted into heat. For the measurement of following properties several methods are available:

i. Temperature
ii. Thermo-physical and optical properties
iii. Extent of thermal damage

The basis of hyperthermia or laser induced thermal therapy (LITT) is the thermal energy or heat generated by laser in the biological medium. Thermal energy converted from laser power in biological tissue kills the target tissue if the temperature reaches the degeneration temperature, i.e. 42.5°C to 43°C or higher. However, the chances of tissue damage in surrounding area is also high if temperature distribution is not controlled precisely [Sakurai 2010]. Few approaches such as focused beam laser instead of collimated beam laser have been proposed for localized and deep tissue heating [Barun and Ivanov 2003, Dai *et al.* 2008, Deng and Liu 2002, Fanjul-Vélez *et al.* 2009].

The thermal analysis of a biological system is complex due to simultaneous presence of multiple parameters like thermal conductivity, heat transfer coefficient, blood flow rate and metabolic heat generation. Pennes' model [Pennes 1948] is a good approximation for predicting temperature field in a biological system [Arka *et al.* 2009, Welch 2011, Zhou 2004, Sakurai 2010, Kim 2004, Datta 2002, Jiji 2009].

Heat transfer equation and its solution for inanimate system requires the knowledge of material properties, such as density, specific heat and thermal conductivity, and initial and boundary conditions, and is relatively straightforward. While solving the same for the biological system perfused with blood, requires few extra information. The complexity in modeling bioheat equation arises from the fact that living tissue is a complicated system, which is characterized by anisotropic blood flow in a complex network of branching arteries and veins with changing size and orientation. In addition, the thermal state of a tissue is always being maintained by an active thermoregulatory mechanism, which tries to make and keep the tissue at a fixed temperature, known as core body temperature [Jiji 2009, Ng and Chua 2002].

Laser induced hyperthermia and thermal therapy are emerging as promising methods of treatment for many ailments like port-wine stain, and diseases like malignant tumors [Li *et al.* 2013, 2014b, Loze and Wright 2001]. During such procedures, light energy gets absorbed in the tissue, and the absorption starts from the skin surface in case of external laser irradiation. Therefore, the maximum thermal energy produced is in the skin and the tissue layers immediately below the skin surface (dermis and subcutaneous layers). The multilayer skin tissue is composed of epidermis, the outermost layer, the intermediate dermis, and internal vascular tissue with layers of fat. The epidermis contains melanin which is characterized by high absorption of light, and is, therefore, the most susceptible for thermal damage during laser heating of tissues [Bashkatov *et al.* 2005, Lister *et al.* 2012]. In any externally irradiated hyperthermia procedure, principal aim is to provide treatment to target tissue while minimizing thermal damage to the skin surface. Therefore, in any such procedures, which involves high temperatures, cooling the skin is desirable.

One of the major issues in skin surface laser irradiation is the surface overheating and thermal damage of the skin. Forced convective surface cooling is a viable option to mitigate the skin thermal damage. To determine the efficacy of forced convection surface cooling, present study demonstrates numerical simulation for minimizing undesired thermal damage. In the first part of the present study, heating of blood perfused tissue based on Pennes bioheat model during laser irradiation with convective surface cooling is studied.

4.2 Surface Cooling During Laser Induced Thermal Therapy

The major contribution of Pennes was the inclusion of blood perfusion term, which identified the role of blood flow in heat transfer to or from the tissue. The model was based on assumption that thermal equilibrium between the blood and the surrounding occurs mainly in capillaries. An additional assumption made is that the venous temperature is equal to local tissue temperature. The Pennes bioheat equation in general form is given by

$$\rho c\left(\frac{\partial T}{\partial t}\right)=k\left(\nabla^2 T\right)+\rho_b c_b \gamma_b\left(T_a-T\right)+Q_m \tag{4.1}$$

This equation is also known as the bioheat equation. In Eq. 4.1, each term has a unit of $\mathrm{W/m^3}$ and thus represent energy per unit volume per unit time. The bioheat transfer equation is derived from energy conservation equation and heat conduction equation, and additionally including terms for describing blood perfusion and metabolic heat generation. In Eq. 4.1, T is temperature of tissue, ρ and c are density and specific heat of tissue, k is the thermal conductivity of tissue, T_a is the temperature of arterial blood, ρ_b and c_b are blood density and specific heat of blood, and γ_b is the blood perfusion rate. Q_m is the metabolic heat generation rate. The term on left of Eq. 4.1 represents the energy storage i.e. Rate of change of stored energy). First term on right hand side of Eq. 4.1 represents conduction (i.e. Rate of net energy transport due to conduction), second terms accounts for convective effects (i.e. Rate of net energy transport due to bulk flow), and the third term represents metabolic heat generation rate [Datta 2002, Jiji 2009, Welch 2011, Wissler 1998].

Bioheat transfer analysis in laser irradiated tissue has been studied by many researchers [Díaz *et al.* 2001, Zhou and Liu 2004, Jaunich *et al.* 2008]. The importance and applicability of Laser induced thermal therapy (LITT) and detailed discussion of Monte Carlo method used for light transport in biological medium is also presented. However Monte Carlo method is computationally costly [Zhou and Liu 2004, Kim and Guo 2004].

Sakurai *et al.* (2010) solved the coupled radiation and bioheat transfer for continuous wave light transport in biological tissue using radiation element method (REM^2), which is computationally faster than Monte Carlo method. Also they demonstrated the effect of air-tissue interface and effects of optical and thermophysical properties of biological tissue, like varying refractive index, extinction coefficient, scattering albedo, blood perfusion parameter, and conduction-radiation parameter [Sakurai *et al.* 2010].

For radiative heat transfer simulation, the radiation element method by ray emission model REM^2 was used. Biological tissue is scattering and absorbing medium against radiation. Numerical Simulations were done in order to study heat transfer phenomena inside biological tissue when the skin surface is irradiated by the laser. The temperature distribution in the biological tissue on laser irradiation was numerically estimated by the thermal radiation-bioheat conduction combined heat transfer. The wavelength of 1064 nm with assumption of continuous wave Nd:YAG laser irradiation, was considered.

A proposed new surface cooling method by using a cooling device is used in the simulation for prevention of excess temperature rise on skin surface. The cooling device was devised for simultaneous cooling of the surface and laser irradiation.

The intensity I, which may be incident or outgoing, is governed by the radiative transfer equation, which, is given by [Sakurai *et al.* 2010],

$$\left(\frac{1}{c}\right)\frac{\partial I(r,s)}{\partial t}+\frac{dI(r,s)}{ds}=\kappa I_b(r)-\beta I(r,s)+\frac{\sigma_s}{4\pi}\int_{4\pi} I_{-}(s_i)\Phi(s_i,s)\,d\Omega' \tag{4.2}$$

where c is the speed of light, $I(r,s)$ is the radiation intensity at a given location indicated by position vector r, in the direction s, travelling through a participating medium. In steady state, RTE is given as

$$\frac{dI(r,s)}{ds}=\kappa I_b(r)-\beta I(r,s)+\frac{\sigma_s}{4\pi}\int_{4\pi} I_{-}(s_i)\Phi(s_i,s)\,d\Omega' \tag{4.3}$$

The sum of absorption coefficient κ and scattering coefficient σ_S is the extinction coefficient $\beta=\kappa+\sigma_S$ [Mishra *et al.* 2006, Modest 2013, Muthukumaran and Mishra 2008, Sarma *et al.* 2005].

4.2.1 1-D and 2-D axisymmetric cylindrical geometry

To simplify the understanding of heat transfer phenomenon in a biological tissue, consideration is given to one-dimensional single-layer planar biological tissue (Fig. 4.1) of thickness 50 mm. The west boundary (skin surface) is subjected to laser irradiation. Temperature distribution is estimated by solving Pennes bioheat equation (Eq. 4.1) using the FVM. Radiative information needed in the bioheat energy equation is computed using the REM^2. The computational domain is divided into 1002 radiation elements in REM^2, and an equal number of CVs in the FVM.

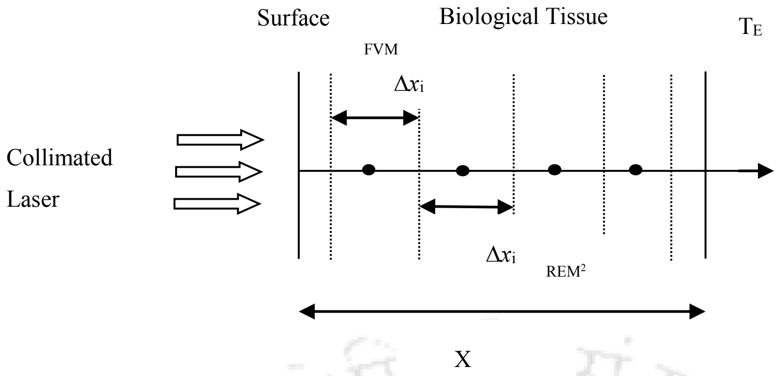

Figure 4.1. The analysis model of biological tissue for radiation- bioheat transfer simulation.

For a 2-Dimensional analysis, a cylindrical model (Fig. 4.2) with radius of 20 mm and height of 25 mm is considered. A 2-D grid of 100×125 for bioheat transfer calculation was considered. The thermal and physical properties of entire media are assumed uniform. The axisymmetric model for radiative heat transfer using REM^2 was verified by [Maruyama *et al.* 2010].

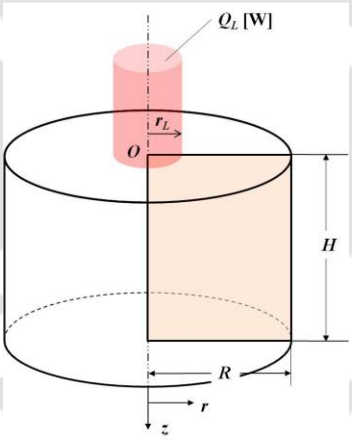

Figure 4.2. Two dimensional axisymmetric cylinder model.

To prevent overheating of the surface and to achieve desired temperature inside the tissue, a surface cooling mechanism is required. In this study, we introduce a cooling device to cool the tissue surface. As shown in Fig.4.3, the cooling device is a rectangular flow path, with flow of water through it. Water exhibits a very weak absorption for light near infrared wavelength 1064 nm. The top surface of the device is quartz glass that transmits a laser on the flow channel, and the lower part is a sapphire glass which is having excellent thermal conductivity. This way simultaneous irradiation of laser and cooling of the surface is possible.

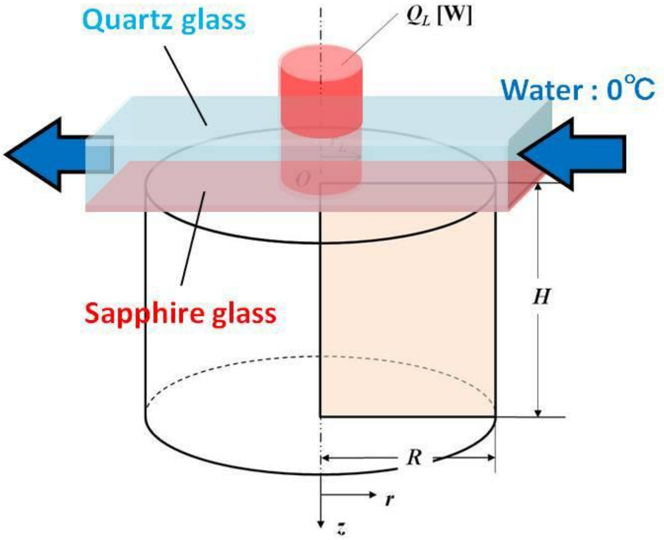

Figure 4.3. The 2-D axisymmetric biological tissue with skin cooling device.

4.2.2 Results and discussion – convective and sapphire device cooling

Absorption coefficient, $\kappa[1/\mathrm{m}]$ and scattering coefficient $\sigma_s[1/\mathrm{m}]$ of skin tissue for 1064 nm wavelength are 16.5 and 17100, respectively. The thermo-physical properties of various tissues from are as shown in Table 4.1 [Okajima 2009, Sakurai 2010]. Temperature distribution in a one-dimensional skin tissue with laser irradiation is obtained for various levels of irradiation time.

Table 4.1: Thermophysical properties of different tissues.

Tissue	Density $\rho[\mathrm{kg/m^3}]$	Specific heat $c[\mathrm{J/(kg\cdot K)}]$	Thermal conductivity $k[\mathrm{W/m\cdot K}]$	Blood perfusion rate $\omega_0[1/\mathrm{s}]$	Metabolic rate $q_0[\mathrm{W/m^3}]$
Skin	1085	3680	0.47	1.8×10^{-3}	1368
Fat	850	2300	0.16	4.2×10^{-4}	2558
Muscle	850	3768	0.42	5.0×10^{-4}	1648
Liver	1060	3600	0.52	1.5×10^{-2}	6100

For values of input laser power 0.5 W/cm^2 and 1.0 W/cm^2 were obtained as shown in Fig. 4.4 (a) and Fig. 4.4(b), respectively. Figures 4.5 (a) and (b) show the temperature distribution when forced convection cooling at the boundary was provided for cases of 0.5W/cm^2 and 1.0W/cm^2 respectively.

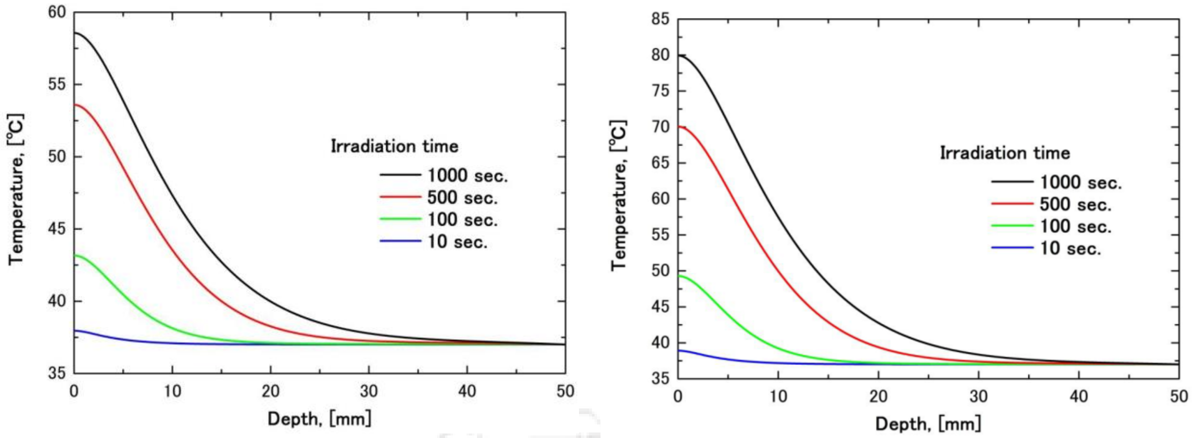

(a) (b)

Figure 4.4. Temperature distribution in biological tissue with YAG laser irradiation for laser power (a) 0.5 W/cm^2 and (b) 1.0 W/cm^2.

Two-dimensional calculation were performed for beam radius of 1mm and laser power of 4W. The temperature distribution along the center line is shown for skin tissue for different irradiation time levels (Fig. 4.6(a)). A 2-D color contour is shown in Fig.4.6 (b).

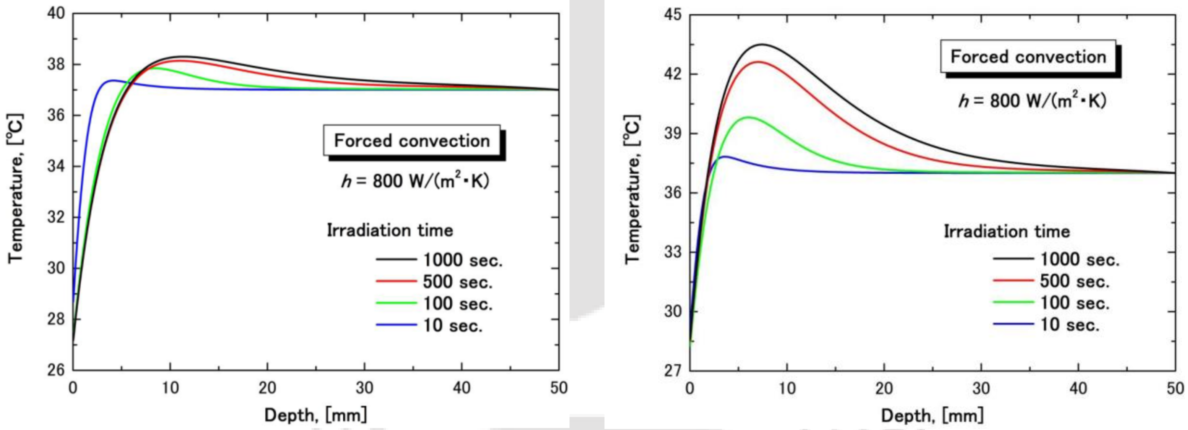

(a) (b)

Figure 4.5. Temperature distribution in biological tissue with YAG laser irradiation and forced convection cooling for (a) laser power 0.5 W/cm^2 and (b) 1.0 W/cm^2 (heat transfer coefficient is $800\,\mathrm{W/m^2\cdot K}$.

Figure 4.7 (a) and (b) show temperature distribution along center and 2-D plane for beam radius of 2 mm with 4 W power. Figure 4.8 (a) and (b) show temperature distribution for a Gaussian beam with 4 W power for skin tissue. As can be seen in figures and plots of direct irradiation of laser on skin surface, the maximum temperature lies on the outermost part of tissue.

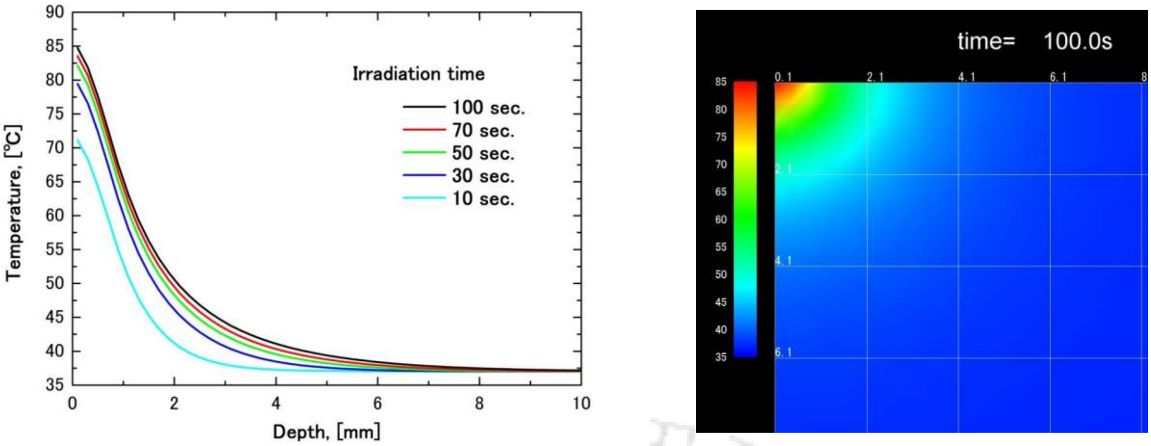

(a) (b)

Figure 4.6. (a)Time variation of temperature distribution at center with beam radius 1 mm and power 4 W (b) 2-D axisymmetric temperature distribution.

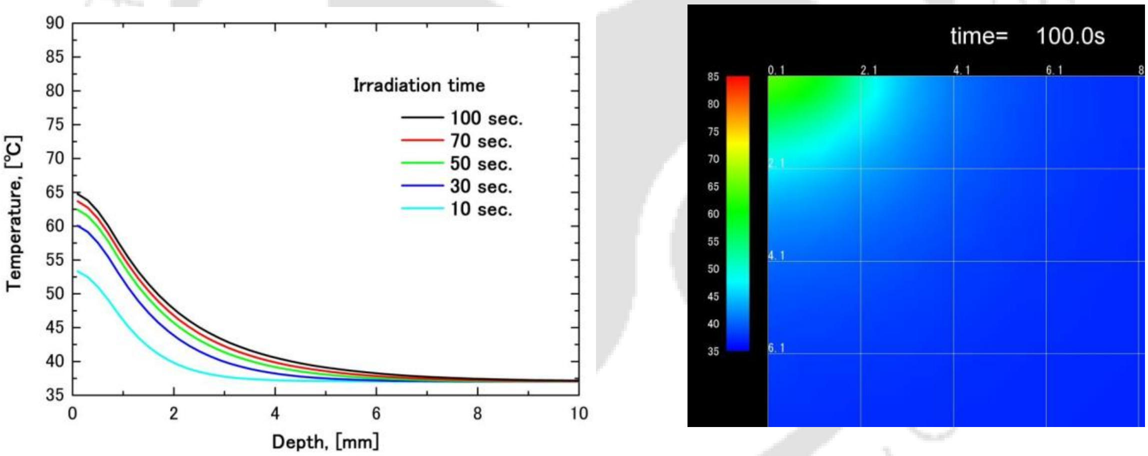

(a) (b)

Figure 4.7. (a)Time variation of temperature distribution at center with beam radius of 2mm and power 4 W (b) 2-D axisymmetric temperature distribution.

With the use of cooling device, as explained earlier, simulation results were obtained for beam radius of 1mm and power of 4W for skin tissue (Fig. 4.9). The heat transfer coefficient used was 200 W/m^2.K. As can be seen in 2-D plot, Fig 4.10., the maximum temperature lies inside the tissue. For 4 W power, temperature suitable for direct ablation was not achieved so simulation with 10 W were performed and the temperature distribution can be seen in Figs. 4.11-4.12.

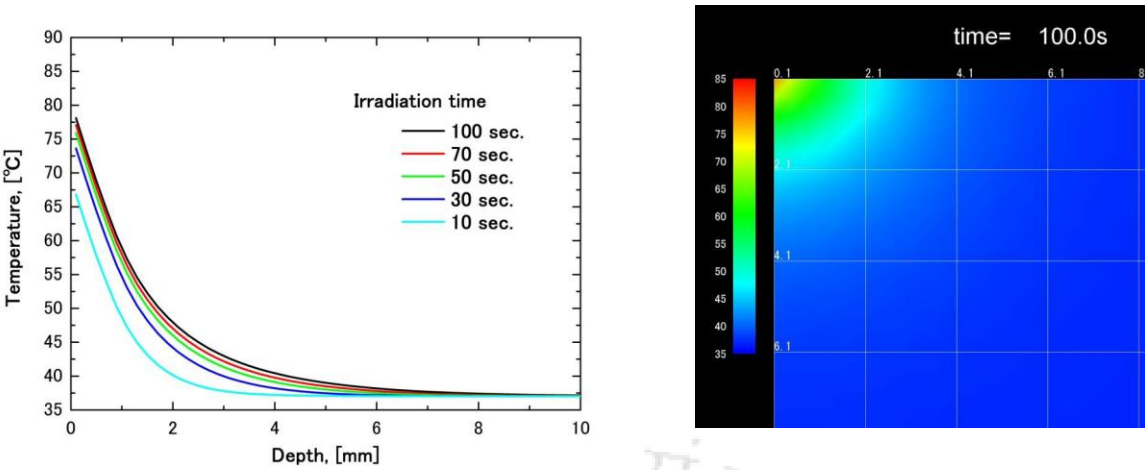

(a) (b)

Figure 4.8. (a)Time variation of temperature distribution at center with Gaussian beam and (b) 2-D axisymmetric temperature distribution.

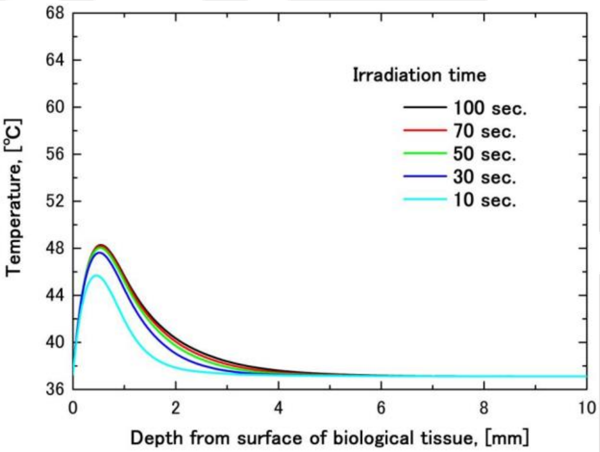

Figure 4.9. Time variation of temperature distribution at center with laser power 4 W.

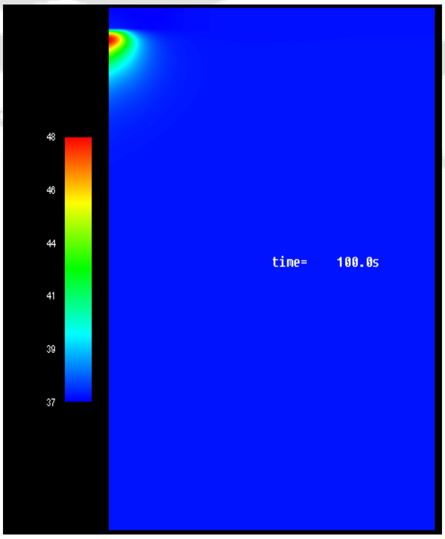

Figure 4.10. Axisymmetric temperature distribution using cooling device with laser power 4 W.

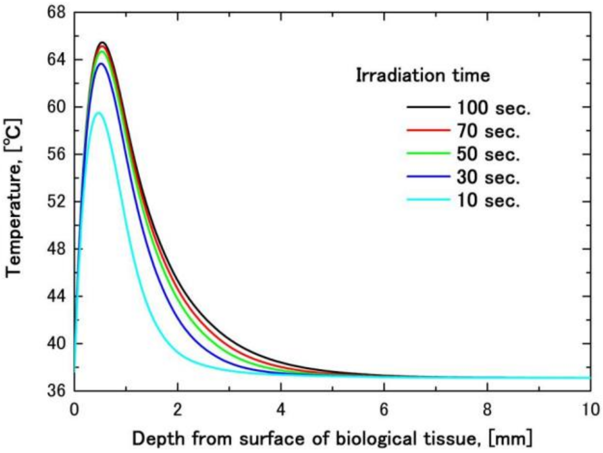

Figure 4.11. Time variation of temperature distribution at center with laser power 10 W.

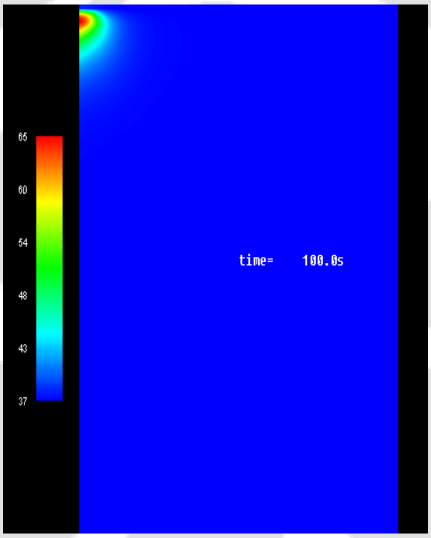

Figure 4.12. Axisymmetric temperature distribution using cooling device with laser power 10 W.

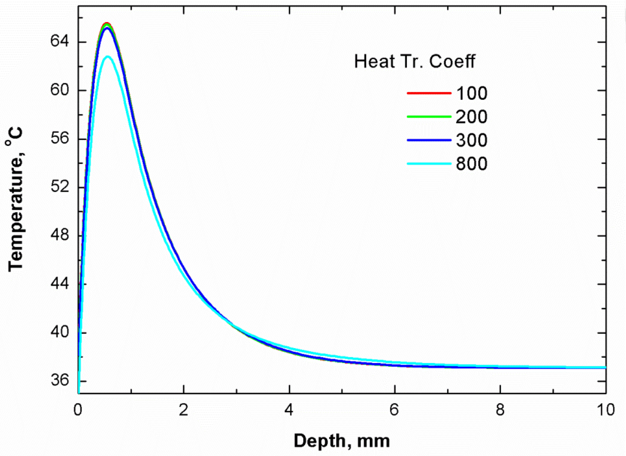

Figure 4.13. Temperature distribution at center for different values of *h* at power of 10 W.

Comparisons of effect of heat transfer coefficient on temperature distribution at centerline (Fig. 4.13) and in 2-D plane (Fig.4.14) were performed.

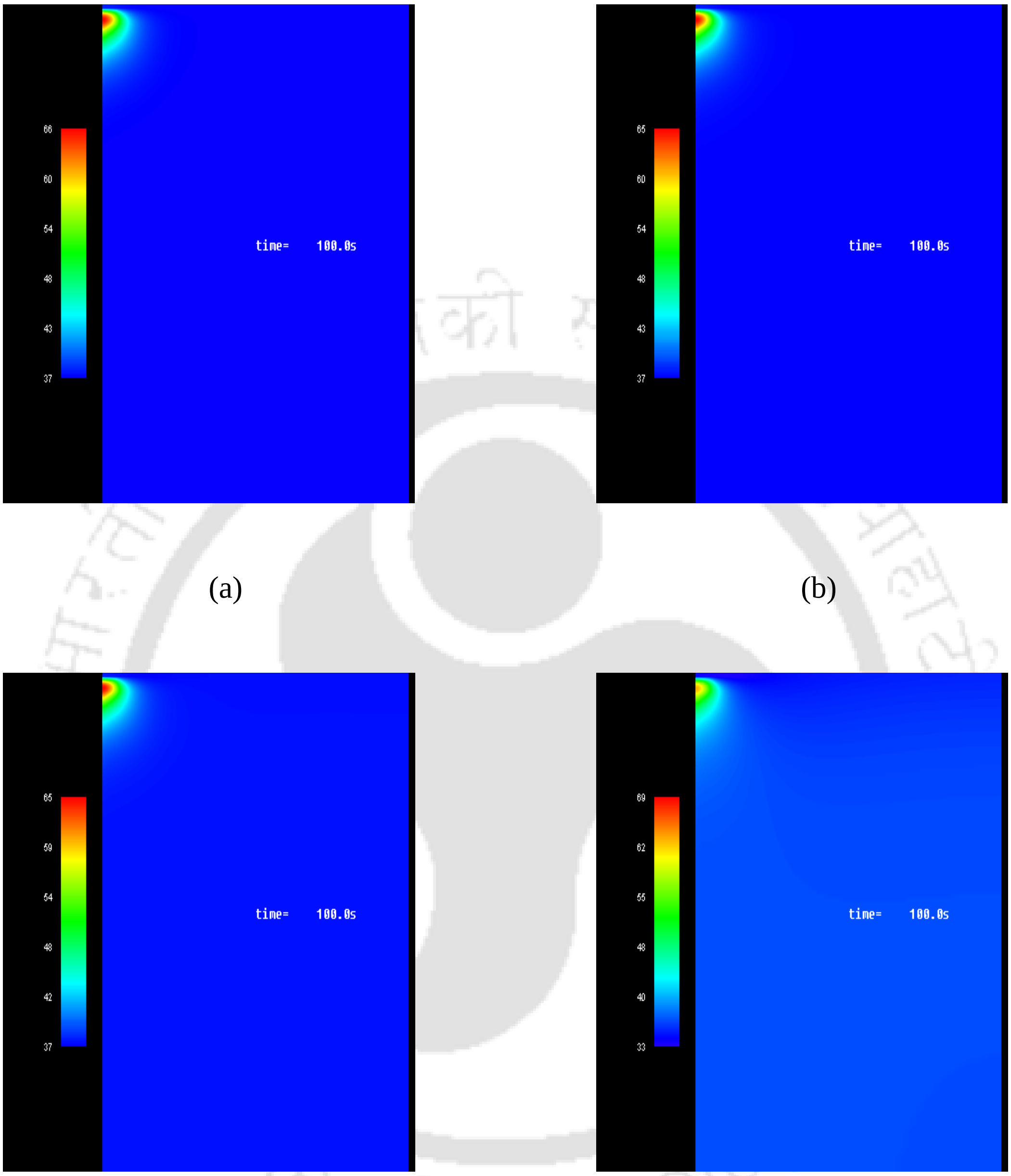

(a) (b)

(c) (d)

Figure 4.14. Axisymmetric temperature distribution for different *h* (a)100, (b) 200, (c) 400, and (d) 800 all with10 W of power.

Calculations using the same input power for different beam radius was performed for 1 mm, 2 mm, 3 mm and 4 mm of beam radius. Center temperature distribution (Fig. 4.15.) and 2-D plot (Fig.4.16.) are presented.

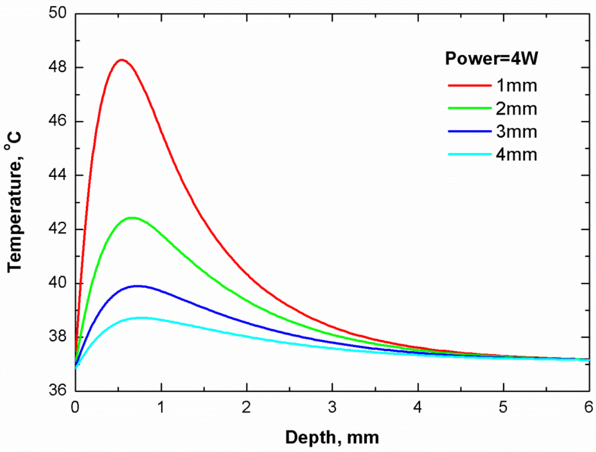

Figure 4.15. Temperature distribution at center for different beam radius with power 4 W.

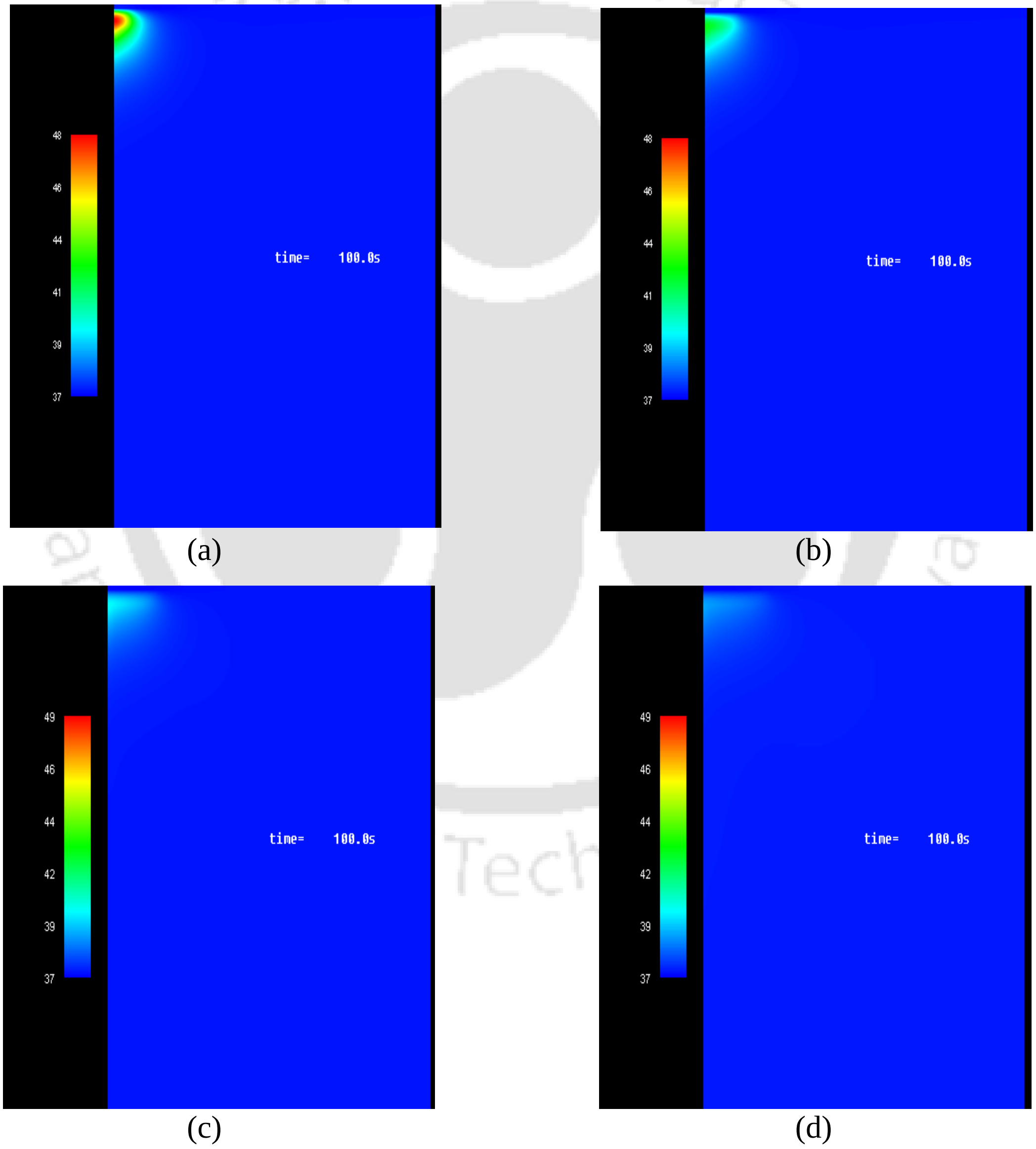

(a) (b)

(c) (d)

Figure 4.16. Axisymmetric temperature distribution for beam radius (a) 1 mm, (b) 2 mm, (c) 3 mm and (d) 4 mm with power 4 W.

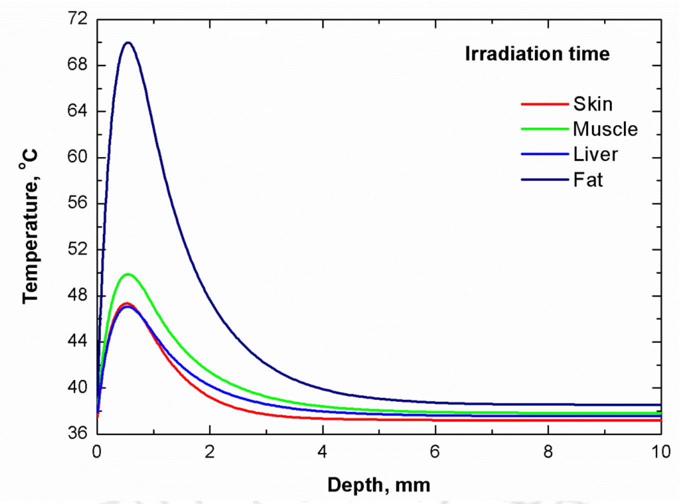

Figure 4.17. Temperature distribution at center with different tissues with $h = 800\,\mathrm{W/m^2 \cdot K}$ at exposure time of t = 100 s.

Finally, the temperature distributions in different tissues were obtained and results are presented for centerline temperature (Fig. 4.17) and 2-D axisymmetric temperature distribution (Fig. 4.18).

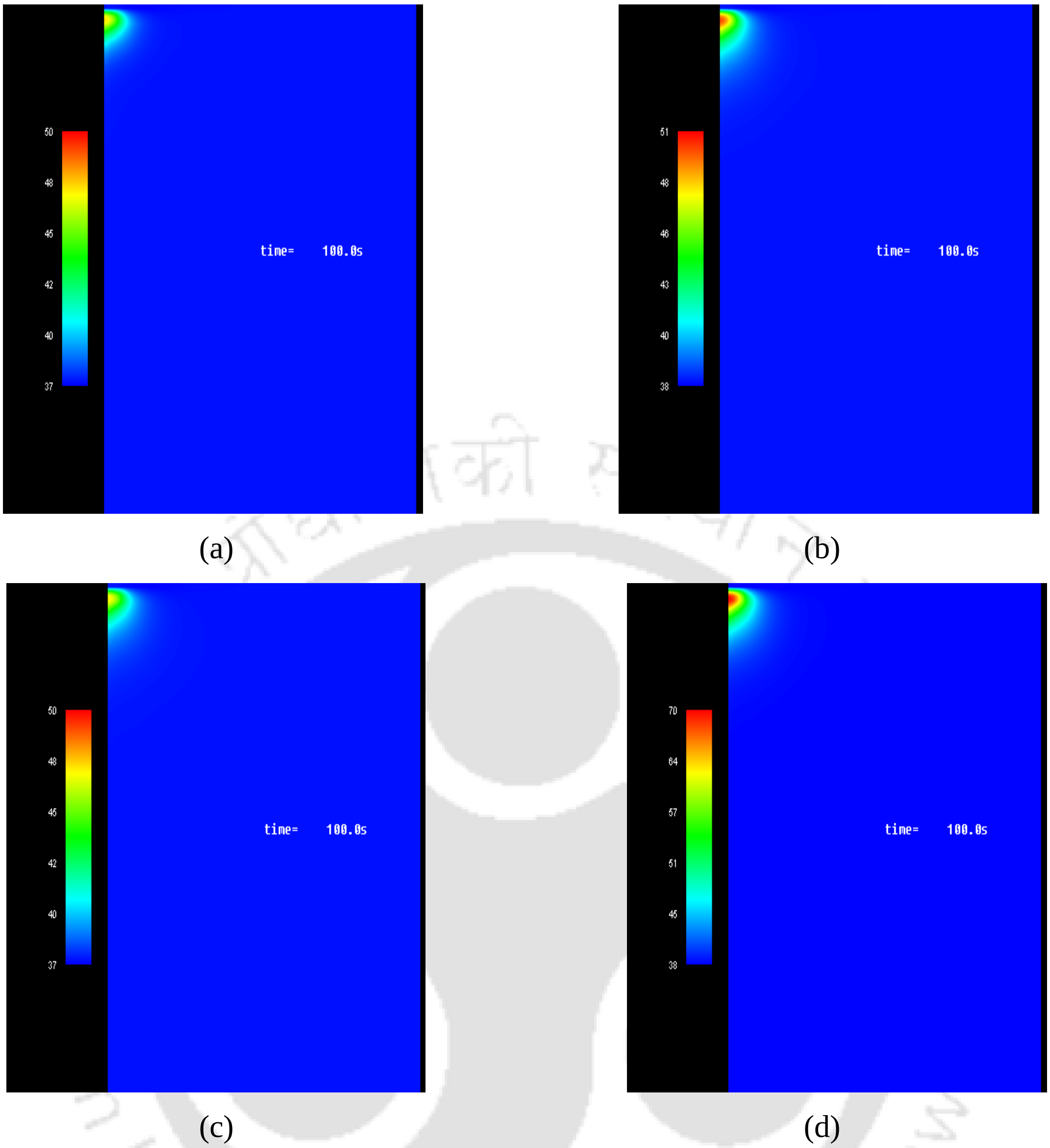

(a) (b)

(c) (d)

Figure 4.18. Axisymmetric temperature distribution for (a) skin, (b) muscle, (c) liver and (d) fat tissue for beam radius 1mm with power 4 W.

4.3 Optical window Contact Cooling during Laser Induced Thermal Therapy

Consideration is given to an axisymmetric cylindrical tissue (Fig. 4.19a) with radius R and height Z. A *cw* laser with beam radius r_b is incident at the center of the top surface of the tissue (Fig. 4.19a). Along the circumferential direction ϕ, tissue properties and thermal condition are assumed constant. Therefore, the computational domain is a 2-D $r-z$ plane (Fig. 4.19b). In a biological tissue, the heat transfer is mainly due to conduction and blood perfusion, combined with volumetric heat generation resulting from metabolic activities. For such a tissue, heat transfer is governed by Pennes bioheat equation.

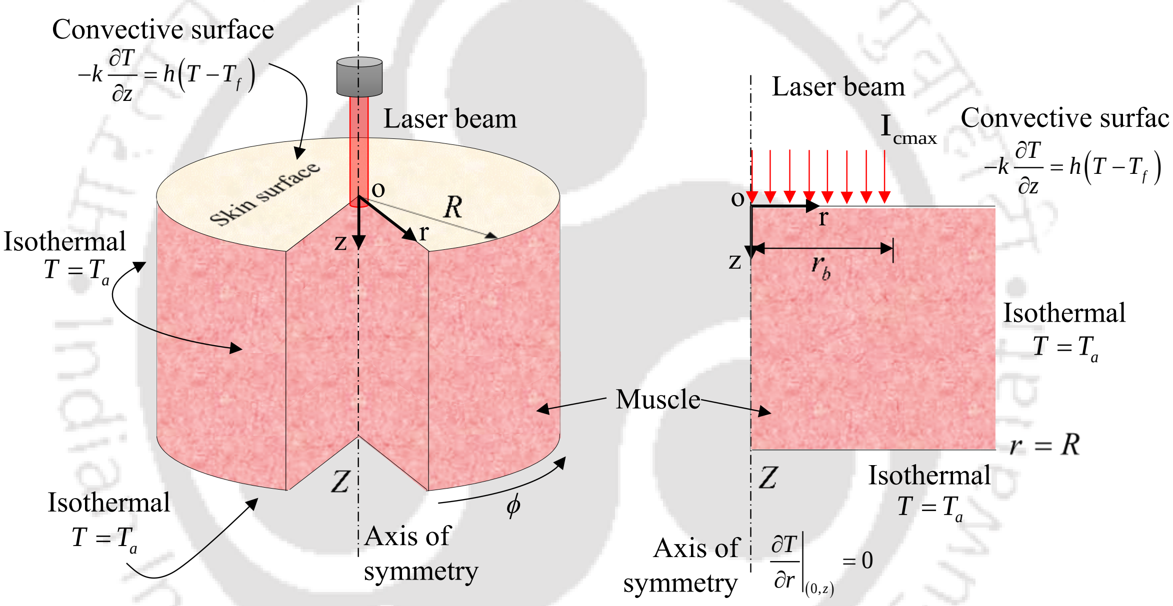

(a) (b)

Figure 4.19. Schematic of single layered (a) cylindrical tissue domain and (b) 2-D computational plane along with the boundary conditions.

With ρ, c_p and k as the density, the specific heat, and the thermal conductivity of the tissue, respectively, for the 2-D cylindrical geometry as shown in Fig. 4.19a, the Pennes bioheat equation considering both conduction and volumetric radiation $\nabla \cdot q_r$ is given by

$$\rho c_p \frac{\partial T}{\partial t}=k\left[\frac{1}{r}\frac{\partial}{\partial r}\left(r\frac{\partial T}{\partial r}\right)+\frac{\partial^2 T}{\partial z^2}\right]+\eta_b \rho_b c_{pb}\left(T_a-T\right)+Q_m-\nabla \cdot q_r \tag{4.4}$$

where ρ_b and c_{pb} are the density and the specific heat of blood, respectively. With T_a as the arterial blood temperature, η_b is the blood perfusion rate and Q_m is the volumetric metabolic heat generation rate.

Radiatively, the tissue with the diffuse-gray boundaries is an optically absorbing, emitting and scattering non-isothermal medium. The left $\left(r=0,\, z\right)$ boundary of the computational domain (Fig. 4.19b) is the central axis of the cylinder, and has symmetry boundary condition $\left(\left.\frac{\partial T}{\partial r}\right|_{(r=0,z)}=0\right)$. The right $\left(r=R,z\right)$ boundary, which is the outer surface of the cylinder and the bottom $\left(r,z=Z\right)$ surface i.e., the core body, are at isothermal condition. The top $\left(r,z=0\right)$ boundary of the tissue is exposed to the ambience, and is at convective cooling condition $\left(-k\left.\frac{\partial T}{\partial z}\right|_{(r,z=Z)}=h\left(T-T_f\right)\right)$. With $\nabla\cdot q_r$ information needed in Eq. (4.4) computed using the DOM, the governing equation (Eq. (4.4)) for the 2-D cylindrical geometry is numerically solved using FVM following the procedures stated in chapter 2.

Next, the study is extended to a multilayer blood perfused and deep seated vascularized tissue under laser irradiation with active contact cooling. Many methods of skin cooling during laser induced hyperthermia and thermal therapy have been proposed by researchers [Altshuler *et al.* 1999, Cheng *et al.* 2014]. Optical window surface contact cooling and cryogenic spray cooling are widely used methods for the skin surface cooling. Contact type cooling using optical windows and spray type cooling using cryogens have been studied by some researchers [Svaasand *et al.* 2003, Patel and Zaidi 1999, Zhou *et al.* 2012]. Zenzie *et al.*(2000*)* studied three different application procedures of cooling agent, viz. passive contact plate cooling, active contact plate cooling and spray cooling.

Optical windows are transparent material which find applications in laser optics, electronics, and medicine [Kim 2007]. For applications in laser induced hyperthermia and thermal therapy procedures, optical windows are used for providing a highly conducting contact cooling material which passes most of light through it [Altshuler *et al.* 1998, Anvari *et al.* 1998]. This provides a way of simultaneously heating the tissue deep inside the surface while preventing thermal damage to the top surface of the skin [Anvari *et al.* 1995a, 1995b]. For contact cooling application, sapphire is the most preferred material because of its wide range of transparency from UV to IR wavelengths, high strength and high conductivity. Optical quality crystalline aluminum oxide or sapphire is characterized by very high thermal conductivity, approximately $23\,\mathrm{W/m\cdot K}$, high stability and hardness. Sapphire also has high threshold for optical damage [Anvari *et al.*1998].

In the present study, three new optical materials with thermal conductivity comparable or greater than sapphire are examined for suitability of contact cooling applications. The new optical window materials viz., yttrium aluminium garnet (YAG), lithium tantalate ($LiTaO_3$), and magnesium oxide doped lithium niobate ($MgO{:}LiNbO_3$) were selected based on their ability to pass light between wavelength range of medical lasers, i.e., between 500 nm to 1200 nm [Gervais and Fonseca 1998, Palik 1998, Tropf 1998, Tropf and Thomas 1998]. Other important properties for selection were high conductivity, low reflection loss, stability, hardness, insolubility, non-toxicity and high threshold for optical damage. Yttrium aluminum garnet is a synthetic, hard material with wide transparency range between UV and IR. Lithium tantalate and magnesium oxide doped lithium niobate, apart from having high thermal conductivities, also exhibits wide range of transparent window ranging from UV to IR wavelengths. A theoretical assessment of suitability of these four materials for contact cooling application is done.

Cryogenic liquids, also known as cryogens, have very low boiling point (typically less than -30°C) [Hsieh and Tsai 2006, Li *et al.* 2014a, Torres *et al.* 1999]. At low temperatures, cryogens are in liquid state. When exposed to normal temperature and pressure conditions, cryogens expand into large volume of gas. For spray cooling, the scattering from the cryogen is ignored, as desired results can be achieved by varying the laser power. The two cryogens selected in the present study are HFO-1234yf or R1234yf (boiling point -30^{o}C) and liquid CO_2 (boiling point -57^{o}C), and the selection criteria followed are the low boiling point, low global warming potential and low toxicity [Perkins and Huber 2011].

In the present study, a quantitative evaluation of skin surface cooling during laser induced hyperthermia and thermal therapy is performed. Schematic of the multilayer skin tissue with deep vascularized soft tissue is shown in Fig. 4.20a. The tissue consists of skin layers, viz., epidermis, dermis, and fatty soft tissue. The fourth (bottom) layer of the tissue is a vascularized tissue with embedded large blood vessel pairs. Heat transfer in the top three layers and the fourth (bottom) layer are modelled using the blood perfusion based Pennes bioheat equation [Bhowmik *et al.* 2013], and the blood velocity based Weinbaum-Jiji bioheat equation, respectively. The computational geometry, as shown in Fig. 2.4a in chapter 2, is a 2-D axisymmetric cylinder, with a 2-D planar solution space. The 3-D control volume for solution of RTE is shown in Fig 2.4b (Chapter 2). The volumetric radiative source term, in the form of the divergence of radiative heat flux is incorporated in the Pennes bioheat as well as the Weinbaum-Jiji models. With radiative information computed using the DOM, the bioheat energy equations are solved using the FVM as discussed in chapter 2. Laser of wavelength 1064 nm, irradiated on the top surface of 2-D cylindrical tissues geometry is considered.

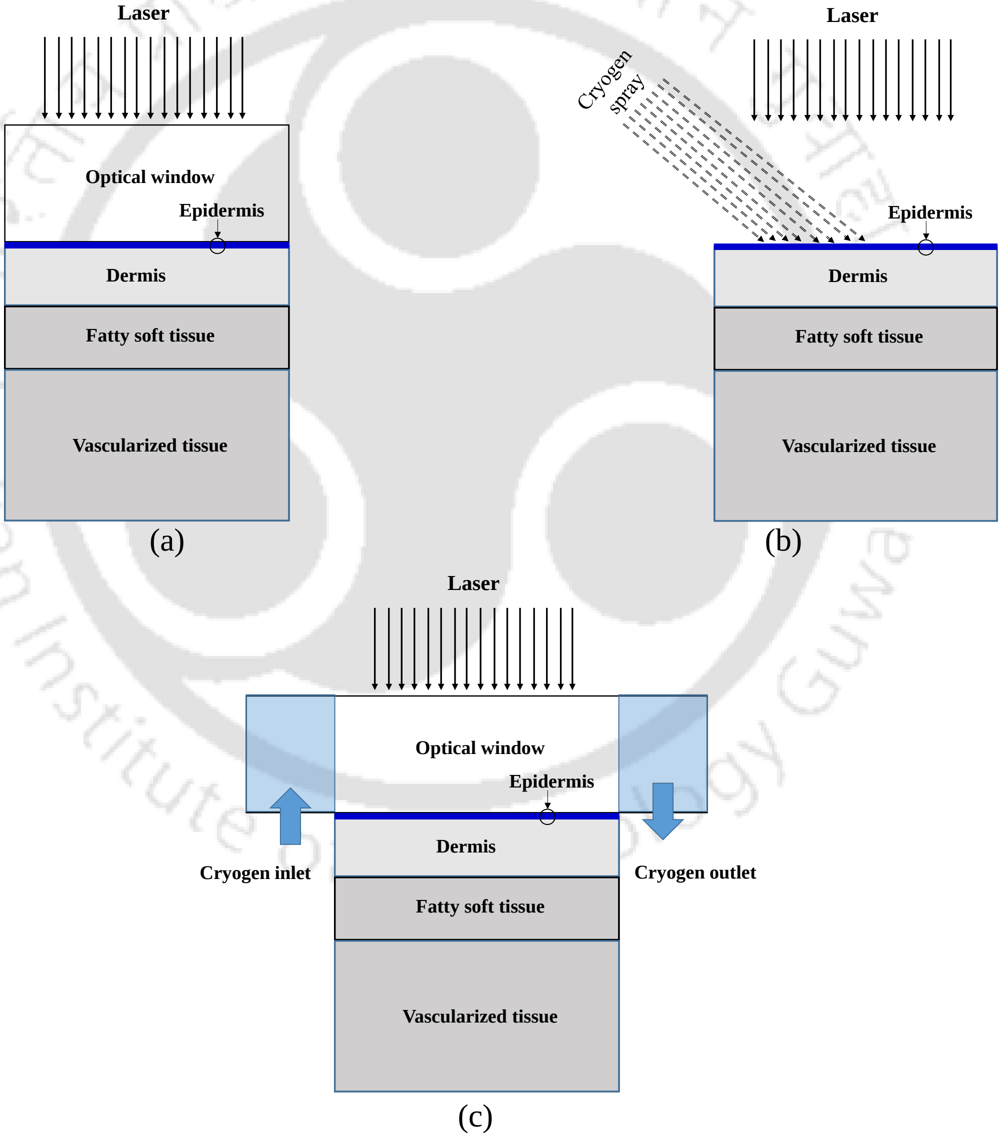

Figure 4.20. Laser irradiated multilayer tissue geometry with (a) optical window contact (b) cryogenic spray and (c) cryogen cooled optical window contact cooling systems.

A careful survey of literature revels that the study on the vascularized tissue under laser irradiation is lacking. In the present study, skin surface cooling, for both optical window contact and cryogenic spray types, a realistic scenario of laser heating of multilayer skin with deep seated tissue embedded with thermally significant blood vessels is presented. A perfect contact between the skin and the optical window is assumed for all cases of contact cooling. In practice, a near perfect contact can be achieved by applying high conductive gels on the skin.

With the volumetric radiative source term, i.e., the divergence of radiative heat flux $\nabla \cdot q_r$ incorporated, the Pennes bioheat equation and Weinbaum-Jiji equation are given by

$$\rho c_p \frac{\partial T}{\partial t} = k\left[\frac{1}{r}\frac{\partial}{\partial r}\left(r\frac{\partial T}{\partial r}\right)+\frac{\partial^2 T}{\partial z^2}\right]+\eta_b \rho_b c_{pb}\left(T_a - T\right)+Q_m-\nabla \cdot q_r \tag{4.5}$$

$$\rho c\frac{\partial T}{\partial t} = \frac{1}{r}\frac{\partial}{\partial r}\left(rk_{eff}\frac{\partial T}{\partial r}\right)+\frac{\partial}{\partial z}\left(k_{eff}\frac{\partial T}{\partial z}\right)-\nabla \cdot q_r + Q_m \tag{4.6}$$

The left $\left(r=0,\, z\right)$ boundary of the computational domain (Fig. 4.20a) is the central axis of the cylinder and has the symmetry boundary condition $\left(\left.\frac{\partial T}{\partial r}\right|_{(r=0,z)}=0\right)$. The right $\left(r=R,z\right)$ boundary, which is the outer surface of the cylinder and the bottom $\left(r,z=Z\right)$ surface i.e., the core body, are at isothermal condition. The top $\left(r,z=0\right)$ boundary of the tissue is exposed to optical window of cryogenic spray. The optical window in case of contact cooling or the skin surface in case of direct spray cooling is considered under convective cooling condition, i.e., $\left(-k\left.\frac{\partial T}{\partial z}\right|_{(r,z=Z)}=h\left(T-T_f\right)\right)$. A dynamic heat transfer coefficient relation is used for cryogen spray cooling. This relation (Eq. 4.7) gives a time dependent effect of cryogen spray [Li *et al.* 2014a],

$$h_o^*(\tau) = \left(\frac{h_{\text{cryo}}(0,\tau)}{h_{\text{o,max}}}\right) = \begin{cases} \tau & \tau \le 1.0 \\ 1.0 - 0.35(\tau - 1) & 1.0 < \tau \le 3.0 \\ 0.3 - 0.002(\tau - 3) & 3.0 < \tau \le 8.0 \\ 0.2 - 0.0125(\tau - 8) & 8.0 < \tau \end{cases} \tag{4.7}$$

where $h_o^*(\tau)$ is the normalized convection heat transfer coefficient, $h_{\text{cryo}}(0,\tau)$ is the surface heat convection coefficient, τ is the non-dimensional time, and $h_{\text{o,max}}$ is the maximum heat transfer coefficient during cryogenic spray. Although, this relation is experimentally available for cryogen R134a [Aguilar *et al.* 2003, Franco *et al.* 2005], it is assumed that this relation is applicable to R1234yf and liquid CO_2.

4.3.1 Results and Discussion – Contact Cooling

For validation of WJ model using the FVM formulation, a 2-D cylindrical tissue $(R \times Z = 5\,\text{mm} \times 13\,\text{mm})$ is considered. The top and the outer boundaries are kept at the core body temperature i.e., 37°C. The bottom boundary is subjected to convective cooling with ambient temperature of 20°C, and convective heat transfer coefficient of $20\ \text{W/m}^2 \cdot \text{K}$. Figures 4.21a and 4.21b show the steady-state centerline $(r = 0, 0 \le z \le Z)$ and radial $(0 \le r \le R, z = 0)$ temperature distributions, respectively, obtained using the developed FVM solver, and the results are compared with that obtained using FEM-based commercial solver, COMSOL Multiphysics. Results are found to be in good agreement.

Next, for a 2-D axisymmetric cylindrical geometry, a contact sapphire glass over multilayer tissue irradiated with laser of wavelength 1064 nm is modeled as shown in Fig. 4.20. Sapphire thickness of 0.5 mm is considered. The skin layer consists of three types of tissues, viz., epidermis, which is the outermost layer, dermis and blood perfused soft tissue. The thickness of epidermis, dermis and soft tissue are taken as 0.1 mm, 2.0 mm, and 2.4 mm, respectively. The last, the innermost layer of the tissue contains large blood vessel pairs, and the thickness of this layer is as 3.0 mm.

The thermophysical and optical properties of sapphire and different tissues are given in Table 4.2 and Table 4.3, respectively. A laser with wavelength $\lambda = 1064\,\text{nm}$ is considered for the simulation. This wavelength exhibits decent depth of reach in most biological tissues. This wavelength is the characteristic of Nd:YAG type of laser. For a continuous wave laser irradiation over the top surface of geometry (Fig. 4.20a), a centerline temperature distribution is obtained for bean radius of 1 mm. The centerline temperature at exposure time level 5 s for different laser powers with beam radius of 1 mm and heat transfer coefficient $h = 0.0\,\mathrm{W/m^2K}$, is shown in Fig. 4.22a.

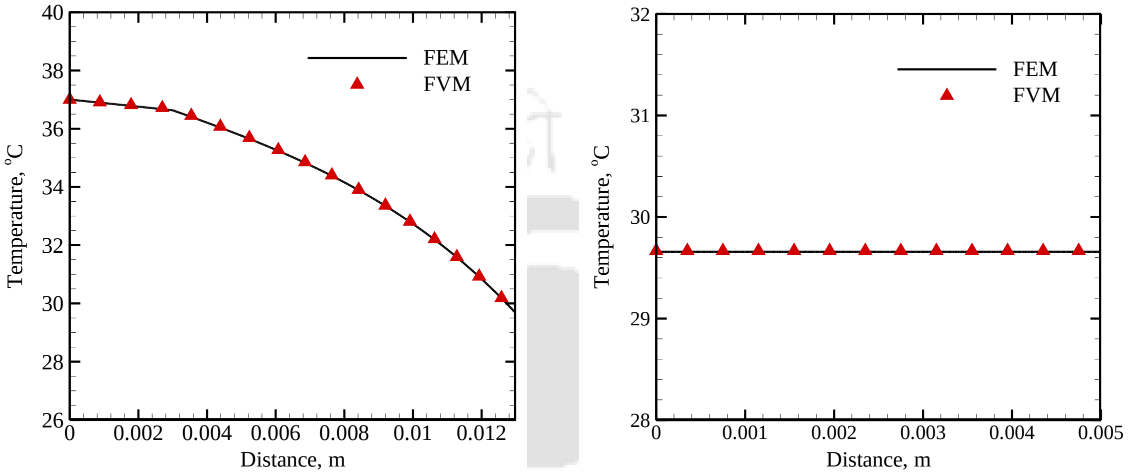

(a) (b)

Figure 4.21. Comparison of the steady-state (a) centerline $(r = 0, 0 \le z \le Z)$ and (b) surface $(0 \le r \le R, z = 0)$ temperature distributions in 2-D cylindrical tissue in the absence of laser irradiation.

For a laser exposure time of 10 s, the centerline temperature for different laser power with beam radius 1 mm and heat transfer coefficient $h = 0.0\,\mathrm{W/m^2 \cdot K}$, is shown in Fig. 4.22b. From Fig. 4.22, it is observed that with heat transfer coefficient h kept as low as 0.0 W/(m^2 K), the surface temperature is maintained at the outside air temperature $T_f = 25^{\mathrm{o}}\mathrm{C}$.

Table 4.2. Thermophysical properties of sapphire and different tissues [Anvari *et al.*1998].

Thermo-physical properties	Sapphire	Epidermis	Dermis	Soft Tissue	Vascularized Tissue
$k\left(\frac{\mathrm{W}}{\mathrm{m/K}}\right)$	23.0	0.24	0.45	0.628	0.5441 Calculated separately
$\rho_{tissue}\left(\frac{\mathrm{kg}}{\mathrm{m}^3}\right)$	4000.0	1190.0	1116.0	1000.0	1000.0
$c_p\left(\frac{\mathrm{J}}{\mathrm{kg/K}}\right)$	760.0	3590.0	3300.0	4187.0	4187.0
$Q_m\left(\frac{\mathrm{W}}{\mathrm{m}^3}\right)$	0.0	368.0	368.0	1190.0	1190.0
$\eta\left(\frac{1}{s}\right)$	0.0	1.0e-7	0.00125	0.003	0.0

Table 4.3. Optical properties of sapphire and different tissues [Anvari *et al.*1998].

Optical properties	Sapphire	Epidermis	Dermis	Soft tissue	Vascularized tissue
$\beta(1/m)$	21.0×10^{-6}	8.592×10^{3}	8.286×10^{3}	1100.0	1100.0
ω	1.0	0.9586	0.994	0.963	0.963

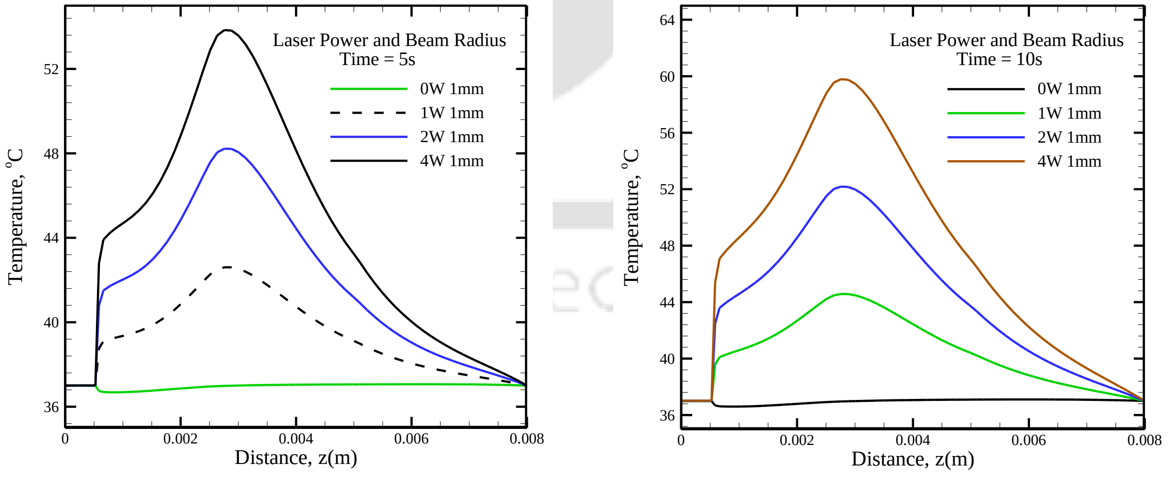

(a) (b)

Figure 4.22. Centerline temperature at time level (a) 5 s for different laser power with beam radius of 1 mm and heat transfer coefficient $h = 0.0\,\mathrm{W/m^2 \cdot K}$, (b) 10 s for different laser power with beam radius of 1 mm and heat transfer coefficient $h = 0.0\,\mathrm{W/m^2 \cdot K}$.

Figure 4.23a shows centerline temperature at different time levels for laser power of 1W with beam radius of 1 mm and heat transfer coefficient $h = 0.0\,\mathrm{W/m^2 \cdot K}$. Figure 4.23b shows centerline temperature at different time levels for laser power of 1W with beam radius of 1 mm and heat transfer coefficient $h = 0.0\,\mathrm{W/m^2 \cdot K}$. It is evident from Fig. 4.23 that with increase in laser power density, for same laser exposure time, the temperature rise in the tissue is more. A comparison of centerline temperature at exposure time of 5 s with laser power of 1W for different beam radius is presented in Fig. 4.24.

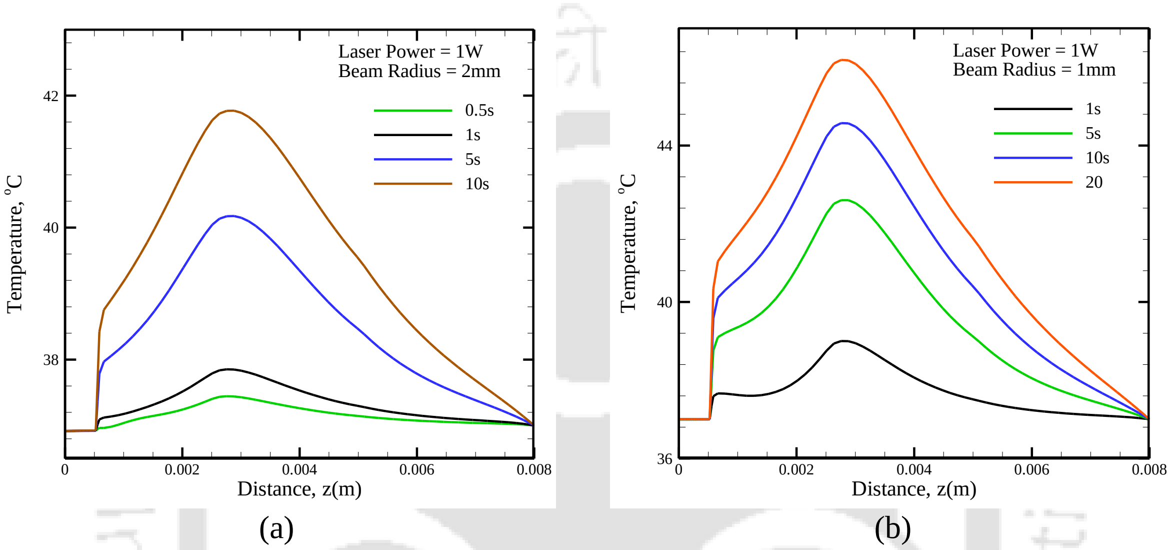

Figure 4.23. Centerline temperature at different time level for different laser power of 1W and (a) 2 mm and (b) 1 mm, with heat transfer coefficient $h = 0.0\,\mathrm{W/m^2 \cdot K}$.

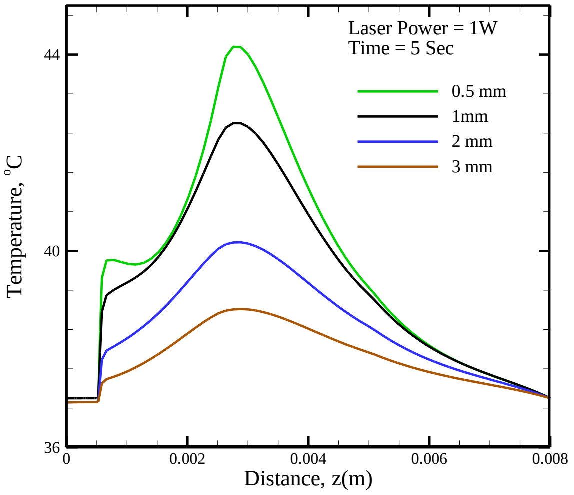

Figure 4.24. Centerline temperature at exposure time of 5 s with laser power of 1 W for different beam radius.

Without sapphire and convective cooling, Figs. 4.25a and 4.25b show contour plots with and without laser irradiation, respectively at time 5s. In case of laser irradiation, the exposure time, power and beam radius are 5s, 1 W and 1 mm, respectively. From Fig. 4.25b, it is observed that, the skin surface temperature can reach to a very high value (310°C). This thus necessitates the need of surface cooling mechanism is any such procedures.

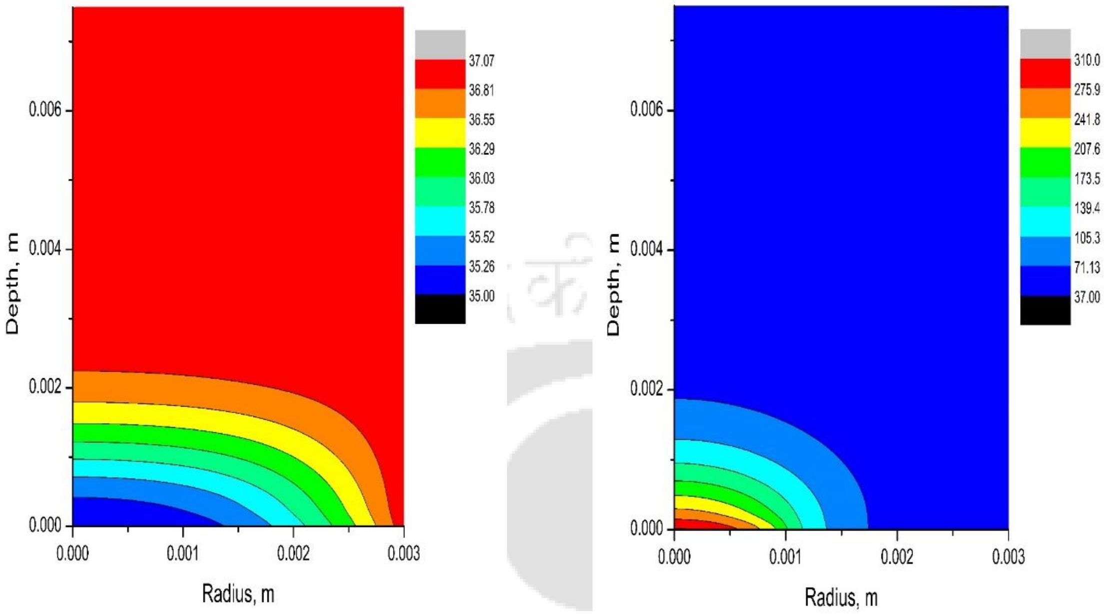

(a) (b)

Figure 4.25. Contour plot at exposure time of 5 s with laser power of (a) 0 W, and (b) 1 W with a beam radius of 1 mm, without sapphire and heat transfer coefficient $h = 0.0\,\mathrm{W/m^2 \cdot K}$.

With laser power of 1 W, beam radius of 1 mm for laser irradiation time 5 s, without sapphire, temperature contours at exposure time 5 s for heat transfer coefficient $h = 25\,\mathrm{W/m^2 \cdot K}$ and $h = 100\,\mathrm{W/m^2 \cdot K}$ are shown in Figs. 4.26a and 4.26b, respectively. It is observed that though with increase in heat transfer coefficient, the overall tissue temperature decreases, the maximum temperature still remains at the skin surface.

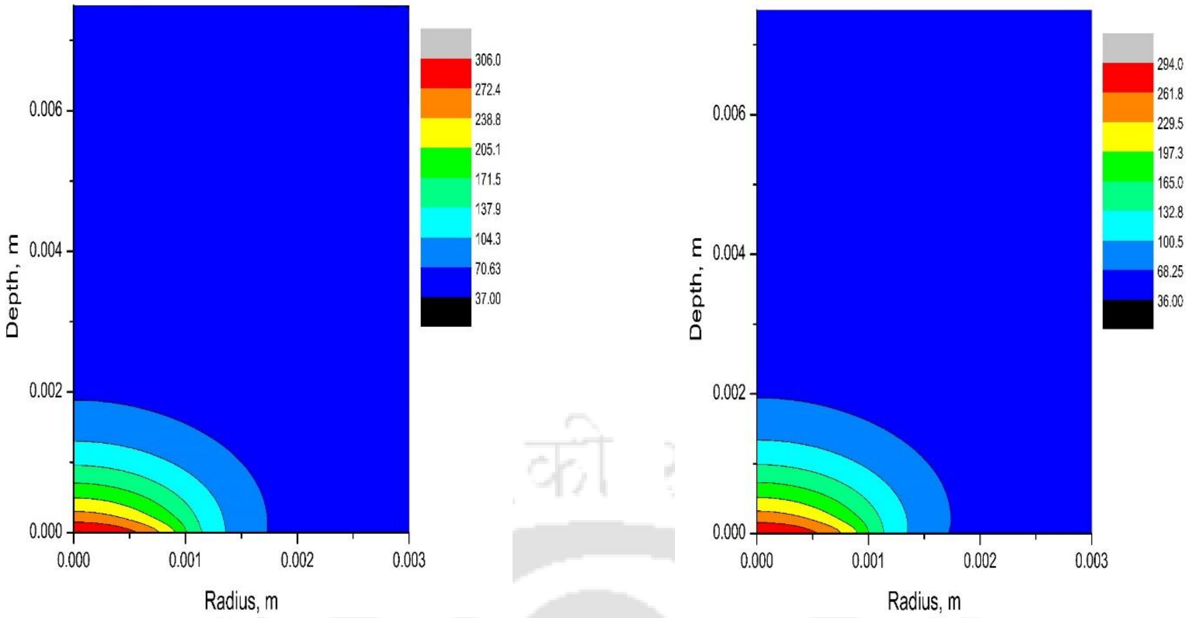

(a) (b)

Figure 4.26. Contour plot at exposure time of 5 s with laser power of (a) 1 W and beam radius of 1 mm, without sapphire and heat transfer coefficient $h = 25\,\mathrm{W/m^2 \cdot K}$, and (b) 1 W and beam radius of 1 mm, without sapphire and heat transfer coefficient $h = 100\,\mathrm{W/m^2 \cdot K}$.

Figure 4.27 shows comparative contour plots at exposure time of 5 s with laser power of 1 W and beam radius of 1 mm, without sapphire (Fig. 4.27a) and with sapphire (Fig. 4.27b), both with heat transfer coefficient $h = 200\,\mathrm{W/m^2 \cdot K}$. It is evident from Fig. 4.27 that introduction of sapphire window as a contact cooling agent provided better cooling of the skin surface.

A comparison of effect of different laser power on temperature evolution in tissue with sapphire window for skin cooling is presented in Fig. 4.28. Figure 4.28a shows a contour plot at exposure time of 5 with laser power of 2 W and beam radius of 1 mm. Figure 4.28b shows a 2-D contour plot at exposure time of 5 s with laser power of 4 W and beam radius of 1 mm.

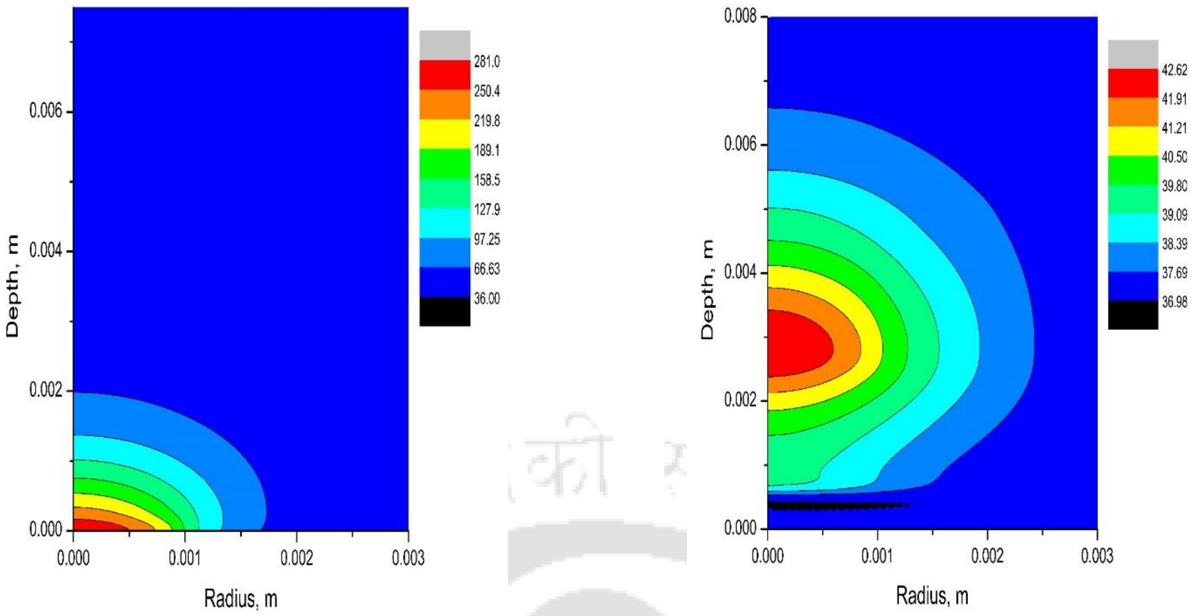

(a) (b)

Figure 4.27. Contour plot at exposure time of 5 s with laser power of 1 W and beam radius of 1 mm (a) without sapphire and (b) with sapphire and with $h = 200\,\mathrm{W/m^2 \cdot K}$.

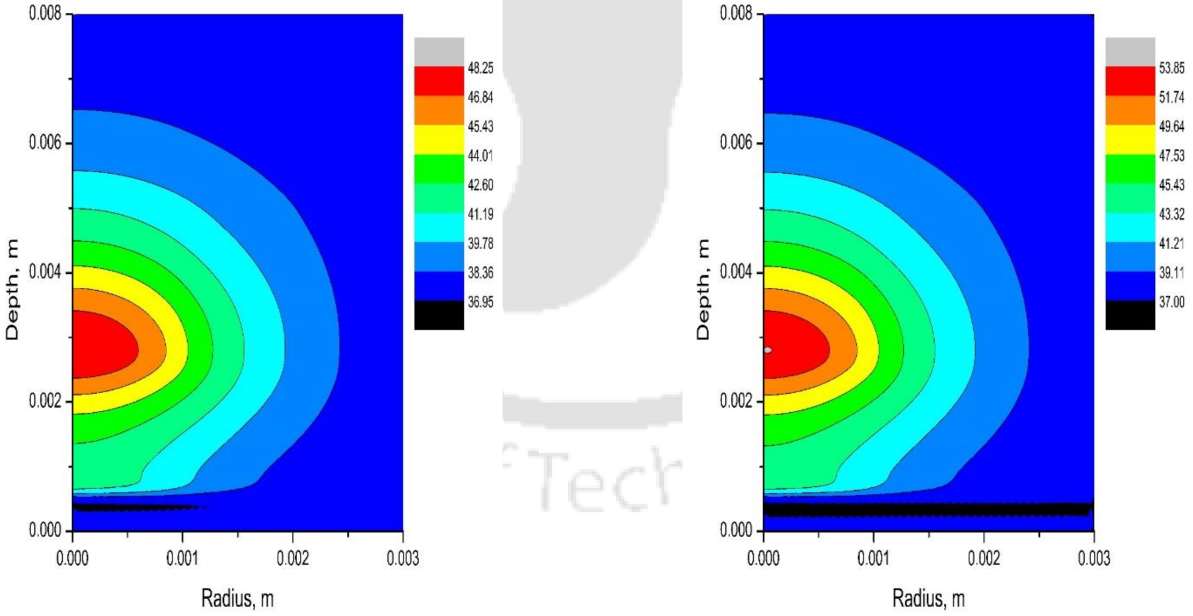

(a) (b)

Figure 4.28. Contour plot at exposure time of 5 s with laser power of (a) 2 W and beam radius of 1 mm, and (b) 4 W and beam radius of 1 mm.

The centerline temperature distribution at exposure time of 5 s with laser power of 1W for beam radius of 1 mm at different heat transfer coefficient h is shown in Fig. 4.29a. Figure 4.29b shows the centerline temperature at exposure time of 0.5 s and 1 s with laser power of 0, 1 and 2 W and for beam radius of 1 mm. A comparison of centerline temperature at exposure time of 1 s and 5 s with laser power of 0 W and 1W for beam radius of 1 mm is shown in Fig. 4.30a. Figure 4.30b shows centerline temperature at exposure time of 1 s and 5 s with laser power of 1 W and beam radius of 1 mm, with and without sapphire. Figure 4.31 shows centerline temperature at exposure time of 1 s with laser power of 1 W and beam radius of 1 mm, with and without sapphire and with heat transfer coefficient $h = 100\,\mathrm{W/m^2 \cdot K}$, and $h = 200\,\mathrm{W/m^2 \cdot K}$.

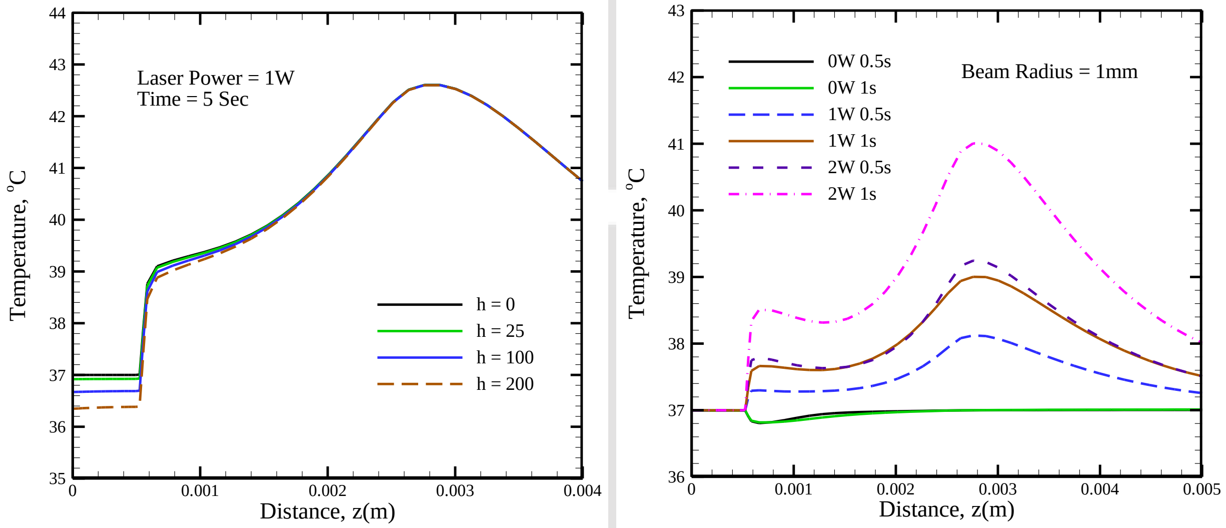

(a) (b)

Figure 4.29. Centerline temperature at exposure time of (a) 5 s with laser power of 1W for beam radius of 1 mm at different heat transfer coefficient, h. and (b) 0.5 s and 1 s with laser power of 0, 1 and 2 W and for beam radius of 1 mm.

The surface cooling mechanism is adopted in the next study considers active by means of cooling, either by keeping constant isothermal condition of optical window material or forced convective condition with extremely low temperature cryogen. Table 4.3 gives the thermal and physical properties of different layers of skin tissue and vascularized tissue. The effective thermal conductivity of vascularized tissue is calculated using WJ model as discussed in chapter 2. The thickness for epidermis, dermis, soft tissue, and vascularized tissue considered are 100 µm, 2.0 mm, 2.4 mm, and 3.0 mm, respectively. The optical window is taken as 0.5 mm thick while the radius of the cylindrical geometry is taken as 3.0 mm. The thermophysical properties of cryogens are not considered for simulation for simplification, and only the dynamic time dependent convective effect by cryogen spray is considered.

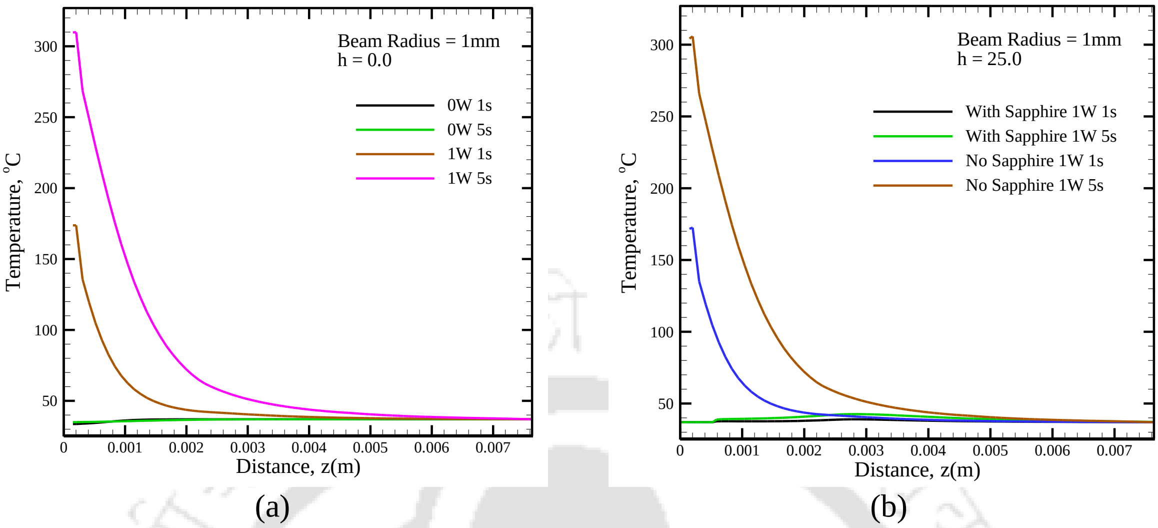

(a) (b)

Figure 4.30. Centerline temperature at exposure time of (a) 1 s and 5 s with laser power of 0 W and 1W for beam radius of 1 mm, and (b) with laser power of 1 W and beam radius of 1 mm, with and without sapphire.

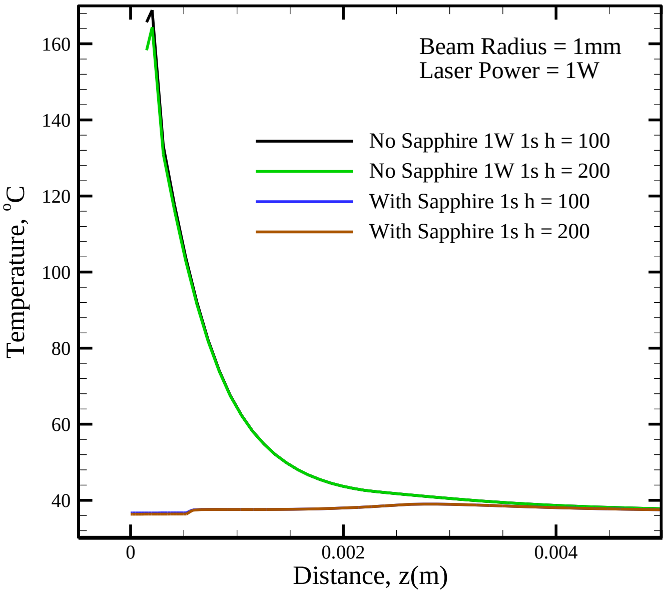

Figure 4.31. Centerline temperature at exposure time of 1 s with laser power of 1 W and beam radius of 1 mm, with and without sapphire and with heat transfer coefficient $h = 100\,\mathrm{W/m^2 \cdot K}$, and $h = 200\,\mathrm{W/m^2 \cdot K}$.

Laser power of 4W with 1.0 mm beam radius is used for irradiation of the top surface of the cylindrical geometry with optical window placed on it. Figure 4.32 shows centerline temperature for different exposure times with different optical windows. With continuous wave laser exposure for time level ranging from 50 ms to 5 s, temperature evolution in multilayer tissue can be observed to be slightly different for four different optical windows at short time level. However, as exposure time increases, this distinction in temperature profile is less (Figs. 4.32a - d). A zoomed-in comparative centerline temperature profiles near the skin surface is presented in Figs. 4.33a-c.

Table 4.4. Thermo-physical properties of optical window materials [Anvari *et al.*1998, Gervais and Fonseca 1998, Palik 1998, Tropf 1998, Tropf and Thomas 1998].

Material / Properties	**Density** $\rho\left(\mathrm{kg/m^3}\right)$	**Specific heat capacity** $c_p\left(\mathrm{J/Kg\cdot K}\right)$	**Thermal conductivity** $k\left(\mathrm{W/m\cdot K}\right)$
Sapphire	3970.0	419.0	22.21
YAG	4560.0	590.0	14.0
Lithium tantalate	7460.0	430.0	46.0
Magnesium oxide doped lithium niobate	4640.0	628.0	38.0

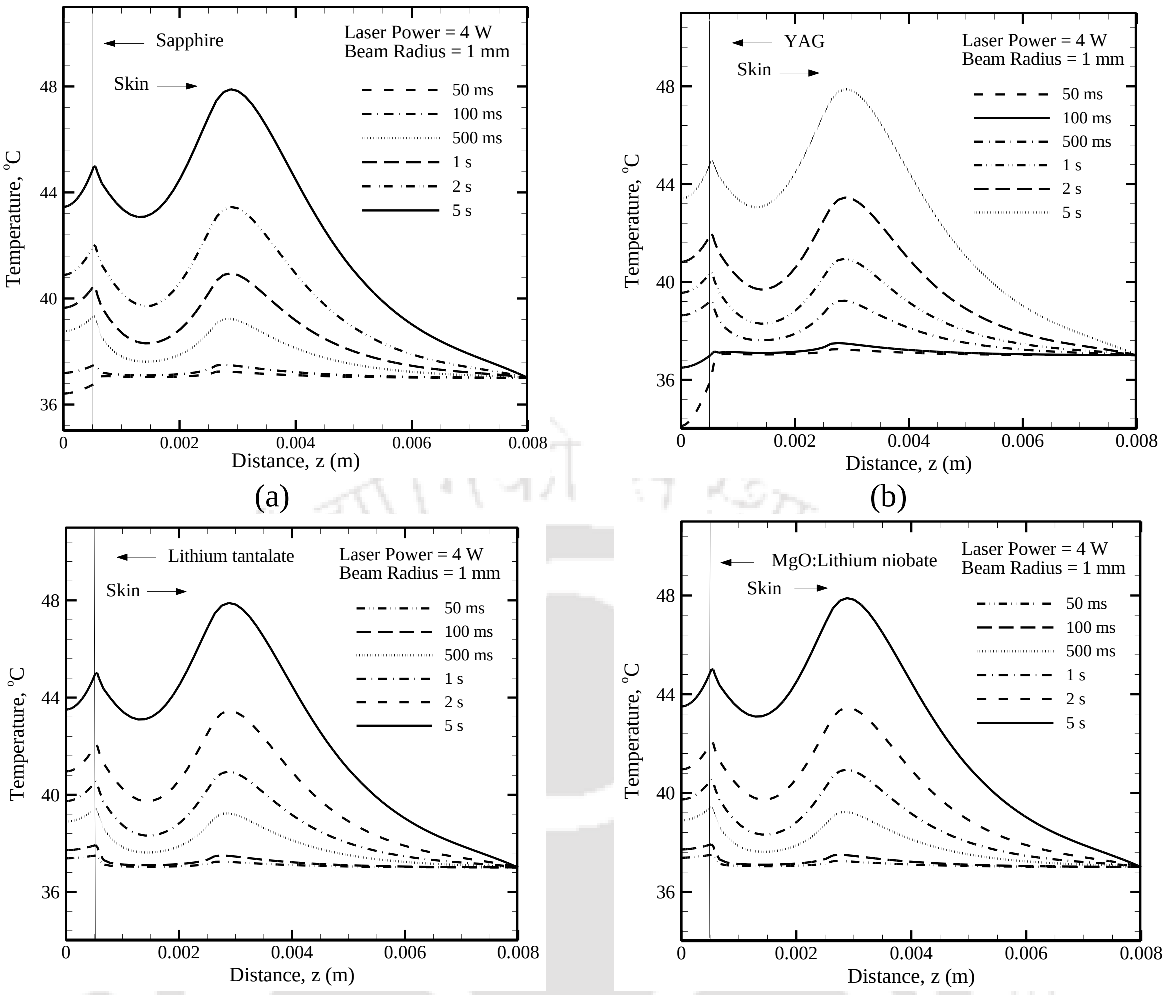

(a) (b)

(c) (d)

Figure 4.32. Centerline temperature of skin tissue for different time of laser exposure with (a) sapphire, (b) YAG, (c) lithium tantalate, and (d) MgO: lithium niobate.

For short time level of laser exposure, i.e. 50 ms (Fig. 4.33a) and 100 ms (Fig. 4.33b), result shows that with other conditions remaining constant, YAG performs better in comparison to other optical windows. Figure 4.33c shows a comparative centerline temperature profiles at exposure time of 1 s. In Fig. 4.33c, a centerline temperature profile of tissue with sapphire window without laser irradiation is presented for providing a reference of how temperature evolves under 1 s exposure.

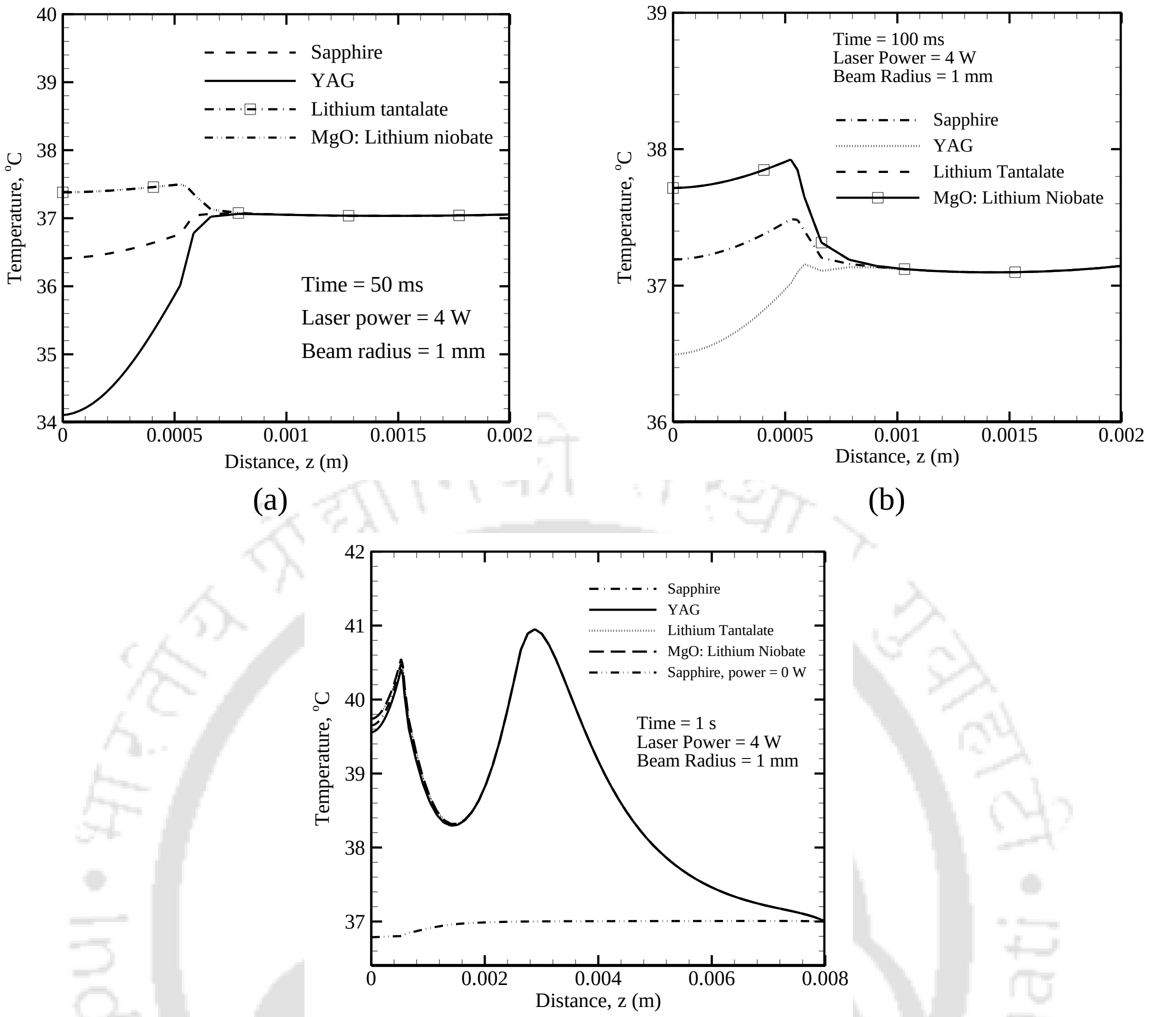

(a)

(b)

(c)

Figure 4.33. Comparison of centerline temperature for different optical windows with laser exposure time of (a) 50 ms, (b) 100 ms, and (c) 1 s.

Figures 4.34a and 4.34b show a skin surface (top layer of epidermis) temperature profile for different optical windows as contact cooling materials. Figure 4.34a shows a comparison of skin surface temperature at laser exposure time of 0.5 s, and it can be seen that YAG provides maximum cooling. However, at time level of 1 s and above, this difference in skin temperature is less, as evident in figure 4.34b. This suggest that for short pulse laser irradiation with contact cooling, YAG provides a better surface cooling than other optical windows.

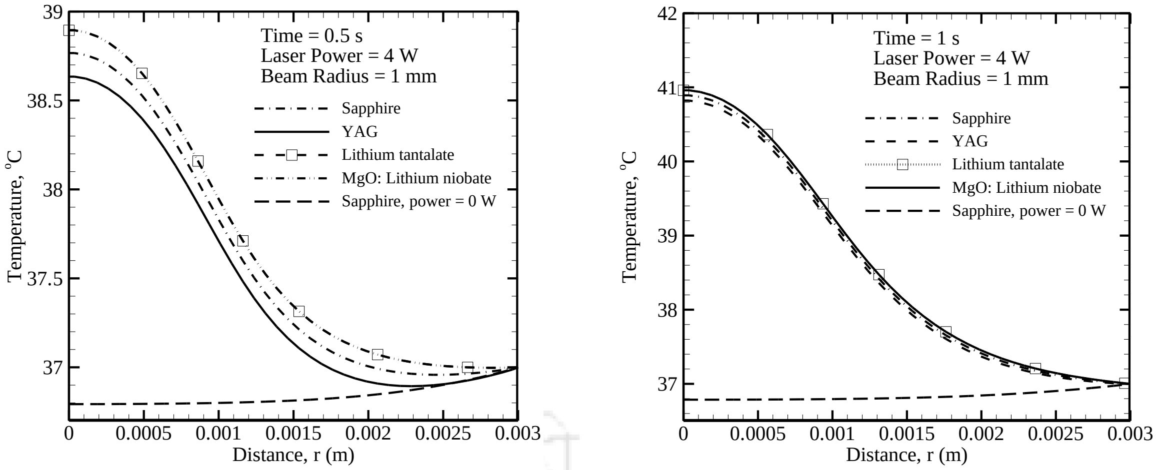

(a) (b)

Figure 4.34. Skin surface temperature at laser exposure time (a) 0.5 s, and (b) 1.0 s, for different optical windows.

Figures 4.35a and 4.35b show the centerline temperature distribution of multilayer skin tissue (Figure 4.20b) when cooled with cryogen spray R1234yf and liquid CO_2, respectively. Figure 4.35c shows surface temperature of laser irradiated multilayer skin tissue (Figure 4.20b) for two cryogens, namely R1234yf and liquid CO_2. Liquid CO_2 has low boiling point than R1234yf, and hence a low surface temperature (Fig. 4.35c) is achieved with the application of liquid CO_2 as cryogen. The initial temperature of pre-cooled window were kept same as of the cryogens (i.e. -57^{o}C in case of liquid CO_2 and -30^{o}C in case of R1234yf).

Cryogen cooled optical window contact cooling as shown in Fig. 4.20c, is the third method of surface cooling in the present study. Figs. 4.36 and 4.37 shows R1234yf and liquid CO2 cooled optical window cooling with different window materials respectively. With laser exposure time of 0.5 s on liquid CO_2 precooled optical window, skin surface temperature of multilayer tissue is presented in Fig. 4.37a. Figure 4.37b shows surface temperature of skin with four different optical windows cooled with liquid CO_2 for a laser exposure time of 1 s. In both the figures (Fig. 4.36 and 4.37), it is evident that for short time of laser irradiation, the combination of liquid CO_2 and YAG provides better cooling of skin surface. For liquid CO_2 cooled YAG optical window, for 5 s laser exposure time, a 2-D temperature contour is presented in Fig. 4.38. The maximum temperature is well inside the tissue and thermal damage of the skin surface is prevented.

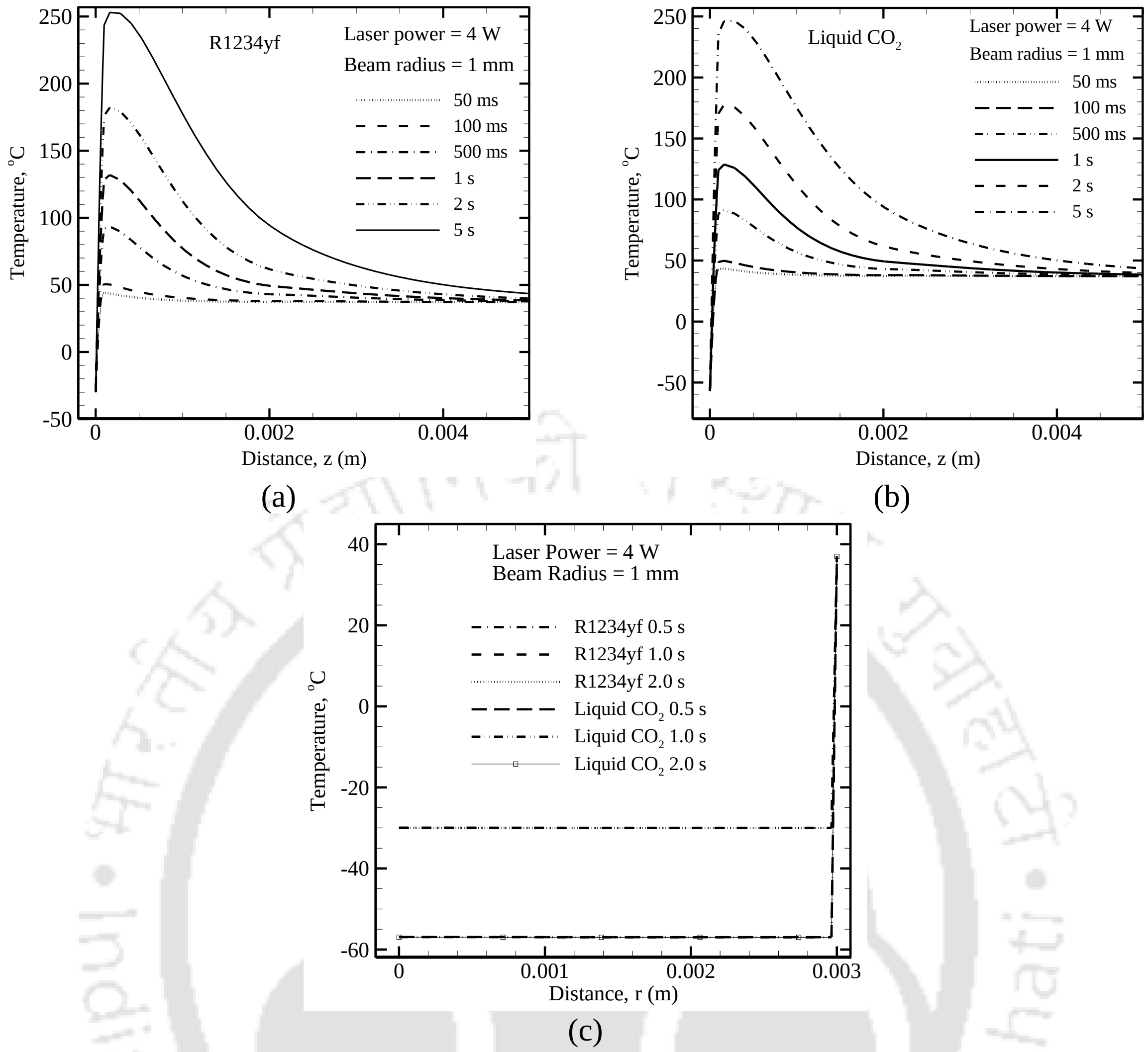

Figure 4.35. Centerline temperature of skin when cooled with cryogen spray (a) R1234yf, and (b) liquid CO_2, and (c) surface temperature of skin with two cryogen at different exposure times.

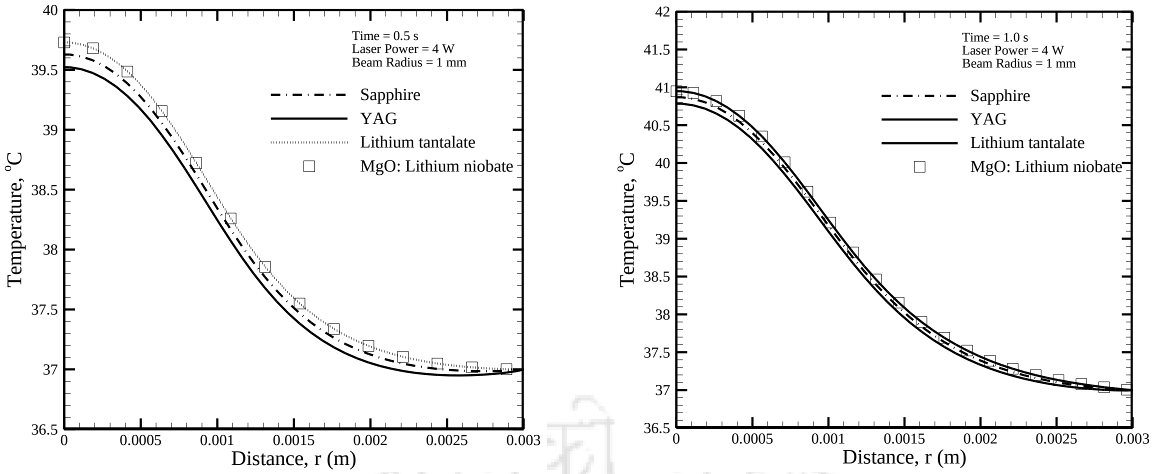

(a) (b)

Figure 4.36. Surface temperature of skin with R1234yf cryogen cooled optical window at laser exposure time of (a) 0.5 s, and (b) 1.0 s.

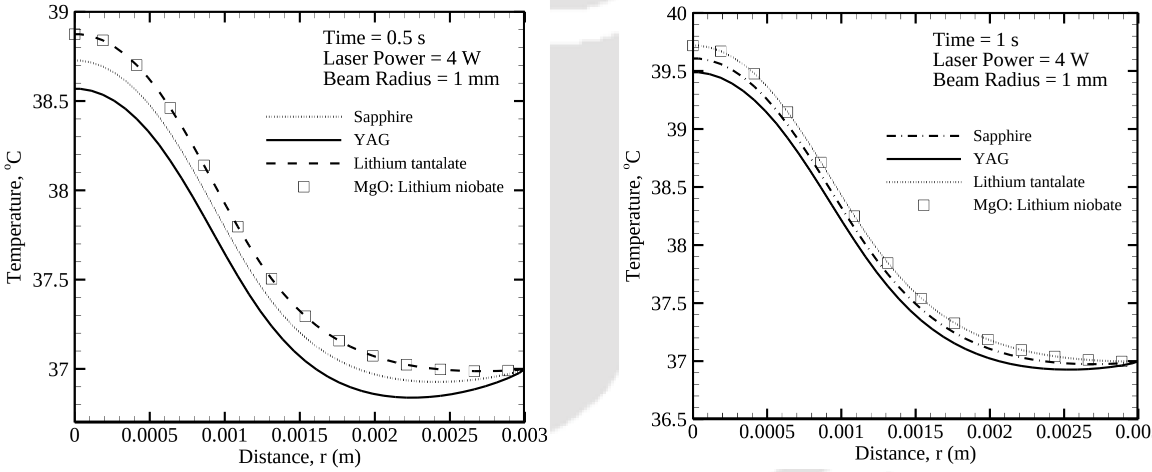

(a) (b)

Figure 4.37. Surface temperature of skin with liquid CO_2 cryogen cooled optical window at laser exposure time of (a) 0.5 s, and (b) 1.0 s.

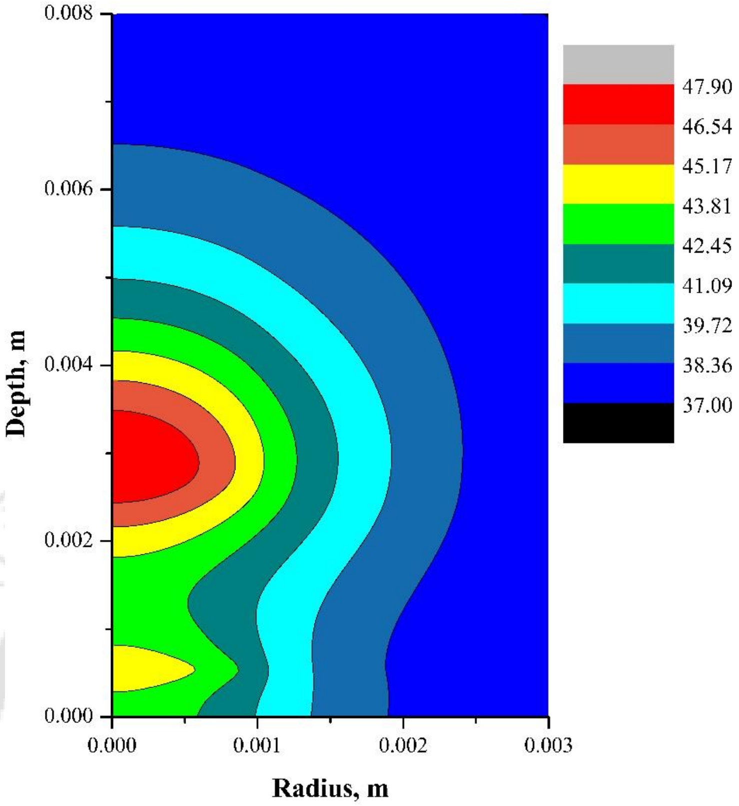

Figure 4.38. A 2-D temperature contour of liquid CO_2 cooled YAG optical window during contact cooling of skin at laser exposure time of 5 s. Laser power of 4 W with 1 mm beam radius is used.

4.4 Closure

One-dimensional and two-dimensional axisymmetric simulations of laser induced hyperthermia were performed and following observations were made:

1. Temperature elevations in biological tissues by laser absorption were calculated and presented for different conditions of laser power and beam radii.

2. A surface cooling mechanism is proposed and simulation using the same was performed for skin surface cooling during laser induced hyperthermia treatment.

3. Using the cooling device, maximum temperature inside the tissue was obtained with controlled temperature on the skin surface. This way, a simultaneous laser irradiation with surface cooling was possible.

In the second part of this chapter, different aspects of skin surface cooling during laser induced hyperthermia and thermal therapy were studied. In the first part of the study, the effect of convective surface cooling on a laser irradiated biological tissue was studied. For a 2-D cylindrical tissue, with volumetric radiative information present in the bioheat equation computed using the DOM, the bioheat equation was solved using the FVM. Without any surface cooling, the maximum temperature was obtained at the skin surface, and the desired temperature rise inside the tissue was not achieved. To prevent skin surface thermal damage, and to raise the temperature inside the tissue above the thermal ablation threshold, convective cooling was provided. With convective cooling, the desired ablation temperature was obtained inside the tissue while the skin surface thermal damage was minimized.

In laser irradiation of skin, cooling of the skin reduces the risk of its damage. This assessment was done using with and without sapphire window with and without convective cooling. A comparison was provided. For this study, a multilayer tissue with blood perfused skin and vascularized deep tissue was considered. A two-equation system for bioheat transfer was used. Volumetric radiation was taken into account. The minimum skin surface temperature and the maximum temperature inside the tissue was achieved when sapphire contact cooling was used.

During laser induced hyperthermia, a comparison of the effects of four different optical window materials placed over the skin surface undergoing convective was also presented. A set of two bioheat equations namely, Pennes bioheat equation for blood perfused tissue and Weinbaum-Jiji bioheat equation for tissue with embedded large blood vessel pairs were simultaneously solved. To account for the volumetric radiation, both the equations contained the term for the divergence of radiative heat flux. The computational domain contained both optical windows and the tissue. A comparative study was presented for two different cryogen with low global warming potential viz. R1234yf and liquid CO_2, for spray cooling during laser induced hyperthermia. A dynamic heat transfer coefficient relation was used for cryogen spray cooling. Finally a combined cryogen - optical window cooling strategy was presented for all combinations of cryogens and optical window materials. The combination of liquid CO_2 and yttrium aluminium garnet was found to be the effective for the short duration laser exposure hyperthermia procedures.

Chapter 5

Transmittance and Reflectance Signals from Laser Irradiated Lung Tissue

---

5.1 Theory

Laser induced thermo-optical signal analysis of biological tissues is an emerging area of research. It finds application in tumor detection and characterization. Transmitted and reflected components of light from the laser irradiated tissue provides specific information about the state of the tissue including the presence of an abnormality such as a tumor. Thermophysical and optical properties of an abnormal tissue are different than that of a healthy one. Laser-tissue interaction and transmittance signals analysis has been reported in literature by many researchers [Muthukumaran *et al.* 2011, Bhowmik *et al.* 2013, Das *et al.* 2003, Welch and Gemert 2011, Trivedi *et al.* 2005, Okutucu and Yener 2007, Katika and Pilon 2006, Niemz 2007]. To model transport of light inside an optically participating medium such a biological tissue, the governing equation is RTE [Modest 2013, Mishra *et al.* 2006, Singh and Mishra 2007].

Thermal response of a lung tissue subjected to a short pulse laser is presented in the present chapter. Consideration is given to a 2-D axisymmetric cylindrical lung tissue with a tumor. Tumor characteristics in the form of temporal transmittance and reflectance signals are analyzed. The RTE, comprising both collimated and diffuse components, is solved using the DOM. Effects of volume fraction of gold-silica nanoshells (i.e. Au/Silica core-shell nanoparticles) and lung volume on transmittance and reflectance signals are studied. Based on absorption and scattering abilities for different stages of lung volume, studies are made with a single and a train of laser pulses. Temporal transmittance signals are distinct for distinct stages of the respiratory lung volume.

Irradiation of a tissue with a short pulse laser, and the resulting transmittance and reflectance signals have been studied by researchers for different geometries. However, no study is reported pertaining to interaction of short-pulse laser with a lung tissue with different stages of respiratory volume. The present work aims at this study with a single and a train of short pulse laser with pulse width $t_p \approx 10^{-9}\,\mathrm{s}$. Transmittance and reflectance signals from the pig lung for four stages of respiratory volumes with and without the presence of a tumor inside the lung has been studied. The lung volume of a respiratory cycle is divided into four discrete values (stages) which have different optical values as given in the literature [Beekyx *et al.* 1997]. The optical properties of lung as a function of respiration are extracted for four different discrete values of lung volume. Experimental studies [Beekyx *et al.* 1997] suggests that the flexible structure of the lung tissue, whose with multilayer air filled sacs, exhibits different optical properties as a function of respiration. Based on the recent literature [Bhowmik *et al.*2014] for transmittance and reflectance signals originating from biological tissues, pulsed laser was opted over *cw* laser. The train of pulse was used to obtain a realistic trend for the analysis of such signals.

Metal-dielectric core nanoparticles (NP) such as gold-silica nanoshells exhibits phenomenon known as surface-plasmon resonance, which when tuned to a particular wavelength, significantly alters the absorption and scattering coefficient of the medium. In cancer treatment and bio-imaging, many researchers [Dombrovsky *et al.* 2011, 2012, Changhong *et al.* 2008, 2009], have done study with Au/silica core-shell nanoparticles infused tissue. Energy absorption by nanoshells and their effect on temperature during laser induced hyperthermia has been discussed in detail by [Dombrovsky *et al.* 2011, 2012, Changhong *et al.* 2008, 2009]. In the present work, with and without a tumor, for different stages of lung respiratory volumes, effect of specific volume fraction of NP on temporal transmittance and reflectance signals is studied. These signals are studied for both single and a multiple (four) laser pulses.

To establish the physical idea of present study, in an imaginary experimental setup, shown in Fig. 5.1, an optical fiber is inserted inside the cancerous lung and a detector system is assumed to capture transmittance signals. A cylindrical tissue-tumor geometry is considered for computation. For a 2-D axisymmetric cylindrical enclosure (Fig. 5.2) having radius R and height Z, with $\theta\left(0 \le \theta \le \pi\right)$ as the polar angle and $\phi\left(0 \le \phi \le 2\pi\right)$ as the azimuthal angle, for any discrete direction $\hat{s} = \left(\sin\theta\cos\phi\right)\vec{e}_r + \left(\sin\theta\sin\phi\right)\vec{e}_\phi + \left(\cos\theta\right)\vec{e}_z$, the transient RTE is given by

[Modest 2013],

$$\frac{1}{c}\frac{\partial I}{\partial t}+\frac{\partial I}{\partial s}=-\beta I+\kappa_a I_b+\frac{\sigma_s}{4\pi}\int_{\Omega'=4\pi} I(\Omega')\Phi\left(\Omega,\Omega'\right)d\Omega' \tag{5.1}$$

where s is the distance in the direction $\hat{s}$, I is the intensity of light, κ_a is the absorption coefficient, σ_s is the scattering coefficient and Φ is the scattering phase function. In Eq. (5.1), $c = 3\times10^8$ m/s is the speed of light and $I_b\left(=\sigma T^4/\pi\right)$ is the black body intensity where $\sigma =$ 5.67×10^{-8} W·m^{-2}·K^{-4} is the Stefan-Boltzmann constant. Short pulse collimated radiation is incident on the top boundary (Fig. 5.2) of the medium with intensity $I_{\mathrm{c,max}}$. As the incident intensity enters and travels through the medium, it starts attenuating. The attenuation of incident intensity is given by

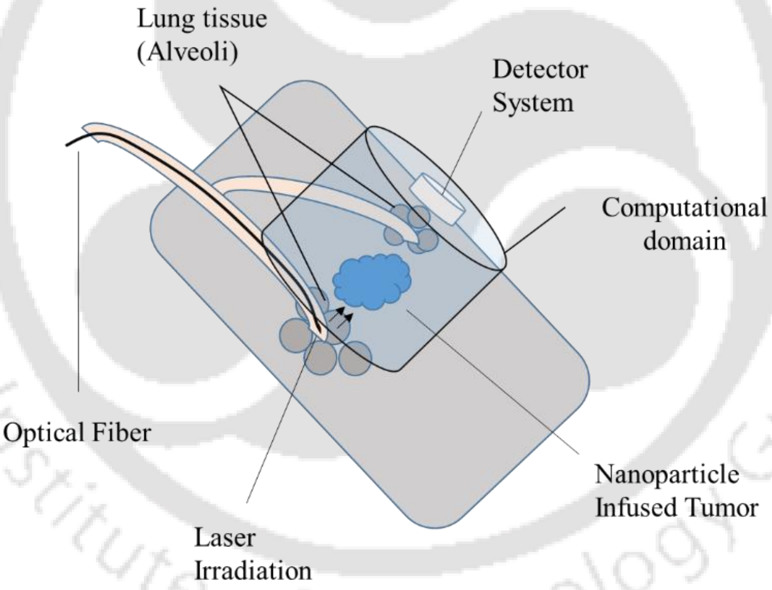

Figure 5.1. Imaginary experimental setup for laser irradiation from inside the lung using optical fiber.

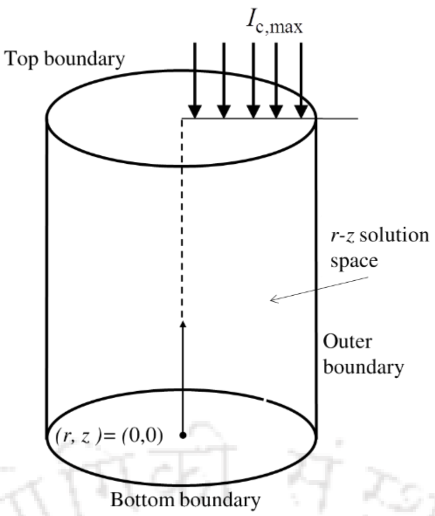

Figure 5.2. Schematic of a 2-D axisymmetric cylindrical tissue.

$$\frac{\partial I_c}{\partial s} = -\beta I_c \tag{5.2}$$

where $\beta\left(=\kappa_a+\sigma_s\right)$ is the extinction coefficient of the medium. The partial attenuation of the collimated intensity along the distance travelled inside the medium is converted into diffuse intensity I_d, and hence, the total intensity I at any point inside the medium is given by: $I = I_c + I_d$.

Substitution of $I = I_c + I_d$ and $\frac{\partial I_c}{\partial s} = -\beta I_c$ from Eq. (5.2) in Eq. (5.1) results in

$$\frac{1}{c}\frac{\partial I_c}{\partial t} + \frac{1}{c}\frac{\partial I_d}{\partial t} + \frac{\partial I_d}{\partial s} = -\beta I_d + S_t \tag{5.3}$$

where the total source term S_t consists of the source term S_c due to collimated intensity and source term S_d due to diffuse intensity. For an isotropically scattering medium, the phase function $\Phi\left(\Omega,\Omega'\right)=1$. The source term due to collimated intensity is given by

$$S_c = \frac{\sigma_s}{4\pi} G_c \tag{5.4}$$

where G_c is the incident radiation due to collimated intensity and is calculated from

$$G_c = I_{c,\max} \exp(-\beta s_c) \times \left[H\left(\beta(ct-z)\right) - H\left(\beta(ct-z) - \beta ct_p\right) \right] \tag{5.5}$$

where $I_{c,\max}$ is the magnitude of the collimated intensity at the top boundary $(z = Z)$ and s_c is the physical distance travelled by the collimated intensity along its direction of incidence. with $\omega(=\sigma_S/\beta)$ as the scattering albedo and G_d as the incident radiation due to diffuse intensity, the source term due to diffuse intensity is given by

$$S_d = k_a I_b + \frac{\sigma_s}{4\pi} G_d = (1-\omega)\beta I_b + \frac{\omega\beta}{4\pi} G_d \tag{5.6}$$

Following the steps of Mishra *et al.* 2014, of the DOM, the G_d is given by

$$G_d = \int_{\Omega=0}^{4\pi} I_d(\theta,\phi)\, d\Omega \approx \sum_{l=1}^{N_\phi} \sum_{k=1}^{N_\theta} I_d^m \Delta\Omega^m \tag{5.7}$$

where N_θ and N_ϕ are the divisions of the polar $(0 \le \theta \le \pi)$ and the azimuthal $(0 \le \phi \le 2\pi)$ space, respectively. In Eq. (5.8), $\Delta\Omega^m$ is the directional weight, and along with the associated direction cosines are computed using

$$\Delta\Omega^m = 2\sin\theta^m \sin\left(\frac{\Delta\theta}{2}\right)\Delta\phi^m \tag{5.8}$$

The time normalization is done as $\zeta = \beta_0 ct$, where β_0 is the reference extinction coefficient and c is the speed of light. At any time ζ, with reference to Fig. 5.2b, while marching from different quadrants, the cell center intensity $I_{d,P}^m$ is given by step scheme, which is omitted from present chapter for brevity and can be found in [Mishra *et al.* 2008, 2013, 2014]. The solution procedure has been discussed in chapter 2.

With intensity distribution known, the non-dimensional transmittance and reflectance are calculated from [Mishra *et al.* 2011]

$$\Psi_T = \frac{q_T(\eta_z = 0)}{q_{c,\max}}, \quad \Psi_R = \frac{q_R(\eta_z = 1)}{q_{c,\max}} \tag{5.9}$$

where, with normal incidence, heat flux $q_{c,\max} = I_{c,\max}$.

Because of the surface properties of the specially designed NPs and the malignant tumor, infused NPs stick around and penetrate inside the tumor. Owing to surface plasmon resonance, NPs such as gold-silica nanoshells alter the optical properties such as the absorption coefficient and the scattering coefficient of the medium. In order to examine application of NP's in tumor detection in a lung, in the present study, a parametric study has been done by considering NP infused tumor inside the lung. Absorption coefficient of tissue infused with NPs is calculated using [Dombrovsky *et al.* 2011, 2012, Changhong *et al.* 2008, 2009].

$$\kappa_a = \kappa_{a,t} + 0.75 f_v \frac{Q_a}{a} \tag{5.10}$$

where Q_a is the dimensionless efficiency factor of absorption for single particle, f_v is the specific volume fraction of the tissue-nanoshells and a is the radius of the nanoshell. The tissue scattering coefficient is calculated from

$$\sigma_s = \sigma_{s,t} + 0.75 f_v \frac{Q_s}{a} \tag{5.11}$$

where Q_s is the dimensionless efficiency factor of scattering of a single nanoshell at wavelength $\lambda = 0.6328 \mu\text{m}$.

5.2. Results and Discussion

The DOM code for pulsed collimated radiation in 2-D cylindrical medium has been first validated with literature [Mishra *et al.* 2008]. By increasing the aspect ratio $AR = 2r/z$ to a high value, e.g., AR =10, the geometry becomes 1-D with variation only along the z-axis of the cylinder. Figure 5.3 (a,b) shows the transmittance and reflectance signals. For AR = 10, results have been compared and validated against the 1-D results of [Mishra *et al.* 2008].

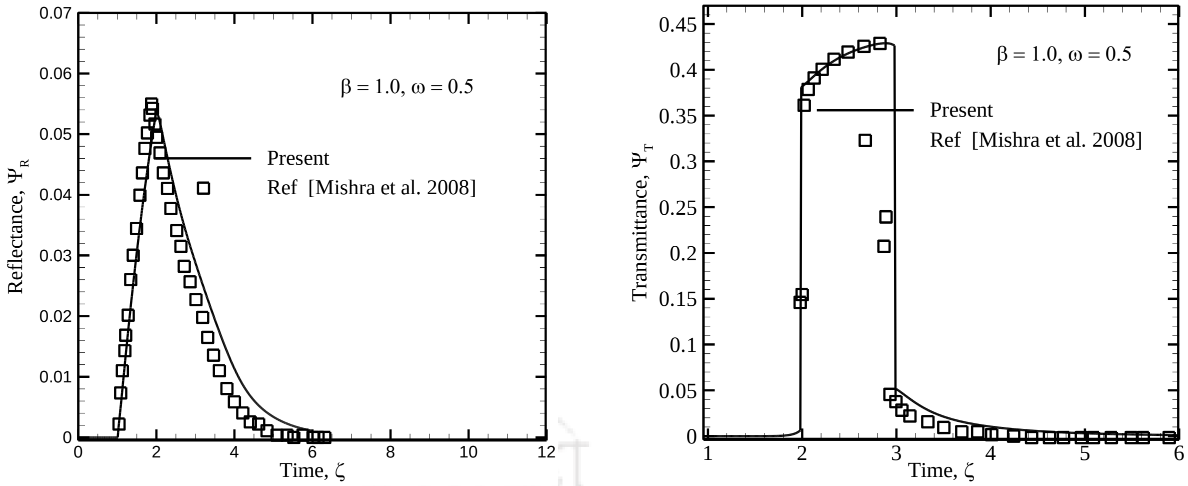

(a) (b)

Figure 5.3. (a) Reflectance and (b) transmittance signals for $\omega = 0.5$, $\beta = 1.0$ and $AR = 10.0$.

With 2-D code validated, for the present work a grid size of 120×80 and 12×12 discrete ray directions were found sufficient.

Pig's lung was taken into consideration, and respiratory optical properties of lung tissue were considered. Lung contains alveoli with surrounding tissue that exhibits absorption coefficient and extinction coefficient as a function of respiration [Beekyx *et al.* 1997]. The lung tissue was divided into four equidistant layers in the z-direction. Whenever the case of tumor was considered, tumor occupied mid 50% of the cylindrical tissue. Four phases of respiratory volumes with corresponding optical properties at laser wavelength of $\lambda = 0.6328\mu m$ were considered [Beekyx *et al.* 1997], as given in Table 5.1. Using Eq. (5.10) and Eq. (5.11), with NP's of radius $a = 20\times10^{-9}$ m, wavelength $\lambda = 0.6328$ µm, efficiency factor of absorption $Q_a = 7.828$, and efficiency factor of scattering $Q_s = 1.144$, optical properties of lung tissue with NP infused tumor for various volume fraction are obtained , and these are given in Table 5.2. The optical properties of tumor in Table 7.2 correspond to tumor without nanoshell infusion.

Table 5.1. Optical properties of Pig's lung tissue for different lung volume at wavelength $\lambda = 0.6328\mu m$.

Lung volume (ml)	**Extinction coefficient β (1/mm)**	**Scattering albedo ω**
25	30.0134	0.9995
50	32.5005	0.9998
100	25.2002	0.9999
150	21.2018	0.9959

Table 5.2. Optical properties of nanoshells infused lung tumor at wavelength $\lambda = 0.6328 \mu m$.

Volume fraction f_v	**Extinction coefficient** β **of tumor** $(\frac{1}{m} \times 10^{-3})$	**Scattering albedo** ω **of tumor**
$f_v = 0.0$	9.50	0.7668
$f_v = 10^{-7}$	9.533	0.7871
$f_v = 10^{-6}$	9.836	0.7668
$f_v = 10^{-5}$	12.864	0.6163

Figure 5.4 shows transmittance signal of a single step pulse laser irradiated healthy lung tissue and lung containing tumor at four stages of respiratory lung volumes. Pulse width of $t_p = 33 \times 10^{-9}$ s was used.

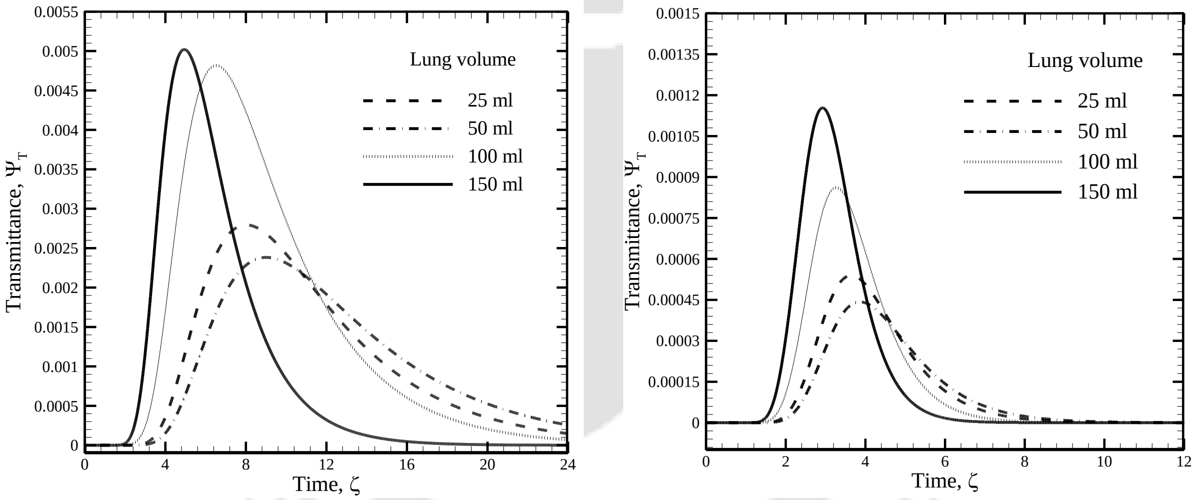

(a) (b)

Figure 5.4. (a) Transmittance signal of laser irradiated (a) healthy lung and (b) lung containing tumor at different stages of respiratory lung volumes.

In case of a tumor present inside the lung, an decrease in transmittance in comparison with healthy lung is observed. Also, as the volume of lung increases, the extinction coefficient decreases, and as observed, this gives rise to a higher value of transmittance.

Figure 5.5 provides a comparison of transmittance signal of a single pulse laser irradiated healthy and cancerous lung containing tumor at two stages of respiratory lung volumes, i.e. 25 ml and 150 ml. It is observed that for a given lung volume, transmittance is much lower when the lung is infected with a tumor.

Figure 5.6 shows a comparison of transmittance signals Ψ_T, of single pulse laser irradiated lung with a tumor infused with NP for two volume fractions of 10^{-5} and 10^{-6} for lung volume levels of 25 ml and 150 ml. For a higher NP volume fraction $f_v = 10^{-5}$, with the maximum lung volume of 150 ml, transmittance signal is a significantly higher as compared to low volume fraction and low lung volumes.

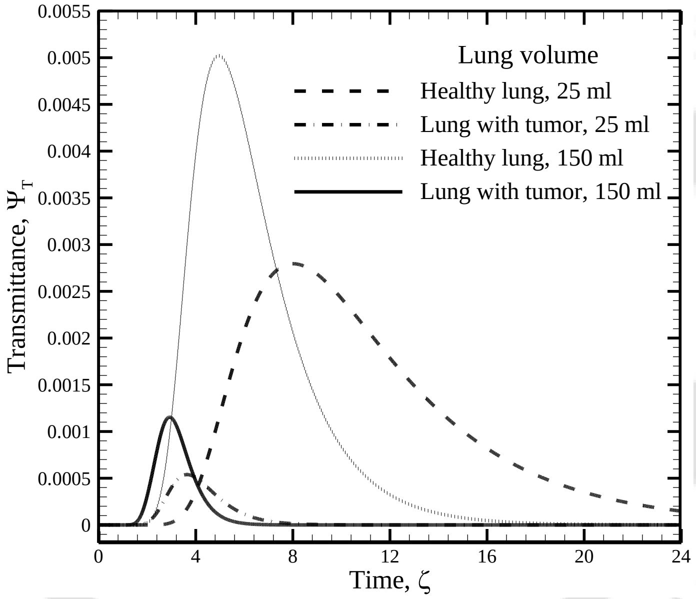

Figure 5.5. Transmittance signal of laser irradiated healthy and cancerous lung at two stages of respiratory lung volumes.

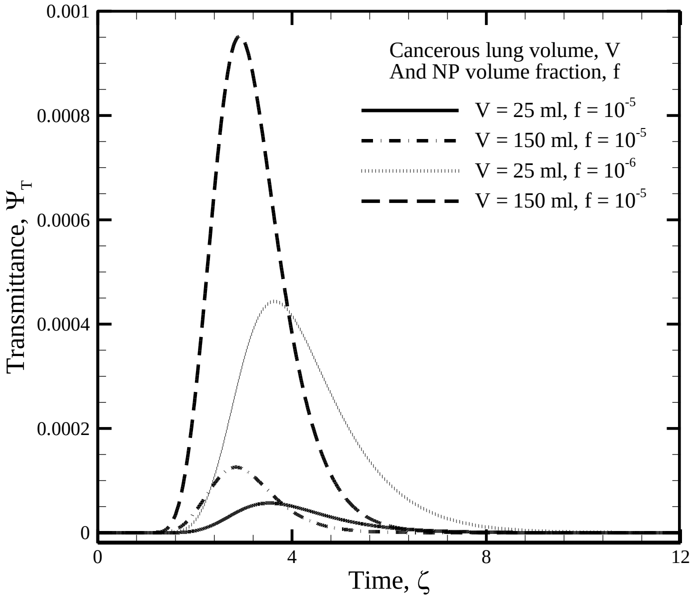

Figure 5.6. Transmittance signals of laser irradiated lung with tumor with nanoparticle volume fractions of 10^{-5} and 10^{-6} at lung volume levels of 25 ml and 150 ml.

Though, the transmittance signals resulting from the irradiation of the tissue with a single laser pulse provides some idea about the tissue-tumor characteristics, to know whether a train of short pulses gives a better picture, next the results are presented for a train of four pulses. With four pulses of same pulse duration $t_p = 33\times10^{-9}$ s as that for the single pulse, and the two consecutive pulses separated by an equal time lag of $4t_p$, Fig. 5.7 shows transmittance signal for a healthy lung and for a lung containing tumor at four stages of respiratory lung volumes. With NP infused tumor inside the lung, Fig. 5.8 shows a comparative transmittance plot for two lung volumes, Fig 5.8a for 25 ml and Fig. 5.8b for 150 ml, respectively.

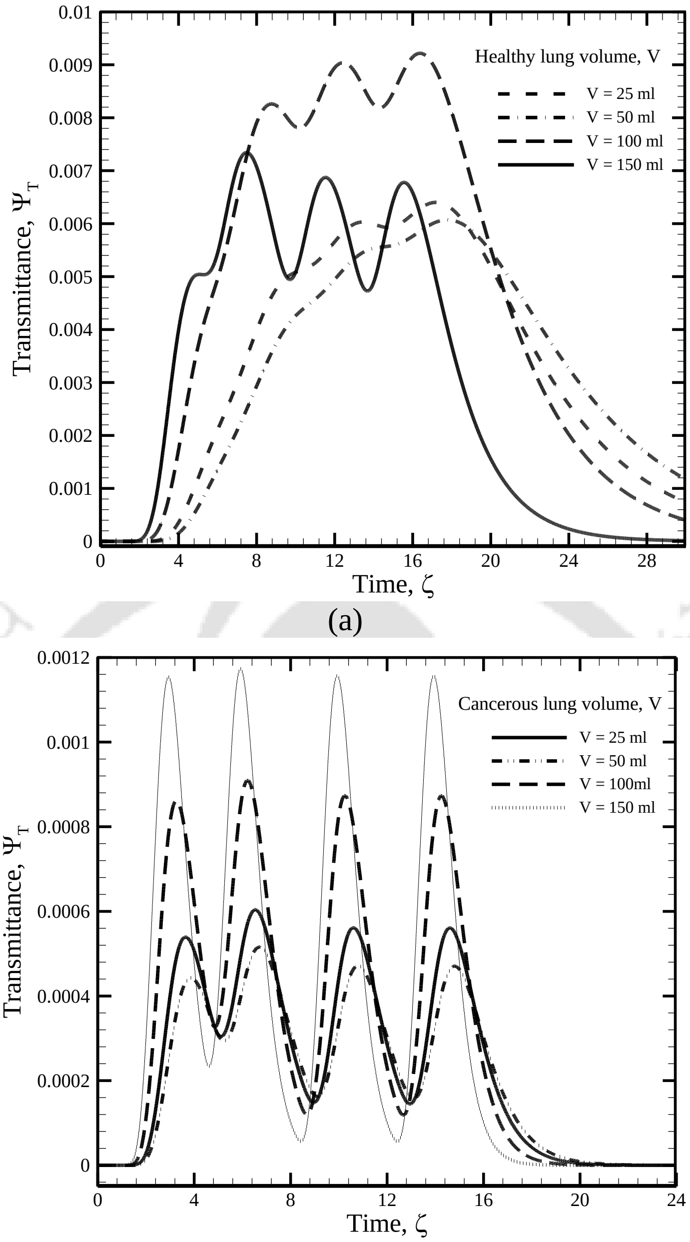

(a)

(b)

Figure 5.7. (a) Transmittance signal of multiple pulse laser irradiated (a) healthy lung and (b) lung containing tumor at different stages of respiratory lung volumes.

While transmitted signals show significant dependence on lung volume and NP volume fraction, reflectance signals (Fig. 5.9), on the other hand, show a less variation. Fig. 5.9. shows reflectance of a multiple (4) pulse laser irradiated lung with NP infused tumor at lung volume levels of 25 ml and 150 ml. Because of very high value of ω associated with biological tissues (Table 5.1 and Table 5.2), the reflectance Ψ_R, is always very high.

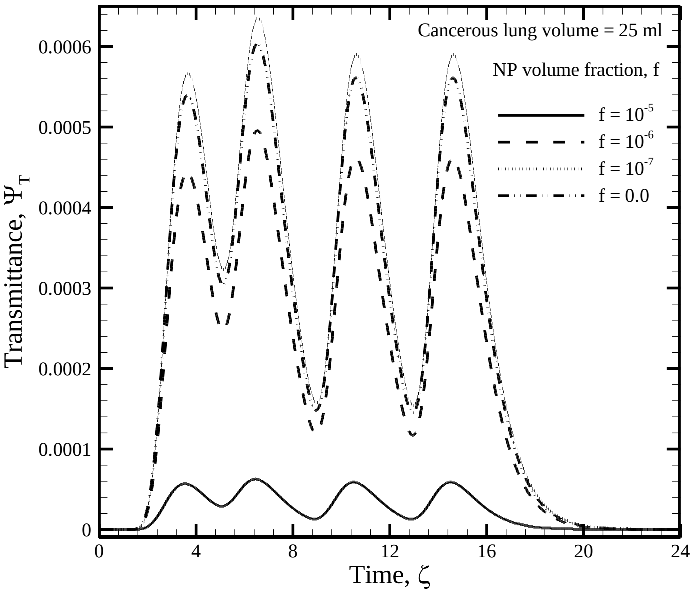

(a)

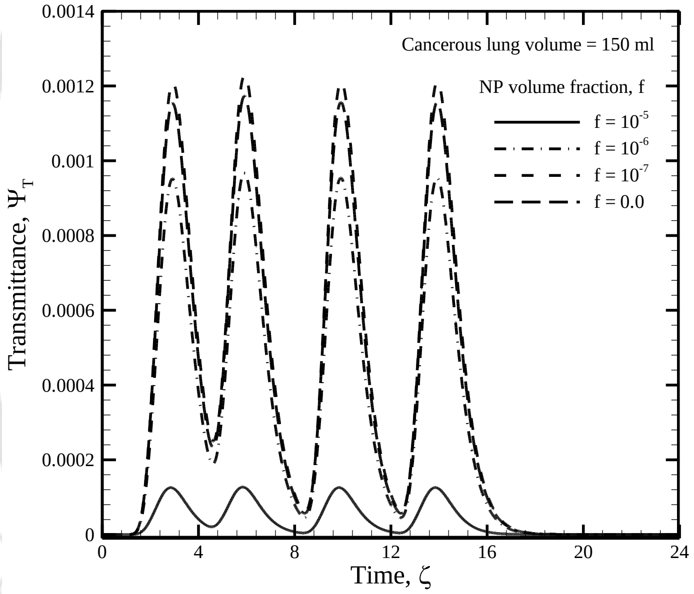

(b)

Figure 5.8. Transmittance signals of multiple pulse laser irradiated lung with tumor with nanoparticle volume fractions of 10^{-5} and 10^{-6} at lung volume levels of (a) 25 ml and (b) 150 ml.

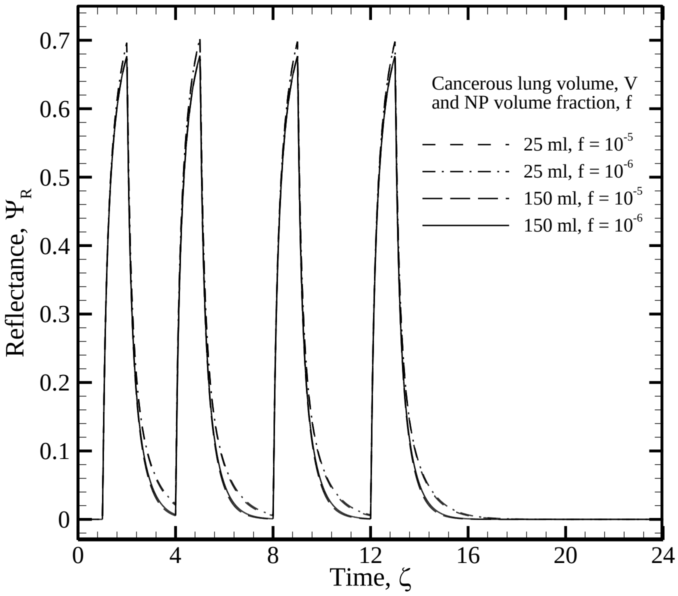

Figure 5.9. Reflectance signal of a multiple pulse laser irradiated lung with NP infused tumor at lung volume levels of 25 ml and 150ml at different NP volume fraction.

Though, the magnitude of reflectance is approximately O(10^3) more than the transmittance, unlike transmittance, reflectance does not show variations with tissue type and lung volume. Hence, the transmittance signal is better suited for diagnostic application.

5.3 Closure

Transport of a $\lambda = 0.6328\ \mu\text{m}$ wavelength short-pulse laser in a 2-D axisymmetric cylindrical pig lung tissue with and without a tumor was studied. The optical properties varied with the respiratory lung volume. Centrally located tumor occupied 50% volume of the lung tissue. Study was also made with and without infusion of gold-silica nanoshells. For the normal incidence, with step temporal profile, the study considered both a single pulse and a train of four pulses. Effects of respiratory lung volume and the volume fraction of gold-silica nanoshells on temporal transmittance and reflectance signals were analyzed. Transmittance signal was more susceptible to changes in lung respiratory volume and the volume fraction of the nanoshells. Though owing to a very high scattering of the tissue, the magnitude of reflectance was more than that of transmittance, it did not vary much with change in lung respiratory volume and the volume fraction of the nanoshells.

Chapter 6

Nanoparticle Assisted Hyperthermia and Thermal Therapy

6.1 Theory

This chapter deals with the study on nanoparticle assisted hyperthermia and thermal therapy. Temporal evolution of temperature in a single nanoparticle infused spherical tissue-tumor geometry subjected to a thermal input is analyzed first. The second study pertains to temperature evolution in a uniformly distributed nanoparticles infused tissue-tumor cylindrical geometry under laser irradiation. In this following, nanoparticles (NPs) and nanoshells have been used interchangeably.

6.1.1 Single nanoparticle infused tissue

Nanoparticle mediated thermal therapy for killing cancer cells is being extensively researched. Because of its selective targeting, local damaging combined with minimal side effects, this mode of treatment is very promising [Roa *et al.* 2011, Letfullin *et al.* 2011]. For ablation of a tumor, spatial-temporal temperature distribution in a tumor imbedded tissue is analyzed. Analysis is done with a gold-silica nanoshell deposited at the tissue tumor interface. The tissue surface is subjected to an external heat input in form of temperature equivalent to that a pulse laser irradiation with Gaussian temporal profile. With a hemispherical tumor seated on a hemispherical tissue, the analysis is done using the FEM based solver, COMSOL. Since for this part of study involving a single nanoparticle, the study is confined only to the conduction heat transfer. Also, while working on COMSOL, it has been observed that the coupled radiation-bioheat modules did not perform well for the study under consideration. Insertion of the nanoparticles improves the localized heating.

Antibody coated NPs is an effective way for the placement of NPs on the surface of the tumor. NPs can be of different shapes and sizes depending upon the desired effects. The NPs on the surface of the tumor provide increased thermal effect when irradiated with laser. Because of the small size of the NPs, the temperature rise is only in the immediate vicinity of the tumor, and this results in the desired localized thermal damage. NPs can be delivered through pulmonary tract via inhalation or by intravenous injections. Inhalable nanoparticles distribution is found to be better than other methods of its administration. Apart from injection, for getting a better reach, optical fibers can also be used to deliver light from inside the lung tissue via the bronchial tubes [Roa *et al.* 2011, Letfullin *et al.* 2011].

A spherical gold-silica nanoshell exhibits exceptional heat generating properties by the phenomenon known as surface-plasmon resonance (SPR). Due to the surface-plasmon resonance, the absorption of nanoshells increase, and the peak absorption appears at a particular wavelength. In a particular range of wavelengths, the peak thermal response is determined from the ratio of the thickness of the gold coating and diameter of the silica core [Roa *et al.* 2011, Letfullin *et al.* 2011].

In the present chapter, effect of gold NPs on spatial-temporal temperature distributions are studied for a hemispherical tumor seated on a hemispherical tissue (Fig. 6.1). The gold-silica nanoshell is provided at the interface of the two hemispheres. The diameter of the nanoshell is 20 nm, and the diameters of the tissue and tumor are 1 µm. Although, these dimensions of tissue/tumor are very small compared to any typical tissue/tumor size (as considered in other chapters of this thesis), in this part of study it is considered for analyzing a short time and localized heating effect of a single nanoparticle. Properties of the tissue and the tumor are constant. The tissue surface is subjected to an external heat input in the form of temperature equivalent to that of a pulse laser irradiation with Gaussian temporal profile. Simulation is done using finite element based commercial solver, COMSOL Multiphysics.

With core body temperature as the boundary condition, for the geometry shown in Fig. 6.1, the governing energy equation is given by

$$\rho c_p \frac{\partial T}{\partial t} = \nabla \cdot \left(k \nabla T \right) + Q + Q_{bio} \tag{6.1}$$

where T, t, k, ρ, c_p, Q and Q_{bio} are the temperature, time, thermal conductivity, density, specific heat of the tissue, distributed volumetric heat source due to spatial heating and metabolic heat generation rate, respectively.

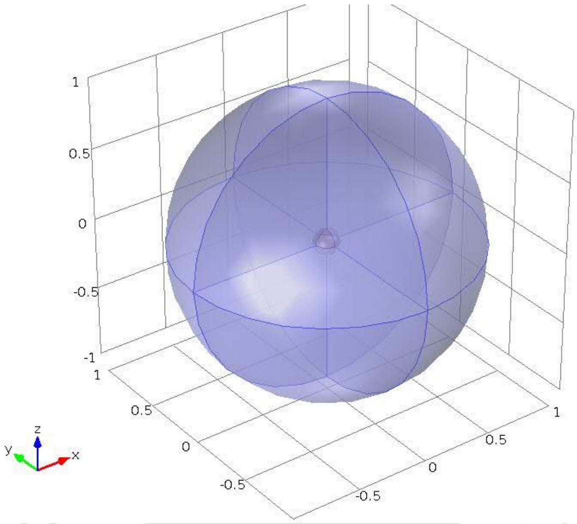

Figure 6.1. Schematic of the 3-D tissue-tumor geometry with a gold-silica nanoshell at the center.

In biomedical applications, short-pulse laser with Gaussian temporal profile in both spatial and temporal domains are used. The Gaussian nature of temperature as a function of time can be expressed as

$$T(t)=\frac{T_{\max}}{\sqrt{2\pi\sigma^2}}e^{-\frac{(t-\mu)^2}{2\sigma^2}} \tag{6.2}$$

where $T_{\max}$ is the maximum input temperature to the model, σ is half of the pulse width, and μ is the mean. The time of temperature input was taken as 4 ms with a step of 0.25 μs. The maximum temperature $T_{\max}$ was taken as 1100 K.

6.1.2 Multiple nanoparticle infused tissue

Next, effect multiple NPs infusion in tissue with large blood vessels is studied. Laser-induced hyperthermia can act as an independent method of treatment for some types of cancers, as well as, it can be used in conjunction with conventional method of cancer treatment such as radiotherapy and chemotherapy [Niemz, 2007; Minkowycz et al, 2009; Welch and Gemert, 2010]. Numerical modelling and simulation of such a procedure provides understanding of thermo-physical behavior of biological systems. Temperature prediction in laser-induced hyperthermia planning is of utmost importance for efficacy of treatment [Das *et al.*, 2003; Fanjul-Vélez *et al.*, 2009].

Many researchers have studied heat transfer analysis in a biological tissue extensively. Several bioheat transfer models have been proposed during the last four decades. Blood perfusion based models such as Pennes bioheat model and the countercurrent bioheat models such as Weinbaum-Jiji bioheat model are some examples. Blood flow in vessels have significant effect on heat transfer in nearby regions in a tissue with embedded countercurrent pairs of large blood vessels of typical diameter < 200 µm. Weinbaum *et al.* (1984), proposed a three layer model for bioheat transfer analysis in tissues geometry with large countercurrent blood vessel pairs. Later, because of complexity associated in modelling a three-layer system, a new simplified Weinbaum-Jiji (WJ) bioheat model was proposed. The WJ model considers the effect of number of countercurrent blood vessel pairs, the blood velocity, and the blood vessel diameter, while predicting temperature field in vascularized biological tissue. Baish *et al.* (1986) presented a comparative study of unidirectional and countercurrent blood flow bioheat models. Later, Song *et al.* (1987) developed a three-layer model using simplified WJ model, and analyzed the effect of vascular geometry on enhancement of effective conductivity.

Laser heating of tissue suffers from some shortcoming such as overheating of nearby healthy tissue causing thermal damage to undesired locations. Recent literature suggests a possible solution using nanoparticle-assisted hyperthermia, for selective and enhanced heating of tissue with minimum damage to healthy tissues. Numerical and experimental studies show the significance and efficacy of nanoparticle assisted thermal therapy and hyperthermia [Day *et al.*, 2009; Dombrovsky *et al.*, 2011]. Selective targeting of cancer tumor and localized heating effect are the two most supporting characteristics of NP assisted cancer treatment.

In a NPs infused tumor, absorption and scattering of laser of a particular wavelength is enhanced using the SPR phenomenon [Liu *et al.*, 2008]. By changing their core-to-shell ratio, these NPs can be tuned to achieve the maximum absorption for a particular wavelength [Das *et al.*, 2003; Fanjul-Vélez *et al.*, 2009]. In the present case, a 20 nm nanoshell is tuned for laser of wavelength 632.8 nm. Effectiveness of nanoshells in a NP assisted thermal therapy and hyperthermia for cancer treatment is well demonstrated in the literature [Vera and Bayazitoglu, 2009a; Vera and Bayazitoglu, 2009b; Dombrovsky *et al.*, 2012; Absalan *et al.*, 2012]. As the biocompatibility of nanoshells are generally considered safe [Loo *et al.*, 2004], in the present study, gold-silica nanoshell is used for simulating laser heating of nanoparticle infused tumor in a vascularized tissue. The use of laser of wavelength 632.8 nm in the current study facilitates the maximum absorption of laser light by the tissue only with embedded NPs, and is mostly transparent to other soft tissues [Liu *et al.*, 2008].

The reported analytical and numerical studies [Weinbaum and Jiji, 1985; Baish *et al.*, 1986; Song *et al.*, 1987] with WJ bioheat model pertain to simple one-dimensional geometry with many simplifying assumptions. Studies on laser assisted hyperthermia in a tissue with large blood vessel pairs subjected to collimated radiation (laser), and its treatment as volumetric radiation in the bioheat equation has not been reported. Also, numerical modelling of nanoparticle assisted laser heating in a tissue with thermally significant countercurrent blood vessel pairs has not been reported in the literature. The present study, therefore, attempts to provide an insight into numerical analysis of NP assisted laser hyperthermia for cancer tumor treatment in a tissue with thermally significant countercurrent blood vessel pairs. Consideration is given to a 2-D axisymmetric cylindrical geometry which serves a close approximation to the realistic scenario.

In the present study, heat transfer in a 2-D cylindrical tissue-tumor geometry (Fig. 6.2) is modelled using the WJ bioheat equation. The tissue is embedded with moderately large blood vessel pairs. The tumor is infused with gold-silica nanoshells. For achieving hyperthermia, tissue temperature is raised by irradiating it with continuous wave (*cw*) laser of wavelength $\lambda = 0.6328\,\mu\text{m}$ [Dombrovsky *et al.* 2012]. Effects of numbers of blood vessel pairs, nanoshell concentration, laser exposure time, beam radius, and power density on temperature spread in the tissue are analyzed.

Figure 6.2(a) shows the schematic of the 2-D axisymmetric cylindrical tissue $\left(r \times z = 10\,\text{mm} \times 15\,\text{mm}\right)$ embedded with a top-seated tumor (10 mm × 5 mm). The top $\left(r, 0\right)$ surface of the tumor is subjected to *cw* laser (Fig. 6.2(b)). Because of the axisymmetric consideration, the computational domain as shown in Fig. 6.2(b) and 6.2(c) is the 2-D $r - z$ plane. The top, right and bottom surfaces of the tissue-tumor geometry are at the core body temperature (37$^{\text{o}}$C). Due to the symmetry, the left boundary of the computational domain is imposed with the symmetry boundary condition. The computational domain consists of two layers - a layer of nanoparticle infused tumor and a muscle tissue layer (soft tissue) (Fig. 6.2(a) and 6.2(b)). A two-layer grid, fine grid for the tumor region and a relatively coarse grid for the tissue region, as shown in Fig. 6.2(c) are considered. In the tissue and the tumor regions, $\Delta r = 1.25 \times 10^{-4}\,\text{m}$ is kept constant (Fig. 6.2(c)). However, in the tumor region

$\Delta z_1 = 1.25\times10^{-4}\,\text{m}$ is smaller than that in the tissue region $\left(\Delta z_2 = 1.875\times10^{-4}\,\text{m}\right)$ (Fig. 6.2(c)). A time step of $\Delta t = 10^{-3}\,\text{sec}$ was found adequate.

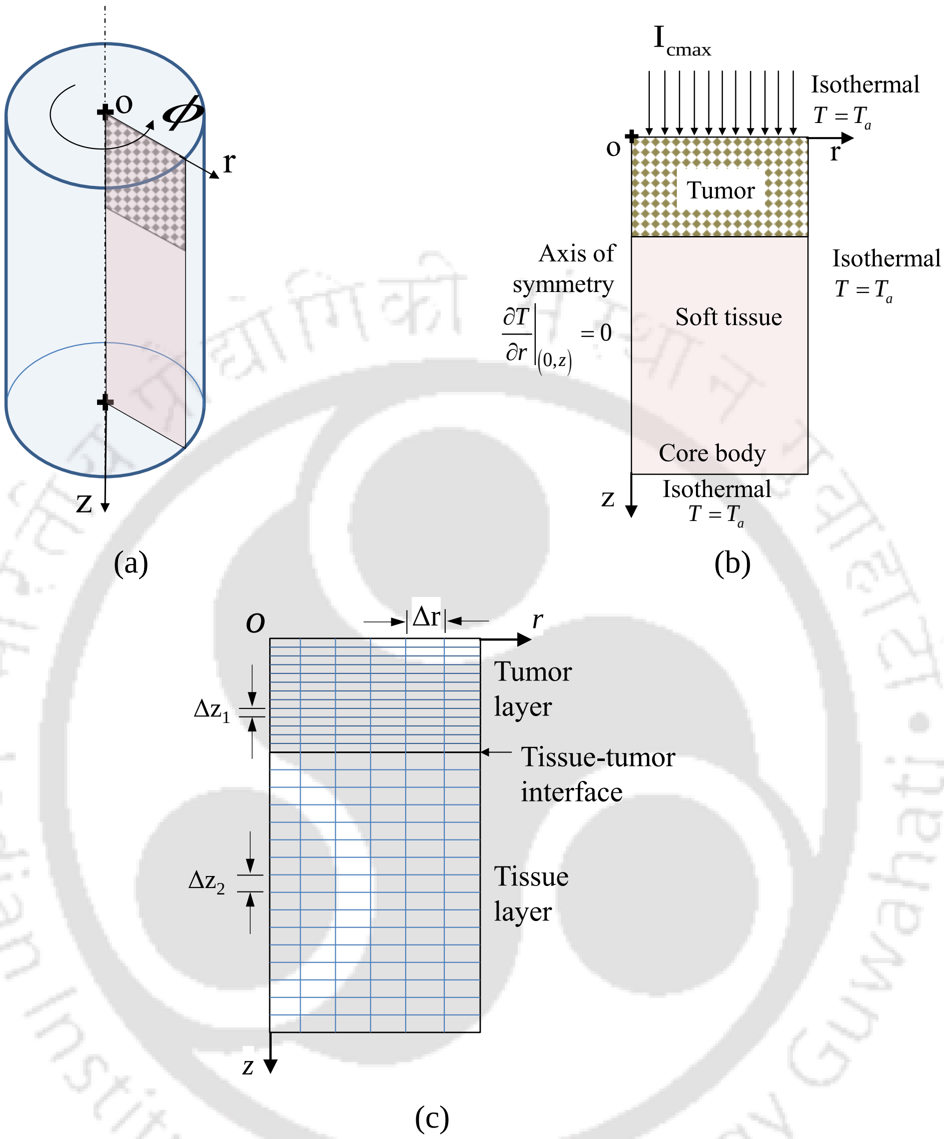

Figure 6.2. Schematics of (a) 2-D cylindrical tissue and (b) $r - z$ computational domain with boundary conditions, and (c) computational grid.

Weinbaum-Jiji bioheat model accounts for incomplete countercurrent heat transfer through artery-vein pair. For a tissue embedded with thermally significant blood vessel pairs Fig. (6.3), WJ model assumes no net mass transfer across the system as amount of blood travelling in opposite direction is roughly the same [Weinbaum and Jiji, 1985]. Figure 6.2 is a typical representation of a small control volume containing couple of artery-vein pairs. However, in the present study, Fig. 6.2 represents the computational geometry in which it is assumed that the artery-vein pairs are arranged parallel to the central axis of the geometry.

For the 2-D cylindrical geometry under consideration (Fig. 6.2a), the WJ model can be expressed as

$$\rho c\frac{\partial T}{\partial t}=\frac{1}{r}\frac{\partial}{\partial r}\left(rk_{eff}\frac{\partial T}{\partial r}\right)+\frac{\partial}{\partial z}\left(k_{eff}\frac{\partial T}{\partial z}\right)+Q_m \tag{6.3}$$

where ρ, c, k_{eff} and Q_m are the density, the specific heat, the effective thermal conductivity and the volumetric metabolic heat generation rate of the tissue, respectively. The effective thermal conductivity of the tissue is a function of different tissue-blood vessel configurations, and is given by [Weinbaum and Jiji, 1985],

$$k_{eff}=k\left[1+\frac{n}{k^2\sigma_{sf}}\left(\pi\rho_b c_b a^2 u\right)^2\right] \tag{6.4}$$

In Eq. (6.4), k, n, ρ_b, c_b, a and u are the thermal conductivity of the tissue, the number of vessel pairs crossing control volume surface per unit area, the density of blood, the specific heat of blood, the vessel radius and the average blood velocity in the counter current vessel pairs, respectively. For two parallel vessels with uniform surface temperature, embedded in a very large medium of tissue, the shape factor σ_{sf} provides the information of resistance to the heat transfer, and is given by [Chato, 1980; Weinbaum and Jiji, 1985],

$$\sigma_{sf}=\frac{\pi}{\cosh^{-1}(l/2a)} \tag{6.5}$$

where l is the center to center spacing between the vessel pairs.

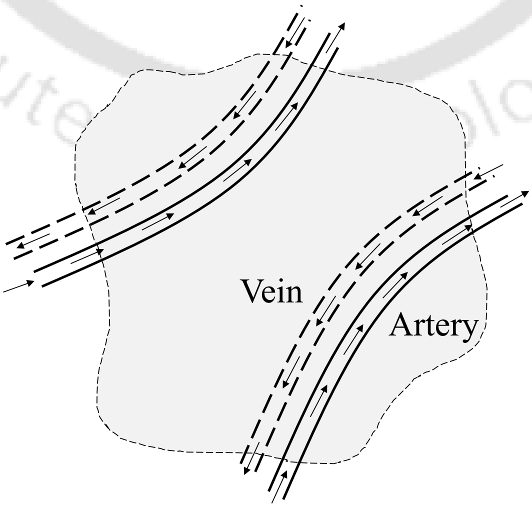

Figure 6.3. Schematic of a tissue containing countercurrent blood vessel pairs.

In the present work, hyperthermia is achieved by irradiating the top $(r,0)$ surface with a *cw* laser. Tissue and tumor being an optically participating medium, the laser penetrates through it. As soon as the laser with intensity I_c comes in contact with the tissue/tumor, it undergoes attenuation. The attenuated component manifests as diffuse radiation, which travels in the $4\pi-$spherical space. In the energy equation, this causes radiation to emerge as a volumetric term, and accordingly the WJ bioheat model gets modified to

$$\rho c\frac{\partial T}{\partial t}=\frac{1}{r}\frac{\partial}{\partial r}\left(rk_{eff}\frac{\partial T}{\partial r}\right)+\frac{\partial}{\partial z}\left(k_{eff}\frac{\partial T}{\partial z}\right)-\nabla\cdot q_r+Q_m \tag{6.6}$$

where $\nabla\cdot q_r$ is the divergence of radiative heat flux, and it is computed using the DOM. The DOM procedure is discussed in chapter 2. The governing bioheat equation (Eq. (6.6)) is solved using the FVM, details of which are presented in chapter 2.

To see the effect of infusion of nano particles on hyperthermia, gold-silica nanoshells are uniformly distributed in the tumor. The change in the optical properties of tumor after nanoshell infusion is calculated using the following equation [Dombrovsky *et al.*, 2012],

$$\kappa_a=\kappa_{a,t}+0.75f_v\frac{Q_a}{a_{ns}} \tag{6.7}$$

where κ_a is the absorption coefficient, Q_a is the dimensionless efficiency factor of absorption for a single particle, a_{ns} is the radius of a single nanoshell and f_v is the specific volume fraction of the tissue-nanoshell. The change in the scattering coefficient is calculated from the following [Dombrovsky *et al.*, 2012],

$$\sigma_s=\sigma_{s,t}+0.75f_v\frac{Q_s}{a_{ns}} \tag{6.8}$$

where Q_s is the dimensionless efficiency factor of scattering for a single nanoshell at wavelength $\lambda=0.6328\mu\text{m}$. Specific heat of blood $c_{p,blood}$ and blood density ρ_{blood} are taken as $3600\ \text{J}\cdot\text{kg}^{-1}\text{K}^{-1}$ and $1060\ \text{kg/m}^3$, respectively. Table 6.2 lists the optical properties of muscle, tumor and nanoparticle infused tumor [Vera and Bayazitoglu, 2009a; Dombrovsky *et al.*, 2012].

Table 6.1: Thermophysical properties of muscle and tumor [Liu *et al.*, 2008].

Thermo-physical properties	Muscle	Tumor
$k\left(\frac{\text{W}}{\text{m/K}}\right)$	0.51	0.558
$\rho_{tissue}\left(\frac{\text{kg}}{\text{m}^3}\right)$	1085	1030
$c_p\left(\frac{\text{J}}{\text{kg/K}}\right)$	3800	3582
$Q_m\left(\frac{\text{W}}{\text{m}^3}\right)$	684.2	9000

Table 6.2: Optical properties of with and without nano-particle infused tumor and muscle [Liu *et al.*, 2008; Day *et al.*, 2009].

Optical properties	Muscle	Tumor	Nano-particle infused tumor
$\kappa_a\,(1/\text{m})$	35	2000	2293.55
$\sigma_s\,(1/\text{m})$	4500	7500	7542.90

6.2 Results and Discussion

6.2.1 Single nanoparticle infused tissue

For the lung tissue and tumor, the temperature distributions at 1.0 ns, 0.25 μs and 40 ms are shown in Figs. 6.4a-c, respectively. For these results, the values of parameters for tissue are: $\rho = 1200\,\text{kg/m}^3$, $c_p = 3300\,\text{J/kg}\cdot\text{K}$, $k = 0.40\,\text{W/m}\cdot\text{K}$. For the tumor, these are $\rho = 1400\,\text{kg/m}^3$, $c_p = 3680\,\text{J/kg}\cdot\text{K}$, $k = 0.55\,\text{W/m}\cdot\text{K}$. It is seen from Figs. 6.4a-c that in the early state (t = 1.0 ns), the temperature rise is sharp and is confined to a narrow region. As the time progresses, temperature comes down, and its spread is more. Because of the thermophysical properties of tumor in upper hemisphere (which is different from the lower hemisphere made of healthy tissue), an asymmetric distribution of temperature field is observed as the time progresses (Fig. 6.4a-c).

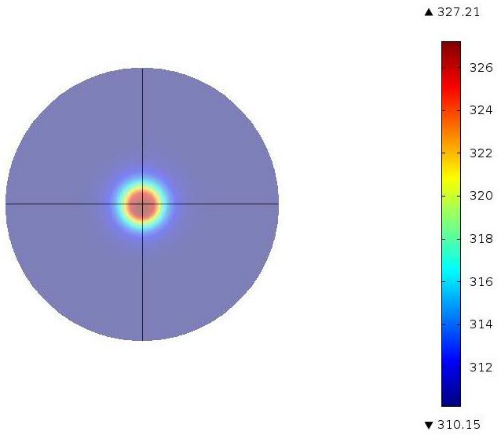

(a) Time = 1.0 ns

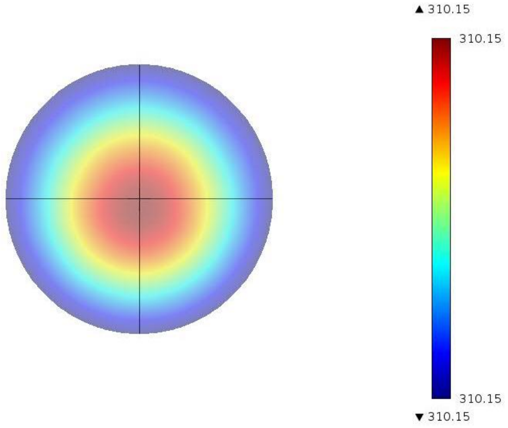

(b) Time = 0.25 μs

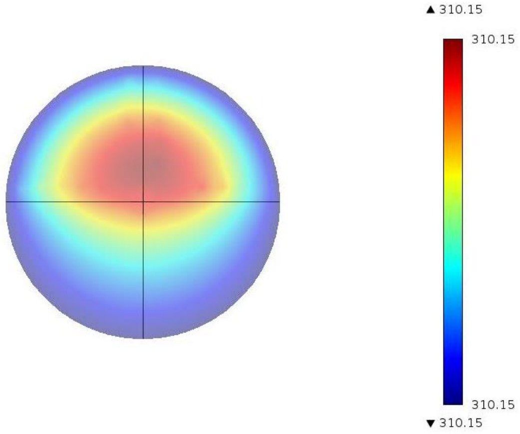

(c) Time = 40 ms

Figure 6.4. Temperature distributions (x-z plane) in the tissue-tumor at (a) 0.0 s, (b) 0.25 μs and (c) 40 ms.

After removal of the input heat pulse, the temperature at the surface of the gold-silica nanoshell is shown in Fig. 6.5. With the passage of time, temperature decreases and it reaches steady-state after 10 µs which is the core body temperature.

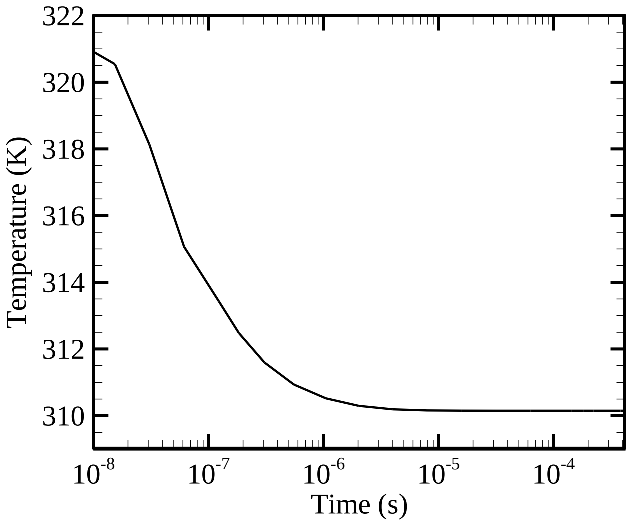

Figure 6.5. Temperature at the surface of nanoshell over time.

6.2.1 Multiple nanoparticle infused tissue

Before presenting results of the present work with the WJ bioheat model with volumetric radiation, first the FVM formulation for solving the WJ bioheat model in the cylindrical geometry without laser incidence is validated (Chapter 4, Section 4.3). Next, for the same geometry, without bioheat equation, the DOM formulation of the laser irradiation is validated against those available in the literature. In order to validate the DOM formulation to calculate the volumetric radiation, for the same geometry (Fig. 6.2a), only the effect of transport of laser irradiation on the top surface is considered.

For two aspect ratios $AR\left(=\dfrac{2R}{Z}\right) = 1$ and 2, distributions of non-dimensional radiative heat fluxes $\Psi_{\mathrm{O}}\left(=\dfrac{q_R}{I_{C,\max}}\right)$ at the outer boundary $\left(R, z^*\right)$ and $\Psi_{\mathrm{T}}\left(=\dfrac{q_{\mathrm{T}}}{I_{C,\max}}\right)$ at the top boundary are obtained using the DOM as shown in Fig 6.6a and 6.6b, respectively. The DOM results compare exceedingly well with those of [Wu and Wu 1997] obtained using the integral equation method.

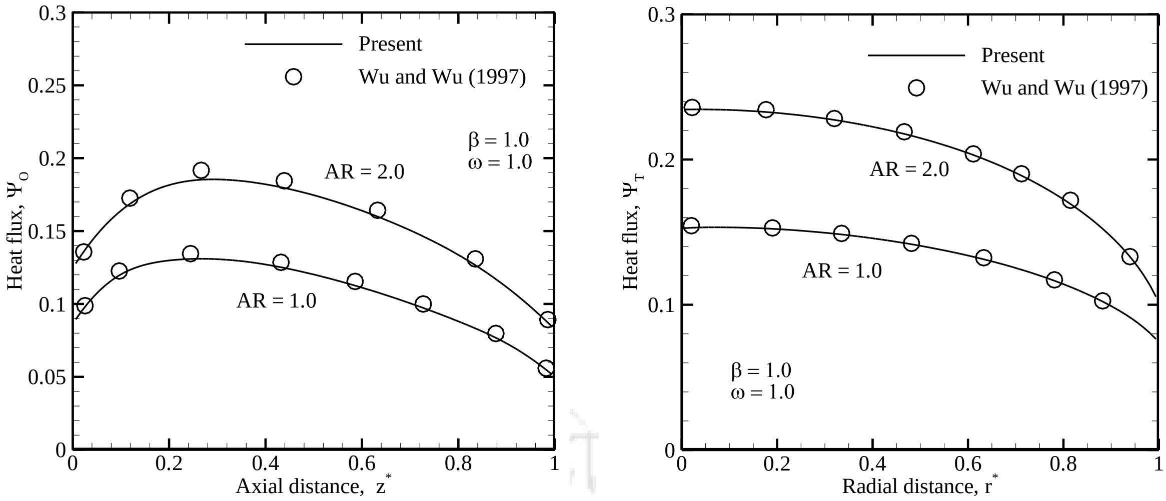

(a) (b)

Figure 6.6. Comparison of non-dimensional radiative heat flux distributions at the (a) outer $(r = R, 0 \le z \le Z)$ and (b) the top $(0 \le r \le R, z = 0)$ boundaries.

Having validated the FVM solver for the governing bioheat equation and the DOM solver for the radiative transfer equation, next the effect of laser irradiation on the nano-particle infused tissue-tumor geometry are presented. The effect has been studied in terms of temporal temperature variations in the tissue. Considering a deep-seated two-layered tissue-tumor geometry as mentioned in the previous section, the tumor is infused with spherical nanoshells with volume fraction $f_v = 10^{-6}$ and particle size of 20 nm. It is assumed that the nanoparticles are of the same size. Having considered the top, the bottom and the outer boundary of the tissue at isothermal core body temperature of 37°C, the effects of presence of nanoshells on absorption and scattering coefficients of tumor are calculated using Eqs. (6.7) and (6.8), respectively. With blood vessel of radius 108.1 μm, the average velocity of blood is taken as 1.413 cm/s. For the solution of the governing equation (Eq. 6.6), the effective thermal conductivity k_{eff} and the shape factor σ_{sf} are calculated using Eqs. (6.4) and (6.5), and the corresponding values are found to be 1.067 and 4.532, respectively, as shown in table 6.3 [Baish *et al.*, 1986].

With an increase in the irradiation time of the laser, the energy accumulation in the tissue increases, and this results in rise in temperature. In Figs. 6.7(a) and 6.7(b), the centerline temperature distributions are shown for different exposure times. In Fig. 6.8 (a), with and without infused nanoshells, temperature distributions are shown for 10s and 20s exposure time. In Fig. 6.8(b), temperature distributions in the nano shells infused tissue are presented at five exposure time levels, viz., 5s, 10s, 20s, 40 s and 50 s. It is to be noted that the temperature in the tissue changes soon after the laser irradiation starts.

An observation of temperature distributions in Fig. 6.7(a) reveals that the temperature change with infusion of nano shells is marginal, and this finding is consistent with that reported in the literature [Dombrovsky *et al.*, 2012]. With a higher exposure time, throughout the tumor region, the temperature rise is more (Fig. 6.7(b)). The peak temperature in all cases appears at $\approx 0.4\ \mathrm{mm}$ from the top surface. For the chosen laser power 0.37 W and the beam radius 2 mm, it is evident from the results that even with 50 s exposure time, only a small region of the tumor attain hyperthermia temperature 43°C and above. This is further evident from the temperature contour for exposure time 50 s shown in Fig. 6.9.

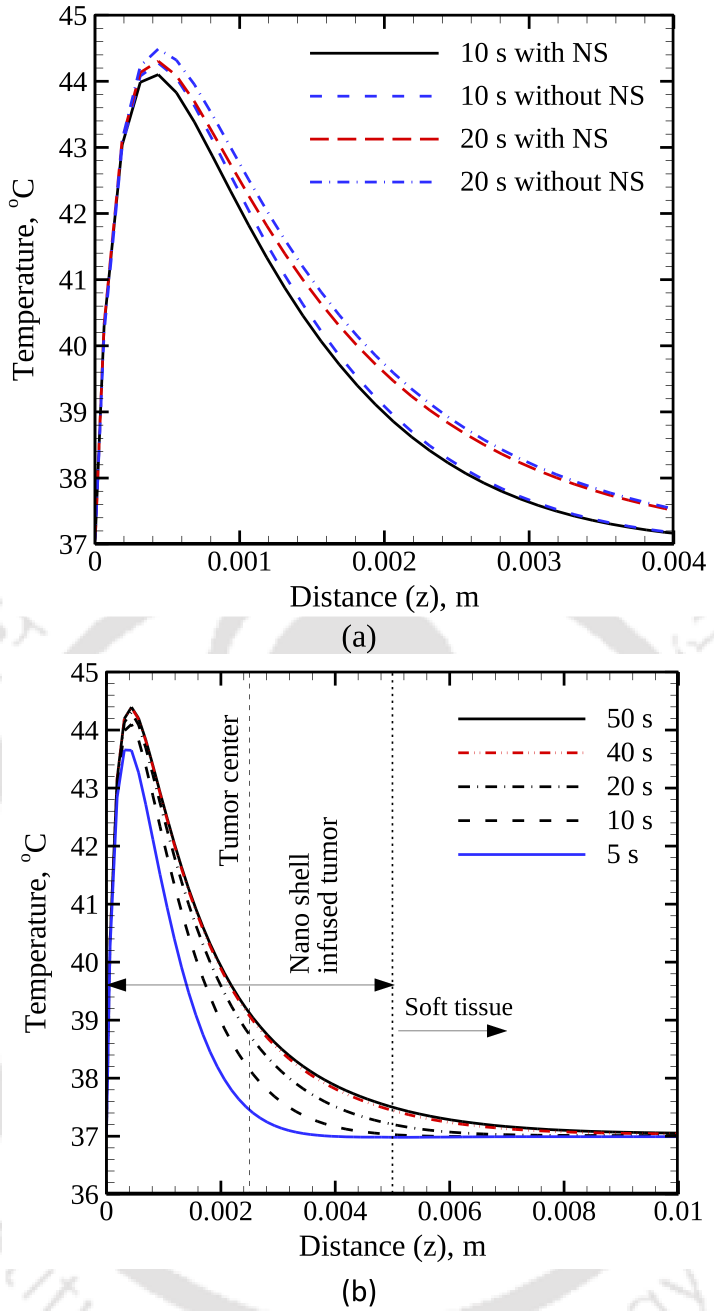

Figure 6.7. Centerline temperature distributions $T(0,z)$ inside the tumor (a) with and without nano shells infusion and (b) with nano shells infusion; laser power: 0.37 W and beam radius 2 mm.

For a tumor, the value of extinction coefficient $\beta\left(=\kappa_a+\sigma_s\right)$ is nearly two times higher than that of a normal muscle tissue (Table 6.2). For any extinction coefficient (β), with increase in axial distance (z), heat flux first increases and it reaches the maximum and then continuously decreases towards the bottom end [Mishra *et al.*, 2014].

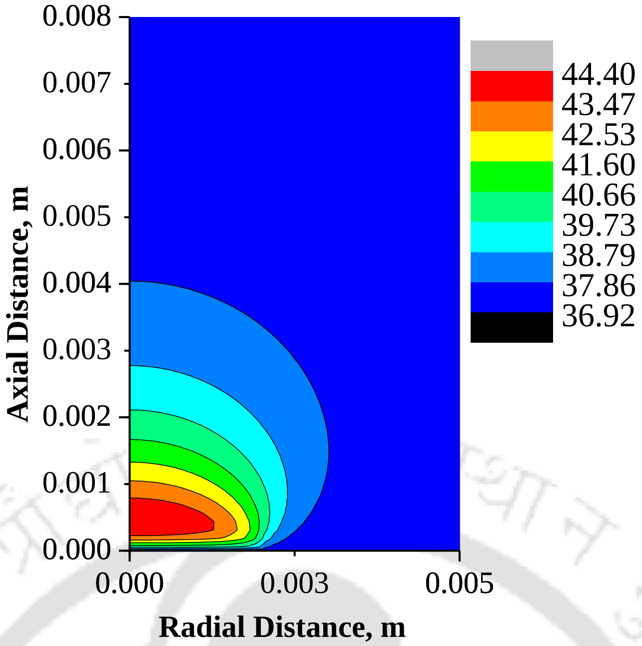

Figure 6.8. Temperature contour of the tissue-tumor geometry at time t = 50 s for a power of 0.37 W and 2 mm beam radius.

Due to higher concentration of the diffuse radiation at the vicinity of the top boundary of the cylindrical tissue, the above trend has been observed. This increase in radiative heat flux manifests in the total heat flux of the system; which is the summation of radiative heat flux and the conductive heat flux of the tissue. It causes the shifting of the temperature peak inside the tissue from the top surface.

With the fixed laser bream radius (2 mm) and exposure time 50 s, for the problem under consideration, the effect of laser power on tumor center (0, 2.5) temperature variation with time is shown in Fig. 6.9a. It is observed that, with laser power 0.25 W and 0.37 W, with beam radius 2 mm, the tumor center temperature is well below the hyperthermia temperature. Considering 45°C as the safe upper limit for long duration hyperthermia treatment, care has been taken not to raise the temperature above the said value. Going by the trend of Fig. 6.7a, the temperature of tumor falls towards the tumor center in the axial direction, and if the maximum temperature at the center of the tumor exceeds the safe limit of 45°C, the temperature at the top region of tumor will go beyond the 45°C limit. However, for a beam radius of 2 mm, with a high power laser (1 W or 2 W), this temperature is attained in about 10 s, and beyond that, the temperature crosses the safe limit (45°C) of hyperthermia treatment. To stay in this limit, attention is given to the laser with power 0.37 W with beam radius 2 mm, and exposure time 50 s.

The attainment of temperature depends on the laser power density and the duration of laser exposer. With 0.37 W laser power and 2 mm beam radius, the power density comes out to be 29443.66 W/m^2. To study the effect of power density or in other words, the beam radius, results of the parametric study for different beam radius are shown in Fig. 6.9b. With laser exposure, time 10 s, these temperature distributions are also shown at 10 s. It is observed from these results that for 0.37 W laser, beam radius 2 mm is the most appropriate as it provides hyperthermia temperature in the top 25% region of the tumor.

Table 6.3: WJ bioheat parameters in a deep tissue layer [Song *et al.*, 1987].

Number density a, pairs/cm^2	**Radius of blood vessel** r, cm	**Blood velocity at Pe = 60** cm/s	k_{eff}/k
1	150	2.5	1.220
2.222	108.1	1.413	1.067

The temperature rise in a laser irradiated vascularized tissue depends on blood flow rate which in turn depends on the diameter of the blood vessel. To study this effect, blood vessel of radii of 108.1 μm and 150 μm are considered. The average blood velocities for vessel radii 108.1 μm and 150 μm are 1.413 cm/s and 2.5 cm/s, respectively (Table 6.3). For radius 150 μm, the effective thermal conductivity k_{eff} and the shape factor σ_{sf} based on Eqs. (6.4) and (6.5) are 1.220 and 4.532, respectively (Table 6.3). The centerline temperature distributions for the blood vessels of radius 108.1 μm and 150 μm, are shown in Fig. 6.10(a) for 5 s and 10 s exposure times. It is observed that with exposure time fixed, higher is the blood vessel diameter, more is the temperature rise in the tissue. This temperature rise is attributed to the transport of higher amount of heat owing to the increased effective thermal conductivity k_{eff} of the tissue.

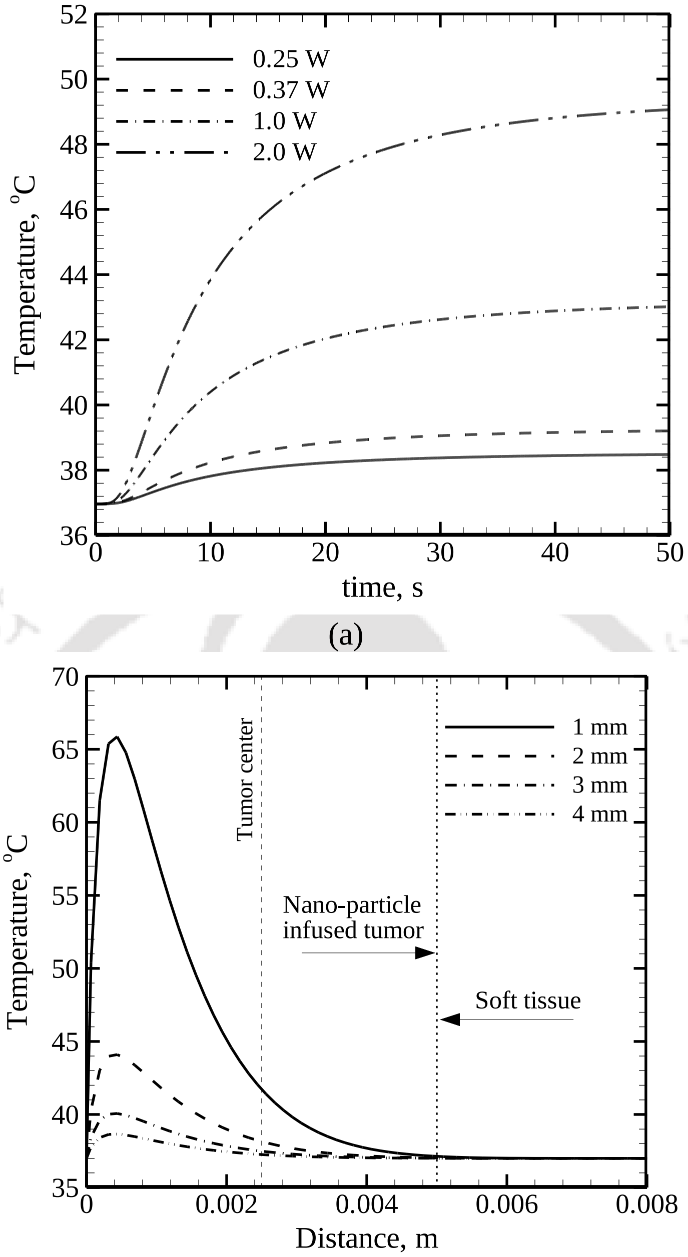

(a)

(b)

Figure 6.9. (a) Effect of laser power on temperature variation with time at the center of the tumor; beam radius 2 mm, and (b) effect of beam radius on the centerline temperature distribution at t =10 s; laser power 0.37 W.

Infusion of the nanoshells in the tumor is known to affect temperature during the laser irradiation. To study this effect, temperature distributions are studied for 10^{-5} and 10^{-7} volume fractions $\left(f_v\right)$ of the nanoshells in the tumor. For the laser power of 0.37 W with a beam radius of 2 mm, Fig. 6.10(b) shows the temperature distribution inside the tissue for exposer time 5 s and 20 s. It has been observed that with increase in the volume fraction of the nanoshells, temperature inside the tissue domain decreases.

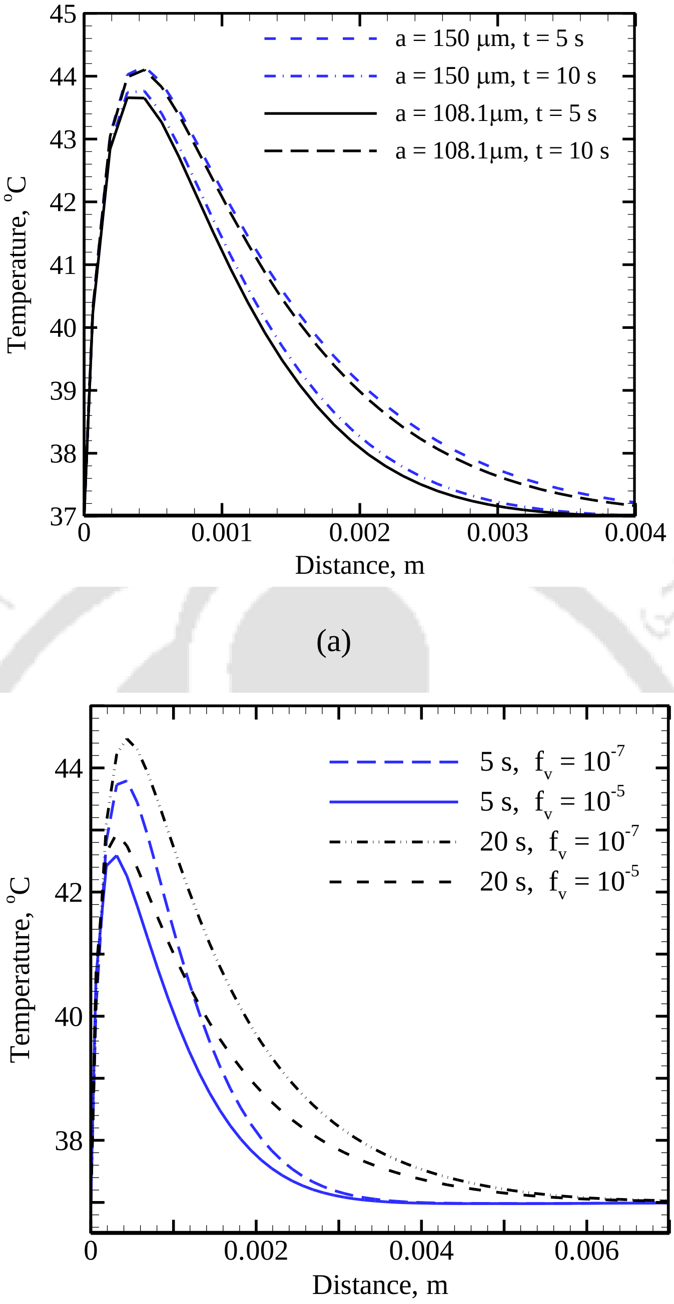

(a)

(b)

Figure 6.10. Centerline temperature distributions $T(0,z)$ inside the tumor (a) with different blood vessel radius and (b) with different nano shells volume fraction; laser power: 0.37 W and beam radius 2 mm.

Calculations of optical properties of nanoshells infused tumor are based on [Dombrosky et al. 2012]. Although, the heating strategies used are different, the results obtained are similar in nature, but they are not the same. The marginal and reverse effect of nanoshell volume fraction in the case of direct heating needs further investigation.

6.3 Closure

In the first part of study, the temporal temperature distribution in a tissue-tumor assembly with gold-silica nanoshell at the interface was studied. The nanoshell was subjected to a pulse heat input. Initially, the temperature rise was high in the narrow region, and with the passage of time (in 40 ms), it spread to a wider region in the tumor. The second part of this chapter dealt with examination of the effectiveness of laser induced hyperthermia treatment of a vascularized tissue with an embedded nanoshell infused tumor. A 2-D axisymmetric cylindrical tissue-tumor geometry was considered with the top surface irradiated with continuous wave laser of wavelength 632.8 nm. For modeling heat transfer in a tissue embedded with moderate sized blood vessel pairs, Weinbaum-Jiji bioheat model was considered. With radiative transfer equation used for modeling of laser transport inside the tissue, the combined conduction-radiation governing equation was solved using the discrete ordinate method and the finite volume method. Effects of laser power, beam radius, blood vessel diameter and nanoshells volume fraction on temperature distributions were studied. A tumor with low nanoshell volume fraction under laser irradiation shows higher temperature distribution, whereas the reverse is true for high volume fraction of the nanoshells. A laser power of 0.37 W was found optimum for a beam of radius 2 mm, for application in a tissue embedded with blood vessel pairs. Temperature distribution suitable for hyperthermia was better achieved using low volume fraction $\left(f_v = 10^{-7}\right)$ of nanoshells with a laser power of 0.37 W applied over 2 mm beam radius. The preliminary numerical study presented here will make a basis for understanding of the mechanism of nanoparticle mediated hyperthermia treatment of vascularized tissue.

Chapter 7

Conclusions and Future Work

7.1 Conclusions

Detection and treatment of cancer using laser continue to remain an active area of research. Laser induced hyperthermia is one such applications of laser in medicine. Studies contained in this thesis pertain to different aspects of laser induced hyperthermia, thermal therapy and laser – tissue interaction. Laser induced hyperthermia for treatment of diseases like cancerous tumor is proving to be an alternative/supplementary mode of treatment. However, it suffers from non-selective tissue damage and overheating of undesired areas. Taking these concerns into account, the present work has aimed at minimizing the skin surface thermal damage and selective targeting of tumor. A study on transmittance and reflectance signal analysis was also performed for characterization of the tumor, and for better understanding of laser – tissue interaction.

Laser induced hyperthermia in one-dimensional planar and two-dimensional axisymmetric tissues was studied first. To minimize the skin surface damage, a surface cooling mechanism using sapphire optical window was adopted, and its performance was compared with direct convective cooling of the skin during laser irradiation. Using the contact cooling mechanism, instead on the skin surface, the maximum temperature was obtained at the desired location deep inside the tissue. The radiation element method with ray emission model was used for modelling light transport and absorption in the tissue. The finite volume method (FVM) was used to solve the governing bioheat equation.

To account for more general cases including transport of laser in an optically participating medium like a tissue, a discrete ordinate method (DOM) based solver for solving radiative transfer equation was developed. Before using the solver for the biological applications, it was validated by solving a benchmark radiative heat transfer problem dealing with 2-D axisymmetric cylindrical participating medium under the influence of collimated radiation. Parametric study in terms of effects of aspect ratio, extinction coefficient and scattering albedo on variations of heat flux and incident radiation along different boundaries were analysed. For all test cases, a very good agreement was found with the results available in the literature.

Using the DOM solver, the study was further extended to different aspects of skin surface cooling during laser induced hyperthermia and thermal therapy. The effect of convective surface cooling on a laser irradiated biological tissue was studied. A coupled bioheat conduction – radiation equation pertaining to a 2-D cylindrical tissue was solved. With volumetric radiative information needed in the bioheat equation computed using the DOM, the FVM was used to solve the bioheat equation. In the absence of any surface cooling mechanism, the maximum temperature was at the skin surface, and not inside the tissue, the desired location. Instead of the tumor, the skin had the undesirable temperature rise. To overcome the problem, a forced convective cooling with a very high value $\left(h = 800\,\mathrm{W\cdot m^{-2}\cdot K^{-1}}\right)$ of the heat transfer coefficient on the skin surface was used, and with this, the desired ablation temperature inside the tissue was obtained, and thermal damage of the skin surface could be prevented.

Convective cooling of the skin surface with a fluid with heat transfer coefficient $h = 800\,\mathrm{W\cdot m^{-2}\cdot K^{-1}}$ cannot be achieved without an active cooling mechanism. To achieve the corresponding extent of skin cooling, the next study utilized optical window contact cooling and cryogenic spray cooling during laser induced hyperthermia. The study was made with sapphire as the contact cooling material. A multilayer tissue with blood perfused skin and vascularized deep tissue was considered, and a two-equation system, namely, the Pennes bioheat equation for blood perfused tissue and Weinbaum-Jiji bioheat equation for tissue with embedded large blood vessel pairs, were solved using the FVM. The radiative information needed in the bioheat equations was computed using the DOM. Maximum temperature inside the tissue was achieved when sapphire contact cooling were used.

Although sapphire is the most popular optical window, the next study pertained to assess the performance of less explored optical windows, viz., yttrium aluminium garnet (YAG), lithium tantalate ($LiTaO_3$), and magnesium oxide doped lithium niobate ($MgO{:}LiNbO_3$). With these four optical windows, the study was also made for two different cryogens having low global warming potential viz. R1234yf and liquid CO_2. A dynamic heat transfer coefficient relation was used for cryogen spray cooling. The combination of liquid CO_2 and yttrium aluminium garnet was found to be more effective for short duration laser exposure hyperthermia procedures.

Nanoparticles have found extensive applications in science and engineering including medicine. Aimed at selective targeting of the tumor, the next study focused on nanoparticle assisted hyperthermia and thermal therapy. The temporal temperature distribution in a tissue-tumor assembly with a single gold-silica nanoshell was studied. The nanoshell was subjected to a pulse heat input, and the temperature distribution at very short time levels were studied. Next, the effectiveness of laser induced hyperthermia treatment of a vascularized tissue with an embedded nanoshell infused tumor was studied. A 2-D axisymmetric cylindrical tissue-tumor geometry was considered with the top surface irradiated with continuous wave laser of wavelength 632.8 nm. For modeling heat transfer in a tissue embedded with moderate size blood vessel pairs, Weinbaum-Jiji bioheat model was considered. With radiative information computed using the DOM, the Weinbaum-Jiji bioheat equation was solved using the FVM.

Effects of laser power, beam radius, blood vessel diameter and nanoshells volume fraction on temperature distributions were studied. A tumor with low nanoshell volume fraction under laser irradiation showed higher temperature distribution, whereas the reverse was found true for high volume fraction of the nanoshells. Temperature distribution suitable for hyperthermia was better achieved using low volume fraction of nanoshells. After conducting the numerical study for understanding the mechanism of nanoparticle mediated hyperthermia treatment of vascularized tissue, the study was further extended for transmittance and reflectance analysis of laser irradiated tissue.

Transport of short-pulse laser in a 2-D axisymmetric cylindrical lung tissue with and without a tumor was studied with the optical properties being a function of the respiratory lung volumes. Tumor was located in the center of the tissue geometry and occupied 50% volume of the lung tissue. Study was made for optical signals from the laser irradiated tissue, with and without infusion of gold-silica nanoshells. For the normal incidence, with step temporal profile, the study considered both a single pulse and a train of four pulses. Effects of respiratory lung volume and the volume fraction of gold-silica nanoshells on temporal transmittance and reflectance signals were analyzed. Transmittance signal was more susceptible to changes in lung respiratory volume and the volume fraction of the nanoshells.

In summary, the studies contained in this thesis provide useful insight on laser-tissue interaction, in particular on laser induced hyperthermia with and without optical windows contact cooling surfaces, cryogens and nanoparticles.

7.2 Future Work

The study presented in the present thesis can be extended to varied domains. To achieve better cancer detection and treatment methods, much research has to be done. The present study used parallel beam of light (laser) for all the simulations. The study can be extended to focused beam laser induced hyperthermia and thermal therapy for deep tissue penetration. In all analyses, in Pennes bioheat equation and Weinbaum-Jiji bioheat equation, the conduction heat transfer was based on Fourier's law of heat conduction. In a short-duration study in a biological tissue, a better insight could be obtained with thermal wave and dual-phase lag models. This study could be performed with and without infusion of nanoparticles. Numerical predictions become more meaningful when experimentally verified. For all the cases presented in this thesis, *in-vitro* as well *in-vivo* studies can be performed.

References

1. Afrin N., Zhang Y., Chen J.K., Thermal lagging in living biological tissue based on nonequilibrium heat transfer between tissue, arterial and venous bloods, *Int J Heat Mass Tran*, 54 (2011) 2419–2426.

2. Aguilar G., Wang G. X., Nelson J. S., Effect of spurt duration on the heat transfer dynamics during cryogen spray cooling *Phys. Med. Biol.* 48 (2003) 2169-2181.

3. Ahmadikia H., Fazlali R. and Moradi A., Analytical solution of the parabolic and hyperbolic heat transfer equations with constant and transient heat flux conditions on skin tissue, *International Communications in Heat and Mass Transfer* 39 (2012) 121–130.

4. Ahmed E. M., Barrera F. J., Early E. A., Denton M. L., Clark C. D., Sardar D. K., Maxwell's equations-based dynamic laser–tissue interaction model, *Comput Biol Med*, 43 (2013) 2278–2286.

5. Altshuler G. B, Zenzie H. H., Erofeev A. V., Smirnov M. Z., Anderson R. R. and Dierickx C., Contact cooling of the skin, *Phys. Med. Biol.* 44 (1999) 1003–1023.

6. Anand S., Sujatha N., Narayanamurthy V. B., Seshadri V., Poddar R., Diffuse reflectance spectroscopy for monitoring diabetic foot ulcer – A pilot study, *Optics and Lasers in Engineering*, 53 (2014) 1–5.

7. Ansari M. A., Massudi R., Study of light propagation in Asian and Caucasian skins by means of the boundary element method, *Optics and Lasers in Engineering*, 47 (2009) 965–970.

8. Antaki P. J., New Interpretation of Non-Fourier Heat Conduction in Processed Meat, *J Heat Transf*, ASME, 127 (2005)189-193.

9. Anvari B., Milner T. E., Tanenbaum B. S. and Nelson J. S., A comparative study of human skin thermal response to sapphire contact and cryogen spray cooling, *IEEE Trans Biomed Eng*, 45 (1998) 934–41.

10. Anvari B., Milner T. E., Tanenbaum B. S., Kimel S., Svaasand L. O. and Nelson J. S., A theoretical study of the thermal response of skin to cryogen cooling and pulsed laser irradiation: implications for the treatment of port wine stain, *Phys. Med. Biol.* 40 (1995b) 1451–65.

11. Anvari B., Milner T. E., Tanenbaum B. S., Kimel S., Svaasand L. O. and Nelson J. S., Selective cooling of biological tissues: application for thermally mediated therapeutic procedures, *Phys Med Biol*, 40 (1995a) 241–52.

12. Baburić M., Duić N., Raulot A. and Coelho P. J., Application of the conservative discrete transfer radiation method to a furnace with complex geometry, *Numer. Heat Transfer A*, vol. 48 (2005) 297-313.

13. Barun V.V. and Ivanov A.P., Thermal action of a short light pulse on biological tissues, *Int J Heat Mass Tran* 46 (2003) 3243–3254.

14. Bashkatov A. N., Genina E. A., Kochubey V. I. and Tuchin V. V., Optical properties of human skin, subcutaneous and mucous tissues in the wavelength range from 400 to 2000nm, *J Phys D Appl Phy*, 38 (2005) 2543–2555.

15. Bayazitoglu Y., Kheradmand S., Tullius T. K., An overview of nanoparticle assisted laser therapy, *Int. J. Heat Mass Transfer*, 67 (2013) 469-486.

16. Becker S. M., One-Dimensional Transient Heat Conduction in Composite Living Perfuse Tissue, *J Heat Transf T-ASME*, 135- 7 (2013) 71002-1-11.

17. Beekyx J. F., van Staverenz H. J., Posthumusy P., Sterenborgy H. J. C. M., van Gemerty M. J. C. The optical properties of lung as a function of respiration, *Phys Med.Biol*, 42(11) (1997) 2263–2272.

18. Bhowmik A., Repaka R., Mishra S. C., Mitra K., Analysis of radiative signals from normal and malignant human skins subjected to a short-pulse laser, *Int J Heat Mass Transfer*, 68 (2014) 278–294.

19. Bhowmik, A., Singh, R., Repaka, R., Mishra, S.C., Conventional and newly developed bioheat transport models in vascularized tissues: A review, *J Therm Biol*, 38 (2013) 107–125.

20. Borjini M. N., Farhat H. and Radhouani M.S., Analysis of radiative heat transfer in a partitioned idealized furnace, *Numer. Heat Transfer A*, 44 (2003) 199-218.

21. Borjini M. N., Guedri K. and Saïd R., Modeling of radiative heat transfer in 3-D complex boiler with non-gray sooting media, *J. Quant. Spectrosc. Radiant. Transfer*, 105 (2007) 167–179.

22. Boulanger J., Akel A. E., Charette A., Liu F., Direct imaging of turbid media using long-time back-scattered photons, a numerical study, *Int J Therm Sci*, 45 (2005) 537–552.

23. Chai J. C., Lee H. S. and Patankar S. V., Ray effect and false scattering in the discrete ordinates method, *Numer. Heat Transfer, B*, 24 (1993) 373-389.

24. Chai J.C. and Patankar S.V., Finite volume method for radiation heat transfer *Adv. Numer. Heat Transfer*, 2 (2000) 110–135.

25. Chandrasekhar S., Radiative Transfer, Dover Publications, New York, 1960.

26. Charny C. K., Cho Y. I., Mathematical Models of Bioheat Transfer, Bioengineering Heat transfer, Advances in Heat Transfer, 22 (1992) Academic press.

27. Chato J C 1980 Heat transfer to blood vessels *J Biomech Eng-T ASME* 102 110-118.

28. Chato J.C., Cho Y. I., A view of History of Heat transfer in Bioengineering, Bioengineering Heat transfer, Advances in Heat Transfer, 22 (1992) Academic press.

29. Cheng T. Y. and Herman C., Analysis of skin cooling for quantitative dynamic infrared imaging of near-surface lesions, *International Journal of Thermal Sciences,* 86 (2014) 175-188.

30. Cheong W., Prahl S. A., Welsh A. J., A review of the optical properties of biological tissues, *IEEE J Quant Electron*, 26-12 (1990) 2166-2185.

31. Cheong W., Prahl S. A., and Welch A. J., A Review of the Optical Properties of Biological Tissues, *IEEE J Quantum Elect*, 26 - 12 (1990).

32. Chui E. H. and Raithby G. D., An implicit solution scheme to improve convergence rate in radiative transfer problems, *Numer. Heat Transfer, B*, 22 (1992) 251–272.

33. Chui E. H., Raithby G. D., and Hughes P. M. J., Prediction of radiative transfer in cylindrical enclosures with the finite volume method, *J. Themophys. Heat Transfer,* 6 (1992) 605–611.

34. Crosbie A. L. and Lee L. C., Relation between multidimensional radiative transfer in cylindrical and rectangular coordinates with anisotropic scattering, *J. Quant. Spectrosc. Radiant. Transfer*, 38 (1987) 231-241.

35. Dai W., Wang H., Jordan P. M., Mickens R. E., Bejan A., A mathematical model for skin burn injury induced by radiation heating, *Int J Heat Mass Tran* ,51 (2008) 5497–5510.

36. Das C., Trivedi A., Mitra K., Vo-Dinh T., Experimental and numerical analysis of short-pulse laser interaction with tissue phantoms containing inhomogeneities, *Appl Optics*, 42-25 (2003) 5173-5180.

37. Das R., Mishra S. C., Uppaluri R., Retrieval of thermal properties in a transient conduction–radiation problem with variable thermal conductivity, *Int J Heat Mass Tran* ,52 (2009) 2749–2758.

38. Datta A. K., Biological and bioenvironmental Heat and Mass Transfer, Marceld Ekkerin, New York (2002).

39. Deng Z., Liu J., Analytical Study on Bioheat Transfer Problems with Spatial or Transient Heating on Skin Surface or Inside Biological Bodies, *J Biomech Eng T-ASME*, 124 (2002) 638-649.

40. Díaz S. H., Aguilar G., Lavernia E. J., and Wong B. J. F., Modeling the Thermal Response of Porcine Cartilage to Laser Irradiation, *IEEE J Sel Top Quant*, 7-6 (2001).

41. Dombrovsky L. A., Baillis D., In: Thermal radiation in disperse systems: an engineering approach. New York: Begell House; 2010.

42. Dombrovsky L. A., Timchenko V., Jackson M., Yeoh G. H., A combined transient thermal model for laser hyperthermia of tumors with embedded gold nanoshells, *Int J Heat Mass Transfer*, 54(25-26) (2011) 5459–5469.

43. Dombrovsky L. A., Timchenko V., Jackson M., Indirect heating strategy for laser induced hyperthermia: An advanced thermal model, *Int J Heat Mass Transfer*, 55(17-18) (2012) 4688–4700.

44. Dombrovsky L. A., The use of transport approximation and diffusion-based models in radiative transfer calculations, *Computational Thermal Sciences*, 4(4) (2012) 297-315.

45. Dua R. and Chakraborty S., A novel modeling and simulation technique of photo–thermal interactions between lasers and living biological tissues undergoing multiple changes in phase, *Comput Biol Med*, 35 (2005) 447–462.

46. Duck F.A., In: Physical properties of tissue: a comprehensive reference book. San Diego: Acad. Press; (1990).

47. Fan J. and Wang L., A general bioheat model at macroscale, *Int J Heat Mass Tran*, 54 (2011) 722–726.

48. Fanjul-Vélez F., Romanov O. G. and Arce-Diego J. L., Efficient 3D numerical approach for temperature prediction in laser irradiated biological tissues, *Comput. Biol. Med.*, 39 (2009) 810-817.

49. Filho R. C. M. and Pimenta A. P., A two-dimensional numerical simulation of combustion and heat transfer in radiant porous burners, *Combust. Sci. Technol.*, 183 (2011) 370-389.

50. Fiveland W.A., Discrete ordinate methods for radiative heat transfer in isotropically and anisotropically scattering media, *J. Heat Transfer*, 109 (1987) 809–812.

51. Fiveland W.A., Discrete-ordinates solution of the radiative transport equation for rectangular enclosures, *J. Heat Transfer*, 106 (1984) 699–706.

52. Franco W., Liu J., Wang G. X., Nelson J. S., and Aguilar G., Radial and temporal variations in surface heat transfer during cryogen spray cooling, *Phys. Med. Biol.* 50 (2005) 387-397.

53. Friedrich B., Michael D., Ulrich H., Roland K., Gerd K., Wolfgang K., Michael L., Reinhard N., Christian R., Nikolaus S., Recommendations for medical and aesthetic treatment of the skin using laser or intense pulsed light (IPL) systems, *Medical Laser Application*, 23 (2008) 105–114.

54. Gervais F. and Fonseca V., Lithium tantalate ($LiTaO_3$) Handbook of optical constants of solids III *Academic press* San Diego (1998) 777-805.

55. González N. F., Lozada J. F. and Burgos A. E. R., Bioheat Transfer in the Human Body, Congress on Biofluid Dynamics of Human Body Systems at University Of Puerto Rico, Mayaguez, 10 (2004).

56. Gupta P. K., Singh J., Rai K.N., Numerical simulation for heat transfer in tissues during thermal therapy, *J Therm Biol*, 35 (2010) 295–301.

57. Howell J. R., Siegel R., Mengüç M. P., In: Thermal radiation heat transfer. New York: CRC Press; (2010).

58. Hsieh S. S. and Tsai H. H., Thermal and flow measurements of continuous cryogenic spray cooling, *Arch Dermatol Res*, 298 (2006) 82–95.

59. Jaunich M., Raje S., Kyunghan K., Mitra K. and Guo Z., Bio-heat transfer analysis during short pulse laser irradiation of tissues, *Int J Heat Mass Tran*, 51 (2008) 5511–5521.

60. Jha K. K. and Narasimhan A., Three-dimensional bio-heat transfer simulation of sequential and simultaneous retinal laser irradiation, *Int J Therm Sci*, 50 (2011) 1191-1198.

61. Jiji L. M., Heat transfer in living tissue, Heat conduction, 3rd Edition, 2009 Springer.

62. Jing L., Xuexue Z., Cuncheng W., Wenqiang L. and Zepei R., Generalized time delay bioheat equation and preliminary analysis on its wave nature, *Chinese Science Bulletin*, 42 – 4 (1997).

63. Johansson R., Andersson K., Leckner B. and Thunman H., Models for gaseous radiative heat transfer applied to oxy-fuel conditions in boilers, *Int. J. Heat Mass Transfer*, 53 (2010) 220–230.

64. Katika K. M., Pilon L., Steady-state directional diffuse reflectance and fluorescence of human skin, *Appl Optics*, 45(17) (2006) 4174-4183.

65. Khanafer K., Bull J. L., Pop I. and Berguer R., Influence of pulsatile blood flow and heating scheme on the temperature distribution during hyperthermia treatment, *Int. J. Heat Mass Transfer*, 50 (2007) 4883-4890.

66. Khlebtzov N. G., Dykman L. A., Optical properties and biomedical applications of plasmonic nanoparticles, *J. Quant. Spectr. Radiat. Transfer*, 111 (2010) 1-35.

67. Kim J., Spray cooling heat transfer: The state of the art, *International Journal of Heat and Fluid Flow*, 28 (2007) 753–767.

68. Kim K. and Guo Z., Ultrafast radiation heat transfer in laser tissue welding and soldering, *Numer. Heat Transfer, A*, 46 (2004) 23–40.

69. Kim S. H. and Huh K. Y., Assessment of the finite-volume method and the discrete ordinate method for radiative heat transfer in a three-dimensional rectangular enclosure, *Numer. Heat Transfer, B*, 35 (1999) 85 – 112.

70. Kok H. P., Gellermann, J., van den Berg C. A. T., Stauffer P. R., Hand J. W., and Crezee, J., Thermal modelling using discrete vasculature for thermal therapy: a review, *Int. J. Hyperther.*, *29*(4), 336–345 (2013).

71. Lapotkoa D., Lukianova E., Potapnev M., Aleinikova O. and Oraevsky A., Method of laser activated nano-thermolysis for elimination of tumor cells, *Cancer Lett*, 239 (2006) 36–45.

72. Lee K. H. and Viskanta R., Two-dimensional combined conduction and radiation heat transfer: comparison of the discrete ordinates method and the diffusion approximation methods, *Numer. Heat Transfer A*, 39 (2001) 205-225.

73. Letfullin R.R., Iversen C.B., George T.F., *Nanomed. Nanotechnol. Biol. Med.*, 7 (2011) 137–145.

74. Li D., Chen B., Wu W. J., Wang G. X., He Y. L., Multi-scale modeling of tissue freezing during cryogen spray cooling with R134a, R407c and R404a *Applied Thermal Engineering* (2014a) 1-12.

75. Li D., He Y. L., Wang G. X., Wang Y. X. and Ying Z. X., A new model of selective photothermolysis to aid laser treatment of port wine stains, *Chin Sci Bull*, 58 (2013) 416-426.

76. Li D., Wang G. X., He Y. L., Wu W. J. and Chen B., A three-temperature model of selective photothermolysis for laser treatment of port wine stain containing large malformed blood vessels, *Applied Thermal Engineering*, 65 (2014b) 308-321.

77. Lister T., Wright P. A. and Chappell P. H., Optical properties of human skin, *Journal of Biomedical Optics*, 17 (2012) 090901-15.

78. Liu C., Mi C. C., Li B. Q., Energy absorption of gold nanoshells in hyperthermia therapy, *IEEE Trans Nanobiosci*, 7 (2008) 206-214.

79. Liu C., Mi C. C., Li B. Q., Energy absorption of gold nanoshells in hyperthermia therapy, *IEEE Transactions on Nanobioscience*, 7 (2008) 206-214.

80. Liu C., Mi C. C., Li B. Q., Transient temperature response of pulsed-laser-induced heating for nanoshell-based hyperthermia treatment, *IEEE Trans. Nanotechnol*, 8 (2009) 697-706.

81. Liu D. L., Engels S. A., Sturesson C., Svanberg K., Håkansson C. H. and Svanberg S., Tumour vessel damage resulting from laser-induced hyperthermia alone and in combination with photodynamic therapy, *Cancer Lett*, 111 (1997) 157-165.

82. Liu K.C. and Chen H.T., Investigation for the dual phase lag behavior of bio-heat transfer, *Int J Therm Sci*, 49 (2010) 1138-1146.

83. Loo C., Lin A., Hirsch L., Lee M. H., Barton J., Halas N., West J., Drezek R., Nanoshell-enabled photonics-based imaging and therapy of cancer, *Technol Cancer Res T*, 3 (2004) 33-40.

84. Loze M. K. and Wright C. D., Temperature distributions in laser-heated biological tissue with application to birthmark removal, *Journal of Biomedical Optics*, 6 (2001) 74–85.

85. Marakis J. G., Papapavlou C. and Kakaras E., A parametric study of radiative heat transfer in pulverised coal furnaces, , *Int. J. Heat Mass Transfer*, 43 (2000) 2961–2971.

86. Maruyama S., Light Energy Engineering, Yoken-do, Tokyo, 2004.

87. Maruyama S. and T. Aihara, Radiation Heat Transfer of Arbitrary Three-Dimensional Absorbing, Emitting and Scattering Media and Specular and Diffuse Surfaces, *J. Heat Transfer–T ASME*, 119 (1997) 129–136.

88. Maruyama S., Radiation Heat-Transfer between Arbitrary 3-Dimensional Bodies with Specular and Diffuse Surfaces, *Numer. Heat Transfer A*, 24 (1993) 181–196.

89. Minhua Z. and Qian C., Estimation of Temperature Distribution in Biological Tissue by Analytic Solutions of Pennes' Equation, *2nd International Conference on Biomedical Engineering and Informatics*, BMEI '09 (2009).

90. Minkowycz W. J., Sparrow E. M., Murthy J. Y., Chapter 26. Rubinsky B., Numerical Bioheat Transfer, Handbook of numerical heat transfer, second edition, John Wiley & Sons, Inc (2006).

91. Mishra S. C., Singh R., Agarwal P., and Krishna C. H., Analysis of radiative transport in a 2-D cylindrical participating medium subjected to collimated radiation *Numer Heat Transfer, A*, 66 (2014) 884-903.

92. Mishra S. C. and Sahai H., Analyses of non-Fourier conduction and radiation in a cylindrical medium using lattice Boltzmann method and finite volume method, *Int. J. Heat Mass Transfer*, 61 (2013) 41-45.

93. Mishra S. C., Chugh P., Kumar P. and Mitra K., Development and comparison of the DTM, the DOM and the FVM formulations for the short-pulse laser transport through a participating medium, *Int. J. Heat Mass Transfer*, 49 (2006) 1820–1832.

94. Mishra S. C., Kim M.Y. and Maruyama S., Performance evaluation of four radiative transfer methods in solving multi-dimensional radiation and/or conduction heat transfer problems, *Int. J. Heat Mass Transfer*, 55 (2012) 5819 – 5835.

95. Mishra S.C. and Krishna C. H., Analysis of radiative transport in a cylindrical enclosure - an application of the modified discrete ordinate method, *J. Quant. Spectrosc. Radiant. Transfer*, 112 (2011) 1065-1081.

96. Mishra S.C., Krishna C. H. and Kim M.Y., Lattice Boltzmann method and modified discrete ordinate method applied to radiative transport in a spherical medium with and without conduction, *Numer. Heat Transfer A*, 58 (2010) 852-881.

97. Mishra S.C., Krishna C. H. and Kim M.Y., Analysis of conduction and radiation heat transfer in a 2-D cylindrical medium using the modified discrete ordinate method and the lattice Boltzmann method, *Numer. Heat Transfer A*, 60 (2011) 254-287.

98. Mishra S.C., Roy H. K. and Misra N., Discrete ordinate method with a new and a simple quadrature scheme, *J. Quant. Spectrosc. Radiant. Transfer*, 101 (2006) 249-262.

99. Mishra S.C., Krishna C.H., Analysis of radiative transport in a cylindrical enclosure - an application of the modified discrete ordinate method, *J. Quant. Spectrsc. Radiat. Transfer*, 112 (2011) 1065-1081.

100. Mishra S. C., Krishna C. H., Kim M.Y., Analysis of conduction and radiation heat transfer in a 2-D cylindrical medium using the modified discrete ordinate method and the lattice Boltzmann method, *Numer. Heat Transfer A*, 60 (2011) 254-287.

101. Mishra S. C., Chug P., Kumar P., Mitra K., Development and comparison of the DTM, the DOM and the FVM formulations for the short-pulse laser transport through a participating medium, *Int. J. Heat Mass Transfer*, 49 (2006) 1820-1832.

102. Mishra S. C., Roy H. K., Misra N., Discrete ordinate method with a new and a simple quadrature scheme, *J. Quant Spectrsc Radiat Transfer*, 101 (2006) 249-262.

103. Mishra S. C., Singh R., Agarwal P., Krishna C. H., Analysis of radiative transport in a 2-D cylindrical participating medium subjected to collimated radiation, *Numer Heat Transfer, A* 66 (2014) 884-903.

104. Mishra, S.C., and Krishna, C.H., Analysis of radiative transport in a cylindrical enclosure - an application of the modified discrete ordinate method, *J. Quant. Spectrosc. Radiant. Transfer*, 112 (2011)1065-1081.

105. Mishra, S.C., Krishna, C.H. and Kim, M.Y., Analysis of conduction and radiation heat transfer in a 2-D cylindrical medium using the modified discrete ordinate method and the lattice Boltzmann method, *Numer. Heat Transfer A*, 60 (2011) 254-287.

106. Mitra K., Kumar S., Vedevarz A., and Moallemi M. K., Experimental Evidence of Hyperbolic Heat Conduction in Processed Meat, *J. Heat Transfer T-ASME*, 117-3 (1995) 568.

107. Mobley J., Vo-Dinh T. Optical properties of tissue. In: Vo-Dinh T, editor. Biomedical photonics handbook. Boca Raton: CRC Press (2003).

108. Modest M. F., *Radiative Heat Transfer*. 3rd Edition, Academic press, New York, 2013.

109. Muller G. J., Berlien P. and Scholz C., The medical laser, *Medical Laser Application* 21 (2006) 99–108.

110. Murthy J. Y., Mathur S. R., A finite-volume scheme for radiative heat transfer in semitransparent media, *Numer. Heat Transfer, B*, 37 (2000) 25-43.

111. Muthukumaran R., Mishra S. C., Maruyama S., Mitra K., Assessment of signals from a tissue phantom subjected to radiation sources of temporal spans of the order of a nano-, pico-, and femtosecond—a numerical study, *Numer. Heat Transfer A*, 60 (2011) 154-170.

112. Muthukumaran R., Mishra S. C., Radiative transfer of a short-pulse laser wave of Gaussian temporal profile through a 2-D participating medium containing inhomogeneities of different shapes at various locations, *Numer. Heat Transfer A*, 54 (2008) 546-567.

113. Muthukumaran R., Mishra S. C., Transient response of a planar participating medium subjected to a train of short-pulse radiation, *Int. J Heat Mass Transfer*, 51 (2008) 2418–2432.

114. Muthukumaran R. and Mishra S.C., Radiative transfer of a short-pulse laser wave of Gaussian temporal profile through a 2-D participating medium containing inhomogeneities of different shapes at various locations, *Numer. Heat Transfer A*, 54 (2008) 546-567.

115. Muthukumaran R., Mishra S. C., Transient response of a planar participating medium subjected to a train of short-pulse radiation, *Int. J. Heat Mass Transfer*, 51 (2008) 2418–243.

116. Ng E.Y.K. and Chua L.T., Comparison of one- and two-dimensional programmes for predicting the state of skin burns, *Burns*, 28 (2002) 27–34.

117. Niemz M. H., Laser-Tissue Interactions, Fundamental and Applications, 3rd Edition, Springer, Heidelberg, 2007.

118. Okajima J., Maruyama S., Takeda H., Komiya A., Dimensionless solutions and general characteristics of bioheat transfer during thermal therapy, *J Ther Biol*, 34 (2009) 377–384.

119. Okutucu T., Yener Y., Participating media exposed to collimated short-pulse irradiation – A Laguerre–Galerkin solution, *Int J Heat Mass Transfer*, 50 (2007) 4352–4359.

120. Othman M. I. A., Ali M. G. S., Farouk R. M., The Effect of Relaxation Time on the Heat Transfer and Temperature Distribution in Tissues, *World Journal of Mechanics*, 1 (2011) 283-287.

121. P. F. Hsu, Z. M. Tan, S. H. Wu and C.Y. Wu, Radiative heat transfer in finite cylindrical homogeneous and nonhomogeneous scattering media exposed to collimated radiation, *Numer. Heat Transfer A*, 35 (1999) 655-679.

122. Palik E. D., Lithium niobate ($LiNbO_3$) Handbook of optical constants of solids I *Academic press* San Diego (1998) 695-702.

123. Partridge P.W. and Wrobel L.C., An inverse geometry problem for the localisation of skin tumours by thermal analysis, *Eng Anal Bound Elem*, 31 (2007) 803–811.

124. Patel B. S. and Zaidi Z. H., The suitability of sapphire for laser windows, *Meas. Sci. Technol.* 10 (1999)146.

125. Pearce J. A., Valvano J. W., Emelianov S., Temperature measurements, Welch AJ, Gemert MJCV. Optical-Thermal Response of Laser-Irradiated Tissue. New York: Springer (2011).

126. Pennes H. H., Analysis on Tissue Arterial Blood Temperature in the Resting Human Forearm, *J Appl Physiol*, 1 (1948) 93-122, reprinted (1998).

127. Perkins R. A. and Huber M. L., Measurement and Correlation of the Thermal Conductivity of 2,3,3,3-Tetrafluoroprop-1-ene (R1234yf) and trans-1,3,3, 3-Tetrafluoropropene (R1234ze(E)) *J. Chem. Eng. Data*, 56 (2011) 4868–4874.

128. Raithby G. D. and Chui E. H., A finite volume method for predicting radiant heat transfer in enclosures with participating media, *J. Heat Transfer*, 112 (1990) 415–423.

129. Randrianalisoa J. H., Dombrovsky L. A., Lipiński W., Timchenko V., Effects of short-pulsed laser radiation on transient heating of superficial human tissues, *Int. J. Heat Mass Transfer*, (2014) - in press.

130. Rath P., Mishra S.C., Mahanta P., Saha U. K. and Mitra K., Discrete transfer method applied to transient radiative transfer problems in participating medium, *Numer. Heat Transfer A*, 44 (2003) 183-197.

131. Roa W.H., Azarmi S., Al-Hallak M.H.D.K., W.H. Finlay, A.M. Magliocco, R. Lobenberg, *J. Controlled Release*, 150 (2011) 49–55.

132. Roselli R. J. and Diller K. R., Biotransport: Principles and Applications, (2011) Springer.

133. Rossi M. R. and Rabin Y., Analysis of a numerical scheme for bioheat simulations of cryosurgery and its experimental validation on a phantom material. MSV'07- The 2007 *International Conference on Modeling, Simulation and Visualization Methods*, Las Vegas, Nevada, USA (2007).

134. Sajjadi A.Y., Mitra K., Grace M., Ablation of subsurface tumors using an ultra-short pulse laser, *Optics and Lasers in Engineering*, 49 (2011) 451–456.

135. Sakurai A., Maruyama S. and Matsubara K., The Radiation Element Method Coupled with the Bioheat Transfer Equation Applied to the Analysis of the Photothermal Effect of Tissues, *Numer. Heat Transfer A*, 58-8 (2010) 625-640.

136. Sarma D., Mishra S. C. and Mahanta P., Analysis of collimated radiation in participating media using the discrete transfer method, *J. Quant. Spectrosc. Radiant. Transfer*, 96 (2005) 123–135.

137. Shih T., Liu H. and Horng T. A, Cooling effect of thermally significant blood vessels in perfused tumor tissue during thermal therapy, *Int Commun Heat Mass*, 33 (2006) 135– 141.

138. Singh R., Mishra S. C., Analysis of radiative heat transfer in a planar participating medium subjected to diffuse and/or collimated radiation – A comparison of the DTM, the DOM and the FVM, *Numer. Heat Transfer A*, 52 (2007) 481-496.

139. Singh R. and Mishra S.C., Analysis of radiative heat transfer in a planar participating medium subjected to diffuse and/or collimated radiation – A comparison of the DTM, the DOM and the FVM, *Numer. Heat Transfer A*, 52 (2007) 481-496.

140. Svaasand L. O., Randeberg L. L., Aguilar G., Majaron B., Kimel S., Lavernia E. J. and Nelson J. S., Cooling efficiency of cryogen spray during laser therapy of skin, *Lasers in Surgery and Medicine* 32 (2003) 137–142.

141. Torres J. H., Nelson J. S., Tanenbaum B. S., Milner T. E., Goodman D. M., and Anvari B., Estimation of internal skin temperatures in response to cryogen spray cooling: implications for laser therapy of port wine stains, *IEEE Journal of selected topics in quantum electronics*, 5 (1999) 1058-1066.

142. Trivedi A., Basu S., Mitra K., Temporal analysis of reflected optical signals for short pulse laser interaction with nonhomogeneous tissue phantoms, *J. Quant Spectrsc Radiat Transfer*, 93 (2005) 337–348.

143. Tropf W. J., Yattrium aluminum garnet ($Y_3Al_5O_{12}$) Handbook of optical constants of solids III *Academic press* San Diego, (1998) 963-986.

144. Tropf W. J. and Thomas M. E., Aluminum oxide (Al_2O_3) revisited Handbook of optical constants of solids III *Academic press* San Diego (1998) 653-682.

145. Tuchin V.V., Tissue optics: light scattering methods and instruments for medical diagnosis. Bellingham SPIE Press; (2007).

146. Tung M. M., Trujillo M., Molina J.A. L´opez, Rivera M.J., and Berjano E.J., Modeling the Heating of Biological Tissue based on the Hyperbolic Heat Transfer Equation, *Math Comput Model*, 50 (2009) 665-672.

147. Veiseh S. and Hakkaki-Fard A., Numerical modeling of combined radiation and conduction heat transfer in mineral wool insulations, *Heat Transfer Eng*, 30 (2009) 477-486.

148. Versteeg, H.K. and Malalasekera W., An introduction to computational fluid dynamics, the finite volume method, Longman Group Limited, New York (1995).

149. Wang H., Zhou Z., Tian H., Effect of light intensity on reflectance and transmittance of a laser beam incident on a gold film, *Optics and Lasers in Engineering*, 48 (2010) 703–706.

150. Wang L. and Fan J., Modeling Bioheat Transport at Macroscale, *J Heat Transf*, *T-ASME*, 133 (2011).

151. Wang L., Zhou X. and Wei X., Heat Conduction, Mathematical Models and Analytical Solutions, Springer (2008).

152. Weinbaum S. and Jiji L. M., A new simplified bioheat equation for the effect of blood flow on local average tissue temperature, *J Biomech Eng-T ASME*, 107 (1985) 131-139.

153. Welch A. J. and Gemert M.J.C.V, Optical-Thermal Response of Laser-Irradiated Tissue, 2nd edition, Springer, New York, (2011).

154. Welch A. J., The Thermal Response of Laser Irradiated Tissue, *IEEE J Quant Elect*, (1984) 20-12.

155. Welch, A.J, and Gemert M.J.C.V, Optical-Thermal Response of Laser-Irradiated Tissue, 2nd edition, Springer, New York (2011).

156. Wissler, E. H., Pennes' 1948. Paper Revisited, *J Appl Physiol*, 85 (1998) 35-41.

157. Wu C. Y. and Ou N. R., Differential approximation for transient radiative transfer through participating medium exposed to collimated radiation. *J. Quant. Spectrosc. Radiant. Transfer*, 73 (2002) 111-120.

158. Wu S. C. and Wu C. Y., Radiative heat transfer in a two-dimensional cylindrical medium exposed to collimated radiation, *Int. J. Heat Mass Transfer,* 24 (1997) 475-484.

159. Wu S. H. and Wu C. Y., Integral equation formulation for transient radiative transfer in an anisotropically scattering medium, *Int. J. Heat Mass Transfer,* 43 (2000) 2009-2020.

160. Xu F. and Lu T., Introduction to Skin Biothermomechanics and Thermal Pain, Science Press Beijing and Springer (2011).

161. Xu F., Lu T. J., Seffen K. A. and Ng E. Y. K., Mathematical Modeling of Skin Bioheat Transfer, *Applied Mechanics Reviews*, 62-5 (2009) 050801-1 – 35.

162. Xu X., Meade A., Bayazitoglu Y., Numerical investigation of nanoparticle-assisted laser-induced interstitial thermotherapy toward tumor and cancer treatments, *Lasers Med Sci*, 26 (2011) 213–222.

163. Zenzie H. H., Altshuler G. B., Smirnov M. Z. and Anderson R. R., Evaluation of cooling methods for laser dermatology, *Lasers Surg Med*, 26 (2000) 130–144.

164. Zhou J. and Liu J., Numerical study on 3-d light and heat Transport in biological tissues embedded with large blood vessels during laser-induced Thermotherapy, *Numer. Heat Transfer A*, 45 (2004) 415–449.

165. Zhou J., Zhang Y. , Chen J. K., An axisymmetric dual-phase-lag bioheat model for laser heating of living tissue, *Int J Therm Sci,* 48 (2009) 1477–1485.

166. Zhou J., Zhang Y. and Chen J. K., Non-Fourier Heat Conduction Effect on Laser-Induced Thermal Damage in Biological Tissues, *Numer. Heat Transfer A*, 54-1 (2008) 1-19.

167. Zhou Z., Chen B., Wang Y., Guo L. and Wang G., An experimental study on pulsed spray cooling with refrigerant R-404a in laser Surgery, *Applied Thermal Engineering*, 39 (2012) 29-36.